MULTI-SCALE PARAMETERISATION OF STATIC AND DYNAMIC CONTINUUM POROUS PERFUSION MODELS USING DISCRETE ANATOMICAL DATA

Author:
Eoin Ronan HYDE,
University College

Supervisors:
Prof. Nic SMITH
and
Prof. Jon CHAPMAN



COMPUTATIONAL BIOLOGY GROUP,
DEPT. OF COMPUTER SCIENCE

Thesis submitted for the degree of Doctor of Philosophy

MICHAELMAS TERM 2013

Multi-scale parameterisation of static and dynamic continuum porous perfusion models using discrete anatomical data

E.R. Hyde, University College, 2013.

Abstract

The aim of this thesis is to replace the intractable problem of using discrete flow models within large vascular networks with a suitably parameterised and tractable continuum perfusion model. Through this work, we directly address the hypothesis that discrete vascular data can be incorporated within continuum perfusion models via spatially-averaged parameterisation techniques.

Chapter 1 reviews biological perfusion from both clinical and computational modelling perspectives, with a particular focus on myocardial perfusion.

In Chapter 2, a synthetic 3D vascular network was constructed, which was controllable in terms of its size and properties. A multi-compartment static Darcy perfusion model of this discrete system was parameterised via a number of techniques. Permeabilities were derived using: *(i)* porosity-scaled isotropic($\phi \boldsymbol{I}$); *(ii)* Huyghe and Van Campen (HvC); and *(iii)* projected-PCA parameterisation methods. It was found that HvC permeabilities and pressure-coupling fields derived from the discrete data produced the best comparison to the spatially-averaged Poiseuille pressure.

In Chapter 3, the construction and analysis of high-resolution anatomical arterial vascular models was undertaken.

In Chapter 4, various anatomically-derived vascular networks were used to parameterise our perfusion model, including a μCT-derived rat capillary network, a single arterial subtree, and canine and porcine whole-organ arterial models. Allowing for general-connectivity (as opposed to strictly-hierarchical connectivity) yielded a significant improvement on the continuum model pressure. For the whole-organ model however, it was found that the best results were obtained by using porosity-scaled isotropic permeabilities and anatomically-derived pressure-coupling fields. It was also discovered that naturally occurring small length but relatively large radius vessels were not suitable for the HvC method.

In Chapter 5, the suitability of derived parameters for use within a dynamic perfusion model was examined. It was found that the parameters derived from the original static network were adequate for application throughout the cardiac cycle.

Chapter 6 presents a concluding discussion, highlighting limitations and future directions to be investigated.

Acknowledgements

Firstly, I would like to thank my supervisors Professor Nic Smith and Professor Jon Chapman for all their help and advice over the course of my PhD. Amongst many fine attributes, they provided the perfect blend of support and motivation.

I would also like to thank my peers in both Oxford and King's College London for many useful discussions over our tea/coffee breaks, both of an academic and a spiritual nature. Deserving of particular mention here is the 'Poro Modelling Group' based at KCL, who's members had to routinely decipher my streams of consciousness.

Thanks also to our colleagues in the Academic Medical Centre, University of Amsterdam for providing us with crucial data and fruitful discussions, without which this thesis would not have been possible.

I would like to express further gratitude to my family, girlfriend and friends, who have made my time in Oxford and London such an enjoyable one. Their support through good times and bad was invaluable to me, and I really couldn't have completed this work without them.

I am especially indebted to my parents, Maura and Jerry. Their infinite sacrifices have allowed me to travel far and wide in pursuit of my goals, and it is impossible for me to adequately express my love for them in words.

Foreword

During the course of my post-graduate studies at the University of Oxford, I have had the great fortune to work with a dedicated and enthusiastic research group. Several have made contributions to the research described in this thesis, and feature as fellow authors on my publications. Similarly, I have assisted with research projects undertaken by colleagues, either by model development and/or providing data acquired from my research. For this reason, I am listed as an author on six peer-reviewed scientific publications (two as first author), one paper undergoing review, and at least two further planned publications. It is important, however, to clearly delineate the contributions of others to the work contained in this thesis, and to link the relevant sections to the corresponding publication. This clarification is presented in the following paragraphs, and all work that is not directly attributed to a colleague is work done solely by myself.

Several sections from Chapter 1 were adapted for use in a 2013 review paper entitled *"Myocardial perfusion distribution and coronary arterial pressure and flow signals in the heart : clinical relevance in relation to multi scale modelling , a review"* and published in the journal Medical Biological Engineering & Computing. In particular, this included the review of 1D flow modelling techniques and 3D perfusion modelling efforts.

The fundamental research featuring in Chapter 2, which identified key traits of spatial-averaging parameterisation techniques, has been published in the same journal, also in 2013, entitled *"Parameterisation of multi-scale continuum perfusion models from discrete vascular networks"*. The continuum model results were solved using an in-house closed-source software package, called 'CHeart', via the finite element method. This package was founded by Dr. David Nordsletten (King's College London (KCL)), and is now co-developed by up to twenty

post-doctoral researchers and technical staff. Furthermore, with the exception of Appendix A, all continuum model solutions displayed in this thesis were solved for using this software.

Chapter 3 features the cryomicrotome data from which the whole-heart anatomical models are constructed. These data were supplied by our collaborators at the Academic Medical Centre (AMC), University of Amsterdam. Deserving of specific mention here are Dr. Pepijn van Horssen (AMC) and Dr. Jeroen van den Wijngaard (AMC), and Prof. Jos Spaan (AMC) as the principal investigator. The creation of the vascular models was enabled by another in-house tool developed by Dr. Ayush Goyal (Oxford), and subsequently improved upon by Dr. Taha Sochi (KCL), Mr. Matthew Sinclair (KCL) and myself. A portion of the tissue model generation pathway uses an automatic cubic Hermite mesh fitting tool developed by Dr. Pablo Lamata (Oxford) as part of the 'euHeart' funding initiative [1]. An 'epicardial-only' discrete vascular model that I extracted from the full porcine model was used in the paper entitled *"A computationally efficient framework for the simulation of cardiac perfusion using a multi-compartment Darcy porous-media flow model"* published in International Journal for Numerical Methods in Biomedical Engineering.

The rat capillary network that appears in Chapter 4 and in the Hyde *et al.* paper *"Parameterisation of multi-scale continuum perfusion models from discrete vascular networks"* is courtesy of Dr. Jack Lee (KCL). The second anatomical model study that featured the porcine arterial subtree was published as an example of our regional perfusion modelling strategy in Journal of Biomechanics in the paper *"A novel porous mechanical framework for modelling the interaction between coronary perfusion and myocardial mechanics"*. The parameterisation results of this chapter have been presented in the paper *"Multi-scale parameterisation of a myocardial perfusion model using whole-organ arterial networks"* which has been published in the journal Annals of Biomedical Engineering.

The deformation used throughout Chapter 5 was produced *in silico* by Dr. Jack Lee using an incompressible hyperelastic model of cardiac motion. The research featured in this chapter will be the first of the remaining planned publications. Finally, in Chapter 6, the contrast agent transport model has been developed primarily by Dr. Andrew Cookson (KCL), with the specific model equations being presented in the paper *"A Finite Element Model of MRI Contrast Agent Transport in the Myocardium"* submitted to MedIA. The preliminary result displayed in this chapter was simulated by Dr. Radomir Chabiniok (KCL). Applying the transport model to velocity fields derived from an anatomically-parameterised perfusion model for both healthy and pathological scenarios will be the subject of the second planned publication.

[1] http://amdb.isd.kcl.ac.uk/

Publications

The following is a list of completed publications arising thus far from the research presented in this thesis.

Published works

1) **Hyde, E.R.**, Cookson, A.N., Lee, J., Michler, C., Goyal, A., Sochi, T., Chabiniok, R., Sinclair, M., Nordsletten, D.A., Spaan, J.A.E., van den Wijngaard, J.P.H.M., Siebes, M., Smith, N.P. *Multi-scale parameterisation of a myocardial perfusion model using whole-organ arterial networks*. Annals of Biomedical Engineering. (Volume and page numbers were not available at time of writing) (2013)

2) Nolte, F., **Hyde, E.R.**, Rolandi, C.M., Lee, J., van Horssen, P., Asrress, K., van den Wijngaard, J.P.H.M., Cookson, A.N., van den Hoef, T., Chabiniok, R., Razavi, R., Michler, C., Hautvast, G., Piek, J.J., Breeuwer, M., Siebes, M., Nagel, E., Smith, N.P., Spaan, J.A.E., *Myocardial perfusion distribution and coronary arterial pressure and flow signals in the heart : clinical relevance in relation to multi scale modeling , a review*. Medical and Biological Computing and Engineering. 51(11),1271–1286. (2013)

3) **Hyde E.R.**, Lee J., Cookson A.N., Michler C., Chabiniok R., Nordsletten, D.A. and Smith N.P., *Parameterisation of multi-scale continuum perfusion models from discrete vascular networks*. Medical and Biological Computing and Engineering. 51(5),557–570. (2013)

4) Michler C., Cookson A.N., Chabiniok R., **Hyde E.R.**, Lee J., Sinclair M., Sochi, T., Goyal, A., Vigueras-Gonzalez, G., Nordsletten D.A., and Smith

N.P., *A computationally efficient framework for the simulation of cardiac perfusion using a multi-compartment Darcy porous-media flow model*. International Journal for Numerical Methods in Biomedical Engineering. 29(2),217–232. (2012)

5) Cookson A.N., **Hyde E.R.**, Lee J., Michler C., Smith N.P., and Spaan J.A.E., *Validation and parameterisation of vascular tree and porous elastic models by microspheres and other functional predictions*. euHeart deliverable 8.2.2. (2011)

6) Cookson A.N., Lee J., Michler C., **Hyde E.R.**, Nordsletten D.A., Sinclair M., Siebes M., and Smith N.P., *A novel porous mechanical framework for modelling the interaction between coronary perfusion and myocardial mechanics*. Journal of Biomechanics. 45(5),850–855. (2011)

Submitted work

7) Cookson, A.N., Lee, J., Michler, C., Chabiniok, R., **Hyde, E.R.**, Nordsletten, D.A., Smith, N.P., *A Finite Element Model of MRI Contrast Agent Transport in the Myocardium*. Medical Image Analysis. (2013)

Honourable Mention

- The following poster received an honourable mention at the 4^{th} Cardiac Physiome Workshop, July 2011 –

  Hyde E.R., Cookson A.N., Goyal A., Lee J., Sinclair M., Michler C., Spaan J.A.E., Siebes M., van den Wijngaard J.P., and Smith N.P., 2011, *Determining fluid–related parameters for poroelastic perfusion modelling*, 4^{th} Cardiac Physiome Workshop, Oxford.

Contents

Abstract ii

Acknowledgements iii

Foreword iv

Publications vi

List of Figures xii

List of Tables xv

List of Symbols xvii

List of Abbreviations xix

1 Introduction 1

1.1 Background . . . 3

1.1.1 Cardiac Function . . . 3

1.1.2 Clinical Context . . . 5

1.1.3 Clinical and Experimental Data . . . 7

1.2 Previous Work . . . 11

1.2.1 Perfusion Modelling . . . 11

1.2.2 Coronary Structure and Deformation 18
1.3 Thesis Objectives 21
1.4 Thesis Outline 24

2 Darcy Model: Synthetic Network **26**
2.1 Continuum Darcy Model 27
2.1.1 Multi-compartment Motivation 27
2.1.2 Multi-compartment Static Darcy System 29
2.2 Discrete Vascular Anatomy 32
2.2.1 Generation of a Synthetic Network 33
2.2.2 Poiseuille Flow Model 37
2.2.3 Vascular Partition 39
2.3 Darcy Model Parameterisation 41
2.3.1 Spatially-averaged Discrete Fields 41
2.3.2 Determination of Permeability 43
2.3.3 Determination of Pressure-coupling Coefficients 46
2.4 Results 48
2.4.1 RVE Radius 51
2.4.2 $\boldsymbol{K}$ Parameterisation and Vessel Density 53
2.4.3 Independence from Poiseuille Pressure BCs 53
2.4.4 Compartmental Mass Transfer 56
2.5 Discussion 57

3 Arterial Model Creation **61**
3.1 Cryomicrotome Imaging 62
3.1.1 Vascular Model Creation 63
3.1.2 Myocardial Tissue Model Creation 65
3.2 Vascular Model Reduction 65
3.2.1 Reduced Arterial Model Statistics 70
3.3 Model Comparison to Experimental Data 72
3.4 Discussion 74

4 Darcy Model: Anatomical Network **80**

4.1 Parameterisation Methods . . . 81
4.1.1 1D Model Component and Vascular Partition . . . 81
4.1.2 Anatomical Parameterisation Methods . . . 84
4.1.3 LVM Boundary Conditions . . . 86
4.2 Results . . . 88
4.2.1 Capillary Anisotropic Network Test . . . 88
4.2.2 Single Arterial Subtree Reveals the Importance of β . . . 90
4.2.3 Anatomical LV Perfusion Model . . . 91
4.2.3.1 Extracted Porosity Values . . . 92
4.2.3.2 Variability of Permeability Properties . . . 93
4.2.3.3 Effect of Anatomical Parameters . . . 96
4.2.3.4 Model Sensitivity to τ and N . . . 98
4.3 Discussion . . . 99
4.3.1 Limitations of Darcy Parameterisation via Anatomical Networks . . . 103
4.3.2 Clinical Implications . . . 107

5 Darcy Model: Dynamic Networks 110
5.1 Myocardial-vessel Interaction . . . 111
5.2 A Deforming Myocardial Model . . . 115
5.2.1 Displacement Mapping Method . . . 117
5.2.2 Deformation Gradient Tensor . . . 121
5.2.3 Treatment of the Vascular Model . . . 123
5.3 Dynamic Parameterisation Methods . . . 127
5.3.1 Choice of Reference State . . . 131
5.4 Results . . . 134
5.4.1 Temporal Strain Measures . . . 134
5.4.2 Temporal $\boldsymbol{K}$ Modification . . . 137
5.5 Discussion . . . 140
5.5.1 Deformation Effects on Network Topology . . . 141
5.5.2 Negligible Benefit of Temporal Parameter Updating . . . 142
5.5.3 Limitations of the Model . . . 145

6 Conclusions **149**
6.1 Limitations . . . 149
6.2 Future Directions . . . 153
6.2.1 Coronary Occlusion Simulations . . . 153
6.2.2 Contrast Agent Transport . . . 156
6.3 Dissertation Contributions . . . 156

A FEM Solutions for Darcy Flow **161**
A.1 Introduction to the Finite Element Method . . . 163
A.1.1 Nodes, Elements and Basis Functions . . . 163
A.1.1.1 Piecewise Bilinear Basis Functions . . . 165
A.1.2 Weak Formulation and the Finite Element Formulation . . . 167
A.1.3 System Assembly for Linear FE Problems . . . 170
A.1.4 Numerical Integration and Gaussian Quadrature . . . 171
A.2 Darcy Flow Solutions via FEM . . . 172
A.3 Sample Results and Software Verification . . . 175

B A Brief Introduction to Poroelasticity **177**
B.1 Poroelastic Perfusion Model Equations . . . 177
B.1.1 Flow . . . 178
B.1.2 Deformation . . . 179

Bibliography **182**

Glossary **198**

List of Figures

1.1 Heart/vascular structure 4
1.2 Perfusion MRI at 1.5T and 3T 9
1.3 Strahler ordering schematic 19
1.4 Coronary perfusion modelling pipeline 22

2.1 RVE schematic 28
2.2 Multi-compartment motivation 28
2.3 Spatial coexistence of compartments 29
2.4 Vascular model schematic 34
2.5 Synthetic model construction 35
2.6 Vascular model length *vs* radius 36
2.7 Poiseuille solution on the synthetic network 38
2.8 Hierarchic parameter field 40
2.9 Synthetic model vascular partition 41
2.10 Synthetic model β fields 50
2.11 Synthetic model RMS error 51
2.12 Actual *vs* averaged pressure RMS 52
2.13 Synthetic qualitative results 54
2.14 RMS comparison of K methods 55
2.15 Compartmental mass transfer 57

3.1 Cryomicrotome to vascular model pipeline . . . 64
3.2 LV myocardial tissue model generation . . . 66
3.3 Tissue invagination challenge . . . 67
3.4 Schematic of vascular reduction . . . 68
3.5 Anatomical network reduction . . . 69
3.6 Anatomical network number of vessel generations . . . 70
3.7 Anatomical network statistics . . . 71
3.8 Sigmoidal fit to experimental data . . . 73
3.9 Network radius versus influx . . . 75
3.10 Carmine microsphere distribution for porcine heart . . . 76

4.1 Anatomical parameterisation schematic . . . 82
4.2 Porcine 1D model components . . . 83
4.3 Anisotropic rat capillary study . . . 89
4.4 Porcine single artery study with general-connectivity . . . 92
4.5 Porcine transmural porosity . . . 93
4.6 HvC method eigenvalue distributions . . . 95
4.7 HvC method determinant and Υ distributions . . . 95
4.8 LV model rms . . . 97
4.9 Porcine LV β distributions . . . 98
4.10 LV canine qualitative results . . . 99
4.11 LV model velocity fields . . . 100
4.12 LV model porosity . . . 100
4.13 LV model Darcy pressure . . . 101
4.14 LV model spatially-averaged discrete pressure . . . 101
4.15 Parameter fields scaling landscape . . . 103

5.1 Schematic of the dynamic parameterisation comparison . . . 112
5.2 Electron scanning microscope fibre image . . . 115
5.3 Tissue model displacement mapping pipeline . . . 118
5.4 Simulated cryomicrotome tissue model deformation . . . 119
5.5 Dynamic tissue model displacement data . . . 120

5.6 Schematic of a deformable body undergoing motion 122
5.7 Deforming tissue and vascular models 124
5.8 Arterial blood volume assuming constant radii 127
5.9 Dynamic Poiseuille conductance ratio vs stretch 130
5.10 Sample vessel strain with $t_{ref} = 0$ 135
5.11 Strain histograms for diastole and systole 135
5.12 Vessel strain histograms 136
5.13 Normalised strain results 137
5.14 RMS error for dynamic K parameterisation 138

6.1 Porcine model normalised vessel taper 150
6.2 Porcine impermeable boundaries 155
6.3 Coronary occlusion and impermeable myocardial regions 157

A.1 Master bilinear quadrilateral and sample mesh 167
A.2 Darcy pressure and velocity results 176

List of Tables

1.1 Sample list of computational biology research projects 2
1.2 Non-explicitly parameterised perfusion models 17
1.3 Connectivity matrix of a porcine LAD 25

4.1 Effect of key vasoactive agents on vessel scale 87
4.2 RMS error for anisotropic networks 89
4.3 Statistical properties of the porcine HvC $\boldsymbol{K}$ field 96
4.4 Canine and porcine optimised scales 102

5.1 Quantification of dynamic $\boldsymbol{K}$ parameterisation via transient integration 140

List of Symbols

β	Pressure-coupling array	[mm^3 Pa^{-1} s^{-1}]
C	Poiseuille conductance	[mm^3 Pa^{-1} s^{-1}]
$\triangle$	Porosity-weighted root-mean-square error metric	[Pa]
δ	Kronecker delta function	[-]
f	Synthetic model bifurcation distance fraction	[-]
$\boldsymbol{I}$	Identity tensor	[-]
J	Jacobian of a continuum body deformation	[-]
$\boldsymbol{K}$	Permeability tensor field	[mm^2 Pa^{-1} s^{-1}]
λ	General eigenvalue	[-]
μ	Dynamic viscosity	[Pa s]
N	Total number of Darcy compartments	[-]
ν	General eigenvector	[-]
$\boldsymbol{w}$	Darcy fluid velocity	[mm s^{-1}]

p	Darcy pore pressure	[Pa]
$\overline{p}$	Spatially-averaged discrete pressure	[Pa]
$\tilde{p}$	Discrete Poiseuille pressure	[Pa]
ϕ	Porosity	[-]
ψ	Displacement mapping of a continuum body	[-]
q	Discrete vessel flux	[$mm^3\ s^{-1}$]
Q	Spatially-averaged inter-compartment flux	[$mm^3\ s^{-1}$]
$\boldsymbol{R}$	Rotation tensor	[-]
s	Darcy volumetric source field	[$mm^3\ s^{-1}$]
τ	Radius threshold for 1D model component	[mm]
Θ	Set of vascular nodes with radius $\geq \tau$	[-]
$\boldsymbol{U}$	Stretch tensor	[-]
Υ	Relative anisotropy for point-wise permeability tensors	[-]
φ	FEM basis function	[-]
ζ	Hierarchic network parameter	[-]

List of Abbreviations

ABV	Arterial Blood Volume
BC	Boundary Condition
CA	Contrast Agent
CCO	Constrained Constructed Optimisation
CDF	Cumulative Distribution Function
CFD	Computational Fluid Dynamics
CH	Cubic Hermite
CVD	Cardiovascular Disease
CVR	Coronary Vascular Resistance
DOF	Degrees Of Freedom
ECG	Electrocardiography
ECHO	Echocardiography
ELV	Element Load Vectors
ESM	Element Stiffness Matrices
ETT	Exercise Tolerance Test
FE	Finite Element
FEM	Finite Element Method
FSI	Fluid Solid Interaction

HvC	Huyghe and van Campen
IMP	Intramyocardial Pressure
IQR	Inter-quartile Range
LA	Left Atrium
LCA	Left Coronary Artery
LCX	Left Circumflex
LGE	Late Gadolinium Enhancement
LV	Left Ventricle
LVM	Left Ventricular Model
MI	Myocardial Infarction
MRI	Magnetic Resonance Imaging
MSCT	MultiSlice Computerised Tomography
PCA	Principal Components Analysis
PCI	Percutaneous Coronary Intervention
PDE	Partial Differential Equation
PDF	Probability Density Function
PET	Positron Emission Tomography
PLR	Path of Least Resistance
RA	Right Atrium
RCA	Right Coronary Artery
rms	root-mean-square
RV	Right Ventricle
RVE	Representative Volume Element
SD	Standard Deviation
SPD	Symmetric Positive Definite
SPECT	Single Photon Emission Computed Tomography
STEMI	ST-segment-Elevation Myocardial Infarction
XRA	X-Ray Angiography

1 Introduction

Of an estimated 1.9 million deaths within the European Union (EU) in the year 2012, Cardiovascular Disease (CVD) accounted for 40% [102]. Overall, CVD is estimated to cost the EU economy almost €196 billion a year [102]. This considerable figure consists of costs related to healthcare (54%), productivity losses (24%) and the informal care of people with CVD (22%) [102]. This only serves to increase the immense financial burden on the public purse, and this has certainly contributed to the widespread agreement that CVD is a growing problem that must be tackled using all possible approaches. This includes better education with respect to a healthier lifestyle, and importantly, an increased understanding of the fundamental mechanisms underlying cardiac function.

However, despite the passing of almost four centuries since the publishing of William Harvey's seminal book "*Exercitatio Anatomica de Motu Cordis et Sanguinis in Animalibus*" ("An Anatomical Exercise on the Motion of the Heart and Blood in Living Beings") [50], which arguably founded the field of coronary physiology, our knowledge of cardiac function remains incomplete. In particular, some key phenomena that occur within the heart are not yet fully understood, for example, the effects of tissue deformation on coronary vascular pres-

sure and *vice-versa*, or cell alterations during various levels of ischaemia. Fortunately, novel experimental techniques and improved clinical imaging modalities are providing the necessary tools and primary data to allow scientists confront these great unknowns. Of course, a suitable framework is required to bridge these two data sources which come from opposite ends of the 'clinical spectrum'. Experimentalists, clinicians, and research funding bodies are increasingly turning to the field of computational biology to fulfill this role (see Table 1.1).

As part of this global effort, the present thesis capitalises on novel vascular morphological data to examine some of the fundamental properties of arterial networks. In turn, this knowledge is incorporated into a biophysical and computationally efficient perfusion model, with the overall aims of improving cardiac knowledge, aiding in the diagnostic process for CVD cases, and guiding optimal image acquisition protocols in the clinic.

Project	**Funding**	**Duration**	**Summary**	**Ref.**
euHeart	£19.05m	June 2008 - May 2012	Personalisation and integration of cardiac care	[37]
preDiCT	£5.5m	June 2008 - May 2011	Improve understanding of the mechanisms of negative drug actions on the heart	[111]
2020 Science	£3.99m	May 2011 - April 2016	Mathematical and computational modelling of complex natural systems	[1]
TGCA	$120m	Oct 2009 - Oct 2014	Catalogue genetic mutations responsible for cancer, using genome analysis techniques	[138]

Table 1.1: A sample of the major computational biology research projects either ongoing or of the recent past.

1.1 Background

1.1.1 Cardiac Function

The heart is the primary organ that regulates, through its periodical contraction, the distribution of blood throughout the body. Its function is to provide the uninterrupted supply of substrates necessary to sustain the energy demands of live tissue. This contraction is initiated by an electrical activation sequence driven by the propagation of an action potential. Myocardial cells, called *myocyte*s, contract when they experience an action potential, and the synchronised contraction of myocytes leads to the characteristic pumping action of the heart and pulsatile blood flow (for more information on electrical propagation and calcium dynamics, see generally Katz [72]).

The cardiac anatomy, as depicted in Figure 1.1, is related to its function. The muscular wall of the heart, termed the myocardium, is shown along with the Right Ventricle (RV), Left Ventricle (LV), Right Atrium (RA) and the Left Atrium (LA), through which blood circulates. Blood enters the heart via the atrial chambers, passes into the ventricles and is then pumped around the body. The myocardial walls of the LV are thicker than the RV, as the LV must provide the pressure for the systemic circulation, whereas the RV has only to pump blood to the lungs and back via the pulmonary circulation, which has relatively lower resistance. Generally, the ventricular tissue is classified into three equal-length transmural regions: the endocardium is the inner layer lining the chamber walls; the outer layer is called the epicardium; and the mid-myocardium aptly defines the remaining central third of the tissue.

While the primary function of the heart is to deliver oxygenated blood and

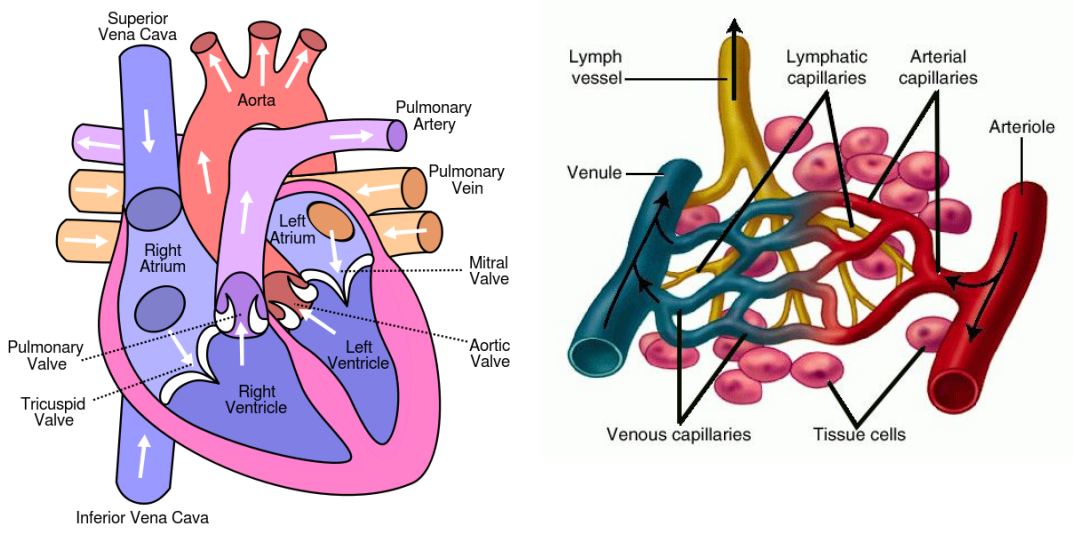


Figure 1.1: (a) Longitudinal cross-section of the heart (apex-base) showing the large scale structural physiology, and arrows indicating the direction of blood circulation. Image courtesy of Wikimedia Commons (http://en.wikipedia.org/wiki/Left_ventricle). (b) A schematic diagram illustrating the blood flow within the microcirculation. The vast majority of metabolite transfer from blood to tissue cells occurs at the capillary level. Image courtesy of The Free Dictionary (http://medical-dictionary.thefreedictionary.com/lymph+capillary).

energy supplies to every living cell in the body, the heart itself requires a constant supply of blood in order to function. The vascular bed responsible for this blood supply is the coronary circulation. In brief, the aorta exits the LV and proceeds to divide into smaller and smaller arteries until they become arterioles, and further subdivision gives rise to capillaries. These are the smallest conducting vessels in the circulatory system, and due to their size, the majority of our knowledge about capillary anatomy is derived from histological studies. The capillaries are organized within the myocyte network and are connected to this network by collagen struts. The distance between two capillaries averages 17μm, and the normal diameter of a myocyte is 18μm, but this can increase

up to 30μm with hypertrophy [66, 68]. Thus, each myocyte is perfused by at least one capillary. Metabolite transfer occurs across the capillary wall, allowing for the importation of glucose and the exportation of the cell's deleterious by-products. The capillaries connect to venules and the blood flow then returns to the RA, mostly through a network of veins converging into the coronary sinus, with a small fraction of the coronary blood supply re-entering the heart's chambers via the Thebesian veins.

Topologically, the coronary arteries and veins have a branching structure (predominantly dichotomous), but the coronary capillaries do not [68]. The capillary density reported in the human heart is approximately 3,100 units/mm^2 [117], and appears to be lower in the epicardium than in the endocardium. The exact reason for this is uncertain, but it is generally believed to be caused by the larger metabolic demand of endocardial tissue due to higher endocardial wall stress and increased systolic compression [15]. This transmural capillary density gradient, coupled with increased pressure at the endocardium, has important effects on the location of ischaemic events. The necrotic core of hypoperfused regions is typically found in the endocardium, with subsequent circumferential and radial spread [51, 144].

1.1.2 Clinical Context

CVD is caused when blood supply to the heart is impeded by disease either in the large vessels, or the small vessels forming the microcirculation. It typically presents as either a Myocardial Infarction (MI) or *angina pectoris*. A common cause of CVD is coronary atherosclerosis, whereby an atherosclerotic plaque develops in the coronary arteries over many years. Once a plaque reduces

the luminal diameter by greater than 70%, blood flow to the myocardium can be reduced by such an extent to cause *angina pectoris*, and the severity of the impedance depends on the site of the narrowing. A stable plaque is a source of chronic CVD, however, if an unstable plaque ruptures an acute MI can result from the subsequent *thrombosis*. Known risk factors such as cigarette smoking, hypertension, diabetes, diet and genetics affect the development of these atherosclerotic plaques [102]. Atherosclerosis is unfortunately not the only cause of CVD, as the following list testifies: coronary vasospasm; microcirculatory diseases; hypertrophic cardiomyopathy; dilated cardiomyopathy; cardiac arrhythmias; myocarditis; amyloidosis; valvular heart disease *etc.* Any one or a combination of these diseases can cause perfusion defects, potentially leading to hypoxic cell states, ischaemia (the underperfusion of muscle tissue) and even MI.

Prevention of CVD can be aided by many methods: sometimes a lifestyle change is sufficient; an improved diet; pharmaceutical treatment can be recommended *e.g.* the use of statins or aspirin. With respect to medical treatment, a stenosis, or coronary occlusion, can be countered via a variety of measures, the optimal choice of which is case-specific *e.g.* Percutaneous Coronary Intervention (PCI) via balloon angioplasty and/or the implantation of a stent. In more extreme cases, one may need coronary artery bypass surgery, or even a heart transplant.

With so many ailments that can strike the heart (only a fraction of which have been listed above), it is often difficult for the cardiologist to determine the correct diagnosis. Patients with quite severe CVD may not even be symptomatic, making early detection of life-threatening problems all the more unlikely. Providing succinct diagnostic information to the clinician could aid this process.

Thus, in the following section, the current conventional approaches to obtaining further knowledge of cardiac function are reviewed.

1.1.3 Clinical and Experimental Data

Currently, diagnosis of CVD can involve several tests/scans including: Electrocardiography (ECG) interprets electrical activity; Exercise Tolerance Test (ETT) can detect coronary artery disease; Echocardiography (ECHO) provides cardiac structural and performance information; myocardial perfusion imaging using Single Photon Emission Computed Tomography (SPECT) or Magnetic Resonance Imaging (MRI) can detect perfusion defects; X-Ray Angiography (XRA) can reveal the coronary artery anatomy; Positron Emission Tomography (PET) is regarded by many to be the current non-invasive gold standard test for perfusion defects; and MultiSlice Computerised Tomography (MSCT) is rapidly being developed for perfusion imaging also. However, there is no "catch-all" diagnostic procedure and the tests/scans undertaken very much depend on the facilities available, the speciality of the cardiologist, and patient-specific factors. Furthermore, some of the aforementioned modalities have serious disadvantages: ECHO gives poor results for obese people and those suffering from chronic obstructive pulmonary disease; SPECT, PET and MSCT involve ionizing radiation, with a single scan typically providing a dose of between $10 - 20$ millisieverts; and MRI cannot be used if the patient has an embedded metal object that is not MR compatible. Despite the individual limitations, there is a synergistic benefit to the wide-range of tools available to the cardiologist. MRI is of particular relevance to this thesis, as it is arguably increasing in prominence in relation to perfusion-related defects, for reasons that shall be described below.

MRI is a noninvasive medical imaging technique used in radiology to visualise internal anatomic structure and cardiac functionality by detecting the induced, rotating magnetic field of hydrogen atoms to distinguish amongst tissue types [12]. In addition to inherent tissue contrast, there are exogenous agents that can be applied to tissues or organ systems that cause significant alterations of the local magnetic field (specifically in the local T1 and/or T2 relaxation times). These agents are called MRI contrast agents and, depending on the type of agent used, can cause either positive (increased signal intensity) or negative (decreased signal intensity) contrast enhancement in MRI images of tissues or organs where the agent has accumulated [33]. There are many such contrast agents (including chelated gadolinium (Gd^{3+}), manganese (Mn^{2+}), and iron (Fe^{3+})) – all of which have their unique intrinsic properties. The resolution of MRI is generally worse than that of SPECT and PET [110], especially during perfusion tests. This is likely to improve with better scanning protocols and the standard introduction of 3T machines (up from the current norm of 1.5T, see Figure 1.2). Furthermore, the current typical resolution $1.5 \times 1.5 \times 8$mm [60] still allows for an estimation of the volume of a hypoperfused region, and its location within the myocardium (which is important for differentiating amongst cardiomyopathies). Nevertheless, MRI does not detail the underlying coronary vasculature.

In fact, the best vascular resolution that can be achieved in the clinic is given by XRA, which is the standard modality used for the diagnosis of coronary stenosis. The conventional use of XRA cannot reliably estimate structures smaller than 1mm however (some model-based techniques are seeking to improve this however [18]), and thus from a patient-specific point of view, treatment must be determined with knowledge of the larger coronary arteries alone. This lack of a direct *in vivo* method to image detailed coronary anatomy poses a significant

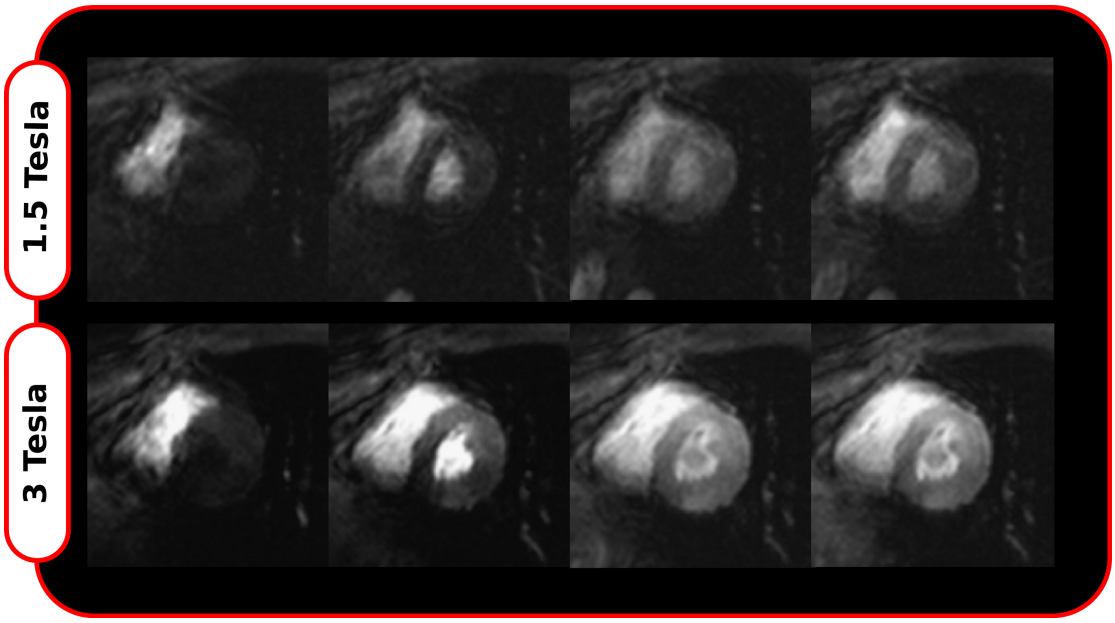


Figure 1.2: Multiple images taken during a perfusion MRI scan using late-enhancement Gadolinium contrast agent. The images are reproduced from Araoz et al. [5] whereby a clinical study on the improvements of using a 3Tesla (T) over a 1.5T machine was undertaken. Note that the usual perfusion pattern can be observed in the images from left-to-right *i.e.* the contrast agent first appears in the right ventricle, then the left ventricle, and finally perfusing the myocardium itself.

barrier to our fundamental understanding of coronary haemodynamics, and hence experimental data must be used to guide our understanding of cardiac function and model development.

There is a myriad of experimental modalities used to investigate vascular networks and *angiogenesis*, as testified by several reviews in the literature [29, 144, 152]. Many of these modalities are not able to render the desired full spatial characterisation of coronary networks, due to varying reasons, such as a limited field of view (multiphoton laser scanning microscopy, electron microscopy), superficial acquisition depth (Doppler ultrasound, optoacoustic imaging, orthogonal polarization spectral imaging, optical frequency domain imaging), or are unsuitable for imaging organs of the scale of tens of centimetres (MR microscopy, confocal laser scanning microscopy). Although, as shall be described

shortly, there are also a number of experimental procedures that can provide vascular data at the desired scale and resolution.

In the past, stereo-angiography has been used to visualise coronary arteries in 59 post-mortem human hearts with the use of a radiopaque contrast medium [46]. This technique was used in seminal studies to reveal new information about coronary collaterals and the role of shear stress in remodelling, however, they were essentially 2D maximum intensity projection images. Vascular casting was subsequently applied to reveal the 3D characteristics of arterial trees. One approach is to fill the coronary microcirculation with silicone elastomer and render the surrounding tissue translucent via bathing the heart in ethanol [7]. Alternatively, one can entirely corrode the tissue with a concentrated acid or base [69, 146]. Statistical descriptions of the studied networks were derived and used in synthetic network generation [62, 128], but knowledge about the spatial relationship between the vessels and the tissue was lost during this casting process. X-ray microcomputerised tomography (micro-CT) faces the same challenge, except that it has the considerable advantage of being able to noninvasively provide images of the coronary microcirculation. Micro-CT has enormous potential as it can scan 1mL volumes at 10μm resolutions [161], yet this technique remains to be successfully upscaled to larger organs while retaining this resolution.

The challenge to obtain whole-organ, high-resolution anatomical vascular data from larger species such as the pig or human, while also retaining the spatial link between the vessels and the tissue, has been addressed by episcopic cryomicrotome imaging. It is a form of surface imaging microscopy capable of resolving large anatomical networks at 25μm. This imaging modality provides

some of the key data used in this thesis, and given its fundamental importance, it is discussed in detail in Section 3.1.

1.2 Previous Work

In the previous section, the complex functionality and structure of the cardiac system was outlined, as well as the confounding factors that hinder our understanding of cardiac function. To further contextualise this thesis, the mathematical models of perfusion that were designed to overcome these obstacles are reviewed next, followed by a discussion of myocardium-vessel interaction.

1.2.1 Perfusion Modelling

1D flow models

Coronary blood flow occurs across many scales, as the diameter of the human aorta is of the order 10^{-2}m whereas the diameter of a capillary is of the order 10^{-6}m. Blood flow in the larger vessels can generate complex secondary flows at curves and bifurcations, and is further complicated by the fact that vessel walls are compliant. Three-dimensional Navier-Stokes models on movable domains can be employed to resolve the flow in such vessels [41, 108], but given the large number of coronary vessels however, the computational cost of applying these 3D models to all vessels would be phenomenal. Thus, for investigation of unsteady blood flow in a network of elastic vessels, the most popular class of models is the one which approximates the blood vessel as a one-dimensional elastic tube and describes conservation of mass and momentum in the space-time domain.

Various numerical studies have demonstrated the computational advantages of the 1D approach. These studies have a common root in a basic underlying mathematical model which was first proposed by Leonhard Euler in 1757 [38]. These equations, which described the conservation of mass and balance of momentum for inviscid fluid flow, were later applied by Euler to model blood flow within the human arterial system [39]. The Euler equations are nonlinear hyperbolic equations and their general solutions are waves - however Euler did not realise this at the time and it was in fact Thomas Young that first scientifically described the wave-like nature of blood flow in the arteries [163]. The focus of more recent work has been to achieve an efficient computational solution of the governing equations, using both finite difference [130] and finite element techniques [43], including high-order spectral element method implementations [124]. It is noteworthy that some of these studies [43, 124, 130] extended the model to couple the terminal points of 1D vessels to lumped-parameter models, thus allowing flow in a network to be calculated while taking into account distal resistances of vessels not explicitly represented [6, 14]. The development of these terminal resistance type phenomenological models was based on the intramyocardial pump theory of Spaan, Breuls, and Laird [131], and they have been used to reproduce the observed flow responses to arteriole and venule pressures of an anatomically based model combining non-linear resistive and capacitive elements. These discrete model types are particularly useful for investigating vascular wall properties [137] and the rheological properties of blood [80]. 1D flow modelling is a reasonable way of reproducing experimentally observed behaviour while maintaining some of the fundamental physics of the problem.

However, it still suffers from three major limitations: *(i)* it is not suitable for

use in modelling local metabolite delivery and interpretation or prediction of contrast MRI results where the detailed structure is not available, *(ii)* its computational tractability has not been demonstrated for coronary flow modelling due to the time-step constraints imposed by the wavespeed and characteristic length of the heart (coronary vessel wavespeeds are approximately 20m/s whereas the human heart is 10-15 cm in length [75]), and *(iii)* it is impossible to measure flow in all vessels and thus fully validate such models for clinical application, or determine suitable 1D model pressure/flow boundary conditions (BCs).

Given the difficulties of the aforementioned 1D discrete models, it is appropriate at this juncture to discuss the findings of Henri Philibert Gaspard Darcy, a French engineer. In 1856, Darcy experimentally demonstrated that the volume of water (Q), passing vertically downwards through a column of sand of depth h and of surface area s, could be expressed via

$$Q = ks(H + h)/h,$$

where H is the height of the water above the sand (*i.e.* the pressure head), and k is a coefficient dependent on the nature of the sand, called the permeability of the medium. Although, he did not explicitly state so, one could reasonably assume that Darcy was aware that k incorporated the physical properties of the fluid and the porous media, or sand in this specific case. The above formation of what has become known as *Darcy's Law* is essentially an empirical 1D porous flow model, however, it has since been extended to three dimensions and been derived from the Navier-Stokes equations via formal homogenisation [53]. Thus, considering its origins, it is unsurprising that Darcy's Law is typ-

ically assumed for the purposes of modelling fluid transport within a porous domain, whereby flow is defined to be the product of the pressure gradient and the permeability of the medium, with flow proceeding from areas of high pressure to low pressure [8].

Non-explicitly parameterised 3D perfusion models

This section details the previous continuum modelling efforts that do not rely on an explicit vascular anatomy for parameterisation purposes. As well as being computationally tractable, a continuum model of perfusion has some distinct advantages over the discrete alternatives mentioned in the preceding section: *(i)* it has a continuous spatial treatment of the microcirculation *i.e.* it does not use lumped parameters; *(ii)* the main clinical interest is often focused on regional perfusion states, typically expressed in terms of capillary pressure and flow. Therefore a continuum approach to blood perfusion, describing blood flow by averaged quantities, would be appropriate; *(iii)* clinical perfusion data, be it PET, SPECT or MRI, is inherently spatially averaged, thus making comparisons to a continuum model the intuitive choice.

The challenge is to formulate and parameterise a continuum model in a sensible manner, often by extracting effective or macroscale parameters from more elaborate microscopic models. The formal theory of homogenisation is one such technique for making this scale transition, and has been used successfully for estimating microscale flow within rock formations [86], for studying the mechanics of perfused myocardium [92], and for producing a 3D model of fluid flow and transport within both healthy tissue and tumor regions [20]. Despite providing an elegant method of separating flow at the various vessel scales under consideration, formal homogenisation requires a repeating unit, or periodic

'canonical cell'. As biological arterial networks are aperiodic in nature, a different method of parameter derivation is required for a perfusion model based on realistic networks.

The multi-compartment porous model of Huyghe et al. [58] allows for scale separation of the flow and does not require any periodicity of the material properties. Furthermore, complementary to the discrete model types, porous perfusion models have the ability to determine the pressure and flow in a continuous manner across the 3D computational tissue domain [19, 24, 97]. In this model, fluid flows through compartments of decreasing arterial radius, into a capillary compartment, and is then drained via compartments of increasing venous radius. The sequential flow amongst compartments is an assumption that greatly simplifies the model and reflects upon the idea of an underlying idealised network, although no actual discrete network is referenced. Due to the lack of a vascular model, their approach to the permeability tensor field was to assume isotropic tensors, proportional to the square of the intramyocardial blood volume under a constant vessel length assumption.

The 3D perfusion models mentioned thus far lack the ability to capture fluid-solid interactions. In Huyghe et al. [57], the authors applied a mixture theory model to the mechanics of the left ventricular myocardium. This was a two-phase mixture model featuring a solid component and a fluid component. It allowed for finite deformation of the tissue, and was fundamentally based upon the work of Biot [9] and Bowen [13]. As their model consists of a single porous domain the authors admit to not being able to model physiological coronary blood flow, in the sense of a flow from arteries to veins.

More recently, Chapelle et al. [19] presented a derivation of a general single-

compartment nearly-incompressible poroelastic model which experienced finite deformations and featured active contraction, fibre orientation, spatially distributed volumetric fluid influx, and an isotropic permeability tensor field (see Appendix B for a brief discussion of the poroelastic framework for flow modelling). While this paper represents a significant contribution to the model development of cardiac perfusion, it largely relied on unphysiological parameters (see Table 1.2). It was sufficient, however, to reproduce some known mechanical effects resulting from the mechanisms of cross-talk between the myocardium and coronary flow, such as a decrease in myocardial volume and flow impediment during contraction, and a non-linear transmural pressure field. Interestingly, the lack of an explicit representation of the arterial and venous vessels is flagged as a major limitation of their model, a factor which is blamed upon a lack of sufficiently detailed measurements to both parameterise and validate the model.

Explicitly parameterised 3D perfusion models

A more realistic attempt to model perfusion in biological tissues was undertaken by Vankan et al. [149]. This was also a multi-compartment perfusion model, accompanied by an explicit synthetic network created using a Constrained Constructed Optimisation (CCO) algorithm [122]. A spatial averaging technique, utilising a moving averaging window, was used to derive the permeability fields for each Darcy compartment, and the inter-compartment coupling terms. This technique was derived in Huyghe and Van Campen [55] and makes use of the Slattery-Whitaker spatial averaging theorem. Although derived for a 4D Darcy model, whereby the fourth dimension allowed for volume coupling between neighbouring 3D porous compartments, Vankan et al. [149] only simulated 2D porous domains (presumably as this is in accordance with a standard

3D Darcy solver). Furthermore, their range of simulations were limited and confined to simple idealised vascular models. The metric they applied to compare the continuum model results with discrete results from a Poiseuille flow model was not spatially comprehensive, as they chose to focus only on total flow through the computational domain.

Note also that this pioneering model neglected the connections known to exist across non-neighbouring compartments. Such a vascular structure is in contrast to the seminal histological studies of Kassab *et al.* that report significant cross-Strahler ordering connectivity (see Table 1.3 and [69]). Strahler ordering is a method developed by Robert Horton and Arthur Strahler originally to quantify the branching complexity of river systems [135], but it has since been applied to other branching objects such as vascular networks [69]. One may assign a Strahler order to all vessels of a network, in bottom-up order, as follows:

1. If the vessel is a terminal distal vessel, its Strahler order is one.

2. If the vessel has a daughter vessel with Strahler order i, and all other daughter vessels have Strahler orders less than i, then the Strahler order

Model	**Muscle type**	**Isotropic K**	**Multi-compartment**	**Source of K value**
Huyghe *et al.* [58]	Cardiac	No	No	Huyghe et al. [58]*
Vankan *et al.* [149]	Skeletal	Yes	No	Braakman et al. [14]
Chapelle *et al.* [19]	Cardiac	Yes	No	Huyghe et al. [58]

Table 1.2: List of non-explicitly parameterised perfusion models and their main features. *Estimated using few experimental studies with significant variance in results. The chosen K value has been acknowledged by the authors to be a "rough estimate of the order of magnitude of the parameter".

of the vessel is i again.

3. If the vessel has two or more daughter vessels with Strahler order i, and no daughter vessel with a greater Strahler order, then the Strahler order of the vessel is $i + 1$.

The term "cross-Strahler ordering connectivity" can now be understood in terms of connected vessels with difference in Strahler ordering that is greater than one (see Figure 1.3 for a schematic of Strahler order assignment). Despite the decrease in the number of connections with compartment separation order, the fact that the pressure difference simultaneously increases means that these long-range intercompartmental effects could be quite significant. This cross-Strahler ordering, or non-neighbouring porous compartment connectivity, is a feature of anatomical vascular models that is not captured by the synthetic networks used by Huyghe and Vankan. The significance of allowing general connectivity amongst compartments is considered in this thesis.

1.2.2 Coronary Structure and Deformation

Arguably, none of the models discussed in the previous section took adequate account of the proposed effect that tissue deformation has on the structure of the underlying vasculature. Structural knowledge of the intramural coronary vessels is important for the understanding of flow and oxygen distribution within the myocardium, as evidenced by direct visualisation of the coronary tree which has shown varying functional roles for vessels of a particular scale. For example, small transmural arteries with diameters in the range $150 - 300\mu$m are predominantly radial in orientation and serve the function of rapidly

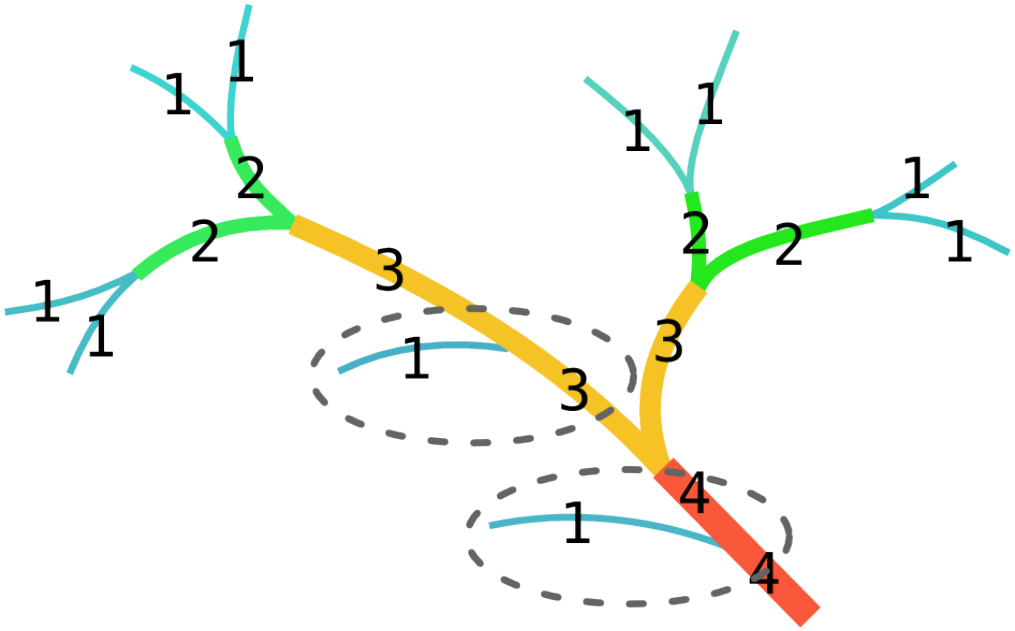


Figure 1.3: A simple branching network with assigned Strahler order. See the main text for an algorithm detailing the order assignment process. Two examples of cross-Strahler ordering connectivity have been highlighted by grey dashed ellipses. Note that a simple continuously-bifurcating network would not have cross-Strahler ordering (figure adapted from `http://en.wikipedia.org/wiki/Strahler_number`).

distributing blood to the mid-myocardial and sub-endocardium, whereas pre-capillary arterioles have a shorter length and a more heterogeneous orientation [132]. It is also known that the composition of vascular walls, in terms of both the number of smooth muscle layers and collagen fraction, vary with vessel location and diameter [48]. Tissue deformation effects are also experienced by the capillary bed which is distensible, a fact that is crucial to the perfusion of a tissue that is constantly contracting and relaxing

In fact, with typical strains of between 10–20%, normal LV pressures of between 0–120mmHg, and normal aortic pressures of between 70–120mmHg, the role played by mechanical 'cross-talk' in the functioning heart is thought to be quite significant, but is far from being fully understood [155]. Some

known mechanisms of interference between the mechanical state of the tissue and the coronary vascular pressure are: *(i)* the intramyocardial pressure (during systole, coronary artery inflow is impeded, or even reversed, and venous outflow is augmented), *(ii)* vascular deformation, *(iii)* the "garden-hose effect" (increased vascular pressure causes an increase in ventricular stiffness), and *(iv)* stretch-activated changes to myocyte force generation (*i.e.* invocation of the Frank-Starling mechanism via increased coronary flow rate or increased afterload (*a.k.a* the Gregg and Anrep effects respectively) [78]).

While much has been reported in the literature about the importance of fluid-solid mechanical coupling particularly with respect to flow impedance and tissue stiffening [155], the orientation and constitution of the vessels themselves have been largely ignored. However, a notable exception to this general observation is the study of of May-Newman *et al.* [92–94] where the structural basis of coronary pressure and its relation to myocardial strain has been investigated through *ex vivo* experimentation and the mathematical modelling of composite myocardial properties, such as the garden hose effect, at the capillary level. These authors astutely observed that within the mathematical modelling literature, the deformation of the myocardium is transmitted to the coronary vasculature through changes in intramyocardial pressure only. This is not representative of known physiology, as detailed structural imaging of the myocardium has shown that forces from the tissue are also transmitted to the vessels by the extracellular matrix connections tethering the fibres and vessels together.

Thus, it is reasonable to hypothesise that tissue deformation also inherently deforms the embedded vasculature. This deformation effect has not yet been quantified, primarily because there is currently no way to directly image the de-

forming network. There are however, techniques to obtain tissue deformation and strain data, such as tagged MRI [162] and speckle/feature tracking [88]. A mathematical model is thus a suitable vehicle to combine transient strain data and static vascular data to finally examine the properties of a realistically deforming coronary network, and provide an improved description of the interaction between ventricular mechanics and coronary perfusion.

1.3 Thesis Objectives

As outlined above, perfusion is the fundamental cornerstone of a functioning organ. Mathematical models of the tissue deformation and transport systems can help elucidate the underlying systemic processes, enhance our knowledge of organ physiology, test hypotheses not feasible to test on a patient, and optimise data acquisition. The challenge of this project is to optimally exploit the clinical applicability of novel structural information, and to link this information with the validational potential of perfusion data via an appropriate mathematical framework that is both principled and robust.

Precisely, the overall objective of this thesis is to replace the intractable problem of using discrete flow models within large vascular domains with a suitably parameterised continuum perfusion model. Hence, beginning with static perfusion models, the **first aim of this thesis** is to establish if continuum models can approximate the flow predicted by discrete models within realistic vascular networks. After a "proof-of-concept" demonstration, the **second aim of this thesis** is to elucidate some of the key differences between anatomical and idealised arterial networks using our established parameterisation approach.

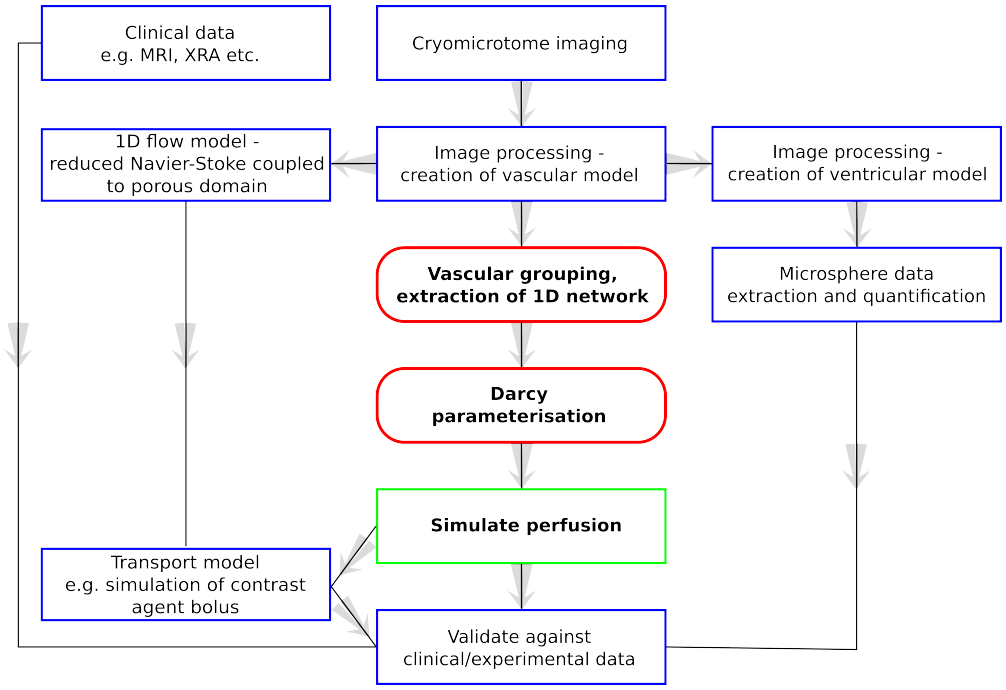


Figure 1.4: The coronary perfusion modelling pipeline. This flow-chart represents the entire myocardial perfusion modelling process being undertaken by our research group. Sections in blue are led by other team members, whereas sections in red are entirely my own work. Experimental data is obtained via collaboration with the Department of Biomedical Engineering, King's College London and the University of Amsterdam, Academic Medical Centre.

Armed with our experience from these static scenarios, the parameterisation process will be extended to whole-cycle dynamic simulations while fully applying the knowledge gained from the static scenario. One of the eventual aims of the perfusion model is to be applied clinically, however this is highly dependent upon what is called "clinically-relevant" solution times. On the shortest time scale, the door-to-balloon time can be as short as 90 minutes in the case of a patient arriving at the hospital with an ST-segment-Elevation Myocardial Infarction (STEMI) [95], motivating the need to reduce the time of computation. Thus, temporal updating of the continuum flow model parameters should be done in a manner that is as computationally efficient as possible, while still yielding reasonable results. In this context, the **third aim of this thesis** is to for-

mulate and implement a computationally efficient method of updating the fluid parameters while the tissue model is undergoing a typical cardiac deformation. An immediate application of the methods developed to tackle this latter aim would be a study of the structural changes that occur to the arterial network during cardiac contraction and relaxation.

While the first aim of this work has been alluded to in a number of previous perfusion modelling papers [19, 149], it has yet to be demonstrated in a 3D vascular network, nevermind attempted with a physiologically realistic network. The current approach also stands in contrast to previous works in that it offers a novel combination of anatomically correct geometry, both in terms of the vascular model and the tissue model, as well as the realistic prospect of use within a physiologically integrative modelling framework *i.e.* improved biophysical realism in terms of fluid-solid coupling. This is a significant departure from using ellipsoidal or even cubic tissue geometries with an idealised underlying vascular network [19].

This research contributes to the basic perception of the mechanics of perfused biological tissues, and its results are of significance to a wide range of computational modellers in numerous fields *e.g.* biomechanics, haemodynamics, and physiology. In time, and with step-by-step validation, the methods developed in this thesis will enhance the patient-specificity of tissue perfusion models for use within a clinical setting (see Figure 1.4 for a schematic of the perfusion modelling pipeline used within our research group). Future uses of a physiologically realistic perfusion model may be optimisation of clinical imaging protocols, quantifying regions of defective perfusion, and improved understanding of tissue energetics and vascular/structural remodelling.

1.4 Thesis Outline

Continuing from this introduction, Chapter 2 describes the parameterisation methods applied to a static perfusion model with an underlying synthetic vascular model. The cryomicrotome experimental procedure, vascular model creation and subsequent manipulation is detailed in Chapter 3. Both canine and porcine anatomical arterial networks are used to parameterise left ventricle perfusion models in Chapter 4. The effects of a realistic cardiac deformation on the fluid-related parameters will be considered in Chapter 5. Finally, the main conclusions of this dissertation, and a discussion of the salient points raised herein are given in Chapter 6, as well as potential future directions to continue this work.

Summary

Coronary vascular diseases are a major killer, yet our knowledge of cardiac function is far from complete. With increasing volumes and types of both clinical and experimental data, it should be possible to better characterise, diagnose and treat such diseases. Mathematical models can play a large role in that process, optimising the use of such data, and providing information on variables that cannot be directly imaged. However, perfusion of biological tissues is a complex process, and while a simplistic perfusion model may reveal some pertinent findings, this model should be computationally tractable and data-driven in a biophysical manner. We hypothesise that discrete vessel data can be used within 3D continuum perfusion models providing increased anatomical realism, and allowing for the tractable solution of blood flow and pressure. This thesis uses both synthetic and anatomical vascular networks to parameterise our continuum perfusion model. It systematically investigates parameterisation techniques for static and dynamic perfusion scenarios, and its findings have clear implications for future perfusion models.

Order	1	2	3	4	5	6	7	8	9	10
0	3.18±0.12	0.68±0.08	0.15±0.08	0	0	0	0	0	0	0
1	0.14±0.03	2.05±0.07	0.63±0.12	0.07±0.07	0	0	0	0	0	0
2	0.09±0.03	2.24±0.10	1.50±0.27	0.06±0.03	0.09±0.02	0.02±0.01	0	0	0	
3	0	0	0.07±0.04	2.10±0.20	0.38±0.06	0.01±0.02	0.12±0.03	0.09±0.03	0.03±0.03	0
4	0	0	0	0.14±0.10	2.25±0.10	0.43±0.04	0.38±0.05	0.43±0.07	0.30±0.10	0.17±0.17
5	0	0	0	0	0.24±0.04	2.50±0.07	1.91±0.11	1.56±0.17	1.36±0.28	0.67±0.33
6	0	0	0	0	0	0.15±0.02	2.50±0.08	1.58±0.16	1.48±0.32	1.18±0.65
7	0	0	0	0	0	0	0.12±0.02	2.09±0.11	1.30±0.30	2.00±1.09
8	0	0	0	0	0	0	0	0.06±0.02	2.50±0.21	2.50±1.06
9	0	0	0	0	0	0	0	0	0.12±0.06	3.33±1.12
10	0	0	0	0	0	0	0	0	0	0.10±0.10

Table 1.3: Connectivity matrix of pig left anterior descending artery and subvessels adapted from Kassab et al. [69]. Values are means ± standard deviation (both rounded to two decimal places). An element (m,n) in m^{th} row and n^{th} column is ratio of total number of elements of order m that spring directly from parent elements of order n divided by total number of elements of order n.

2

Darcy Model Parameterisation: Application to a Synthetic Network

In this chapter, the process of incorporating vascular data into a continuum porous model is outlined. The multi-compartment Darcy porous flow model is further motivated ahead of a presentation of its system of equations. Section 2.2.1 describes the generation of a discrete synthetic vascular model from which the continuum porous domains are parameterised. In Section 2.3.2, a new method of permeability homogenisation is developed and two existing approaches found in the literature are described, specifically a porosity-scaled isotropic permeability field and spatial-averaging *à la* Huyghe and van Campen (HvC). All three parameterisation methods are quantitatively compared across the entire porous domain via a pressure-based root-mean-square (rms) error to the spatially-averaged Poiseuille pressure. For this controllable synthetic network, a good qualitative match results from the HvC method, as described in Section 2.4. Furthermore, these comparisons are conducted across a wide range of spatial-averaging window sizes, demonstrating a clear sensitivity to this size, but also a robustness of the HvC method within the considered vascular range.

2.1 Continuum Darcy Model

As outlined in the previous chapter, it is often infeasible to treat the transport phenomena on the microscale, when seeking a numerical solution to real-world flow problems. For example, there may be a dearth of geometric detail with regards to the fluid-solid interface, and/or the computational cost of such an explicit modelling approach is prohibitive. For such cases, one may seek to replace the physical geometry by a simplified continuum porous medium model. In this manner, each point of the porous domain has a value assigned to it for the relevant variables and parameters of the model, such as increase in fluid mass, velocity, pressure *etc.* These model values represent the variable/parameter averaged over a Representative Volume Element (RVE) centered at the point in question (see Figure 2.1). It is a non-trivial issue as to how these averaging procedures should be carried out, in effect taking what can be complicated microscopic details and transforming them into a simplified macroscale version. In this section, the assumption of a continuum Darcy model of biological perfusion is motivated and the model itself is presented.

2.1.1 Multi-compartment Motivation

Given the disadvantages of 1D flow models discussed in Section 1.2.1, porous flow models, such as Darcy's Law, provide a promising alternative framework as evidenced by previous perfusion models for biological tissues [19, 147]. However, the multi-scale nature of vascular trees makes the use of a typical single-compartment Darcy model inadequate if one is interested in the flow characteristics at the smaller scales, due to the close spatial proximity of vessels with

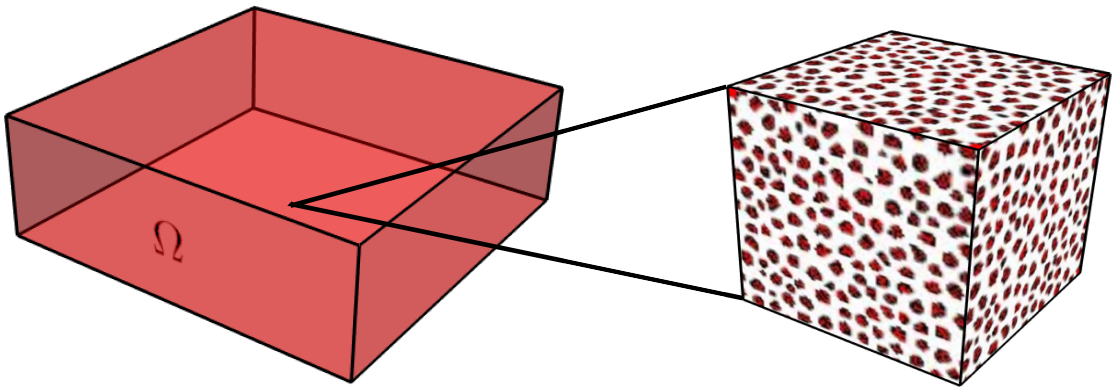


Figure 2.1: The macroscale porous domain, Ω, is shown on the left, with a representation of the microscale shown on the right. The terms *macroscale* and *microscale* are relative to each other, and imply that there is at least an order of magnitude of difference in characteristic length scale between the two. The porous model assumes a superposition of both solid and fluid phases at each point of the domain, with the parameter values for the macroscale point being related to the associated microscale region via a homogenising process.

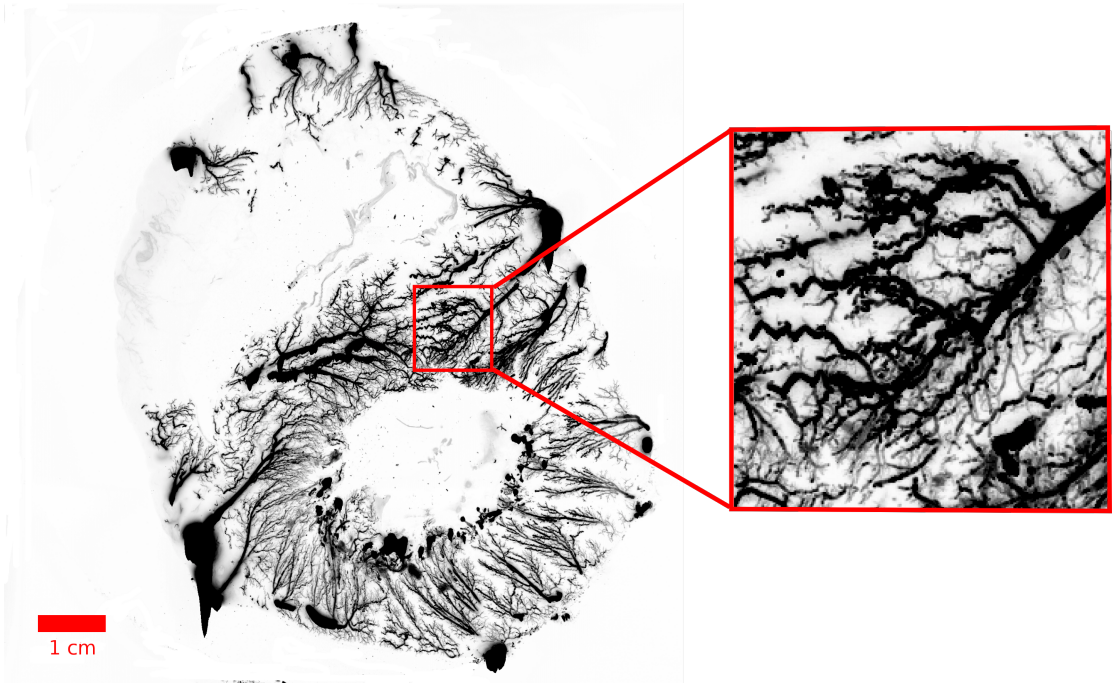


Figure 2.2: The main figure is a 2mm thick maximum intensity projection image created from a porcine cryomicrotome data stack. A 1.25cm in-plane septal section has been enlarged and is shown on the right. Smaller, less intense, vessels are clearly seen to be interspersed with the larger, more intense vessels.

widely varying length and pressure scales. This physiological feature of perfusing networks has been previously commented on by Spaan et al. [132], and can

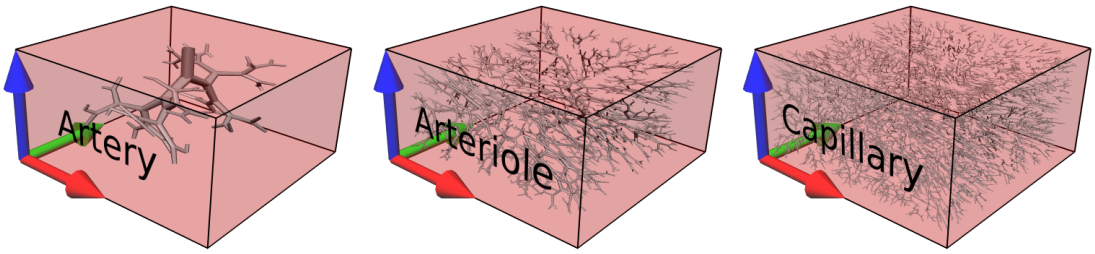


Figure 2.3: Illustration of multiple spatially coexisting Darcy compartments. Each point of the physical domain Ω will have a set of parameters and state variables for each compartment, with the particular parameters dependent on the vessels assigned to the compartment after vascular model partition. Note the decreasing scale of vessel in each compartment from left-to-right.

clearly be seen in cryomicrotome data (see Figure 2.2). This indisputable evidence gathered by direct visualisation is in accordance with our current physiological knowledge, as to supply all cells with the required metabolites (in tissues with low diffusive properties), then smaller scale vessels such as precapillary arterioles must be almost ubiquitous within the tissue. Naturally, this includes small vessels that neighbour vessels that are several orders of magnitude greater in scale. Thus, to characterise the flow occurring at various scales, the approach taken here is to employ *multiple* porous compartments, with each compartment representing a different range of vascular scale. This approach has been successfully applied both by our research group [24, 59, 97], and by others [19, 55].

2.1.2 Multi-compartment Static Darcy System

The multi-compartment static Darcy system is an extrapolation of the single compartment Darcy model to N porous domains, and has been applied to several perfusion modelling problems [24, 59, 97, 148] (see Figure 2.3 for a

schematic). The Darcy system for compartment $i \in [1, N]$ is [1]

$$\boldsymbol{w}_i + \boldsymbol{K}_i \cdot \boldsymbol{\nabla} p_i = 0 \text{ in } \Omega, \tag{2.1.1a}$$

$$\boldsymbol{\nabla} \cdot \boldsymbol{w}_i = s_i - \sum_{k=1}^{N} \beta_{i,k}(p_i - p_k) \text{ in } \Omega, \tag{2.1.1b}$$

where subscripts i and k are compartment indices, $\boldsymbol{K}$ is a permeability tensor of the material, $\boldsymbol{w}$ and p denote the Darcy velocity and pore pressure respectively, s is a source field, and β is the array of inter-compartment pressure-coupling coefficients. Eqs. (2.1.1) are set on an open bounded domain $\Omega \subset \mathbb{R}^{nd}$ with spatial dimension nd and a piece-wise smooth boundary $\partial\Omega$, upon which zero flux boundary conditions are enforced. For the synthetic network simulations featuring in this chapter, $\Omega = [-1, 1]^3$mm. Given that there are no overall volumetric changes to the domain Ω and the assumption that the domain is fully saturated, it follows that the volume of fluid that enters Ω must equal the volume of fluid that exits Ω. This, coupled the aforementioned zero-flux boundary conditions on the boundary of Ω, implies a compatibility condition of

$$\sum_{i=1}^{N} \int_{\Omega} s_i \, dv = 0, \tag{2.1.2}$$

in its general form. In practice however, $s_i = 0$ for $i = 2, ..., N-1$, and thus

$$\int_{\Omega} s_1 \, dv = \int_{\Omega} s_N \, dv, \tag{2.1.3}$$

where $s_1(s_N)$ represents the fluid influx(efflux) into(out of) Ω. As shall be seen shortly, Dirichlet pressure BCs are applied in the simulations of this chapter, thus further discussion of the s_i is deferred until Section 4.1.3.

[1] Einstein summation is not in use

Note that $\beta_{i,k} \in \mathbb{R}_0^+$ and $\beta_{i,k} = \beta_{k,i}$ for $i,k = 1,\ldots,N$ in order to conserve fluid mass across the system (see Eq. (2.3.10)). For example, consider a point $x \in \Omega$ such that $p_i(x) > p_k(x)$ and ignore the external volumetric source fields s_i. To ensure that fluid flows from regions of higher pressure to lower pressure (this is a typically desired feature of Darcy flow models) and given the sign of the right hand side of Eq(2.1.1b), we thus require $\beta_{i,k} > 0$. Under these conditions, we can now recognise $-\beta_{i,k}(p_i - p_k)$ to be a volumetric sink field from the perspective of compartment i, and conversely, $-\beta_{k,i}(p_k - p_i)$ is a volumetric source field from the perspective of compartment k. Conservation of the fluid mass transported between these two compartments implies $-\beta_{i,k}(p_i - p_k) = -\beta_{k,i}(p_k - p_i)$ which reveals the equality $\beta_{i,k} = \beta_{k,i}$. Note that the specific formulation of $\beta_{i,k}$ is presented in Section 2.3.3. In conclusion, volumetric source terms allow for inter-compartment flow scaled by the relevant pressure differences, whereas intra-compartment flow represent the flow for the set of vessels within a defined scale range (see Section 2.3.2).

The permeability tensor field, $\boldsymbol{K}$, is the constant of proportionality linking the Darcy velocity, $\boldsymbol{w}$, to the pressure gradient. $\boldsymbol{K}$ is a material property of the porous medium, and it has some key attributes that are related to the physical constraints of the system [8]:

- $\boldsymbol{K}$ is symmetric, by the Onsager's reciprocal relation. In other words, this ensures that there is no bias in the material and a reversal in the pressure gradient should bring about a corresponding reversal in flow.
- $\boldsymbol{K}$ is positive definite. This property ensures that the direction of flow is always in the same direction as the pressure drop *i.e.* fluid flows from volumes of high pressure to lower pressure.

- By corollary, the fact that $\boldsymbol{K}$ is Symmetric Positive Definite (SPD) implies (this is actually an equivalence relationship) that it is always diagonalisable and can be decomposed into its principal components, *i.e.*

$$\boldsymbol{K} = VDV^{-1}, \tag{2.1.4}$$

where V is the square matrix whose i^{th} column is the i^{th} eigenvector v_i of $\boldsymbol{K}$, and D is the diagonal matrix whose diagonal elements are the corresponding eigenvalues, *i.e.* , $D_{ii} = \lambda_i$ and $\boldsymbol{K}\lambda_i = \lambda_i v_i$. With respect to the Darcy model, these eigenvectors are the principal flow directions, and the eigenvalues are the principal flow strengths along their associated eigenvector. The eigendecomposition property of $\boldsymbol{K}$ is further discussed and used in Chapter 5.

Having now introduced the main Darcy parameters, *i.e.* the permeability $\boldsymbol{K}$ and the pressure-coupling array β, it remains to be said that how they relate to the vascular anatomy is not heretofore clear. Furthermore, neither the level of anatomical detail required for such a parameterisation nor the impact of vessel density or RVE size is known. This thesis addresses the issue of how the required parameter fields are to be determined from the network morphology.

2.2 Discrete Vascular Anatomy

As argued in Chapter 1, it would be difficult to overstate the role that discrete vascular anatomy has on tissue perfusion. A significant *stenosis* (or abnormal narrowing of a blood vessel) can cause distal hypoxic or ischaemic tissue regions, severely altering the mechanical, chemical and conductive properties of

the tissue [100]. The solid and fluid components of the tissue are inherently linked via both strain and pressure coupling. Therefore, the discrete vascular structure is a key determinant of the perfusion and functional state of the tissue.

To maximise the use of such discrete data within a mathematical model of perfusion, a *vascular model*, or concise mathematical description of the complex anatomical structure of a physiological network, is required. This model should contain all the necessary topological details for the chosen application. If one was studying turbulent flows in large vessels (*e.g.* wall shear stress simulations in the aorta [73]) then a 3D finite element tessellation of the vessel wall may be required. Yet, such a detailed model is unnecessary for the purposes of whole organ perfusion modelling. Indeed when one is concerned with the flow rate and pressure only, a more concise 1D vascular model which assumes laminar axisymmetric flow is usually sufficient [80, 129]. In this case, the details required are the vessel centreline, connectivity, and radius. In order to store this data in an efficient manner, interpolation functions are used to reduce the data required to represent a given network. Thus a vascular model consists of two data components, the *nodes* and the *segments*. The nodes encode the spatial and radial information for the given interpolation basis, and the segments define the nodal connectivity (see Figure 2.4 for a schematic of a simple vascular model).

2.2.1 Generation of a Synthetic Network

As shall be seen in Chapter 3, the anatomical vascular models that feature in the following chapters of this thesis are constructed from novel image analysis and processing techniques, usually applied to cryomicrotome data stacks [49]. In general, an anatomically-derived vascular model is fitted to some underlying

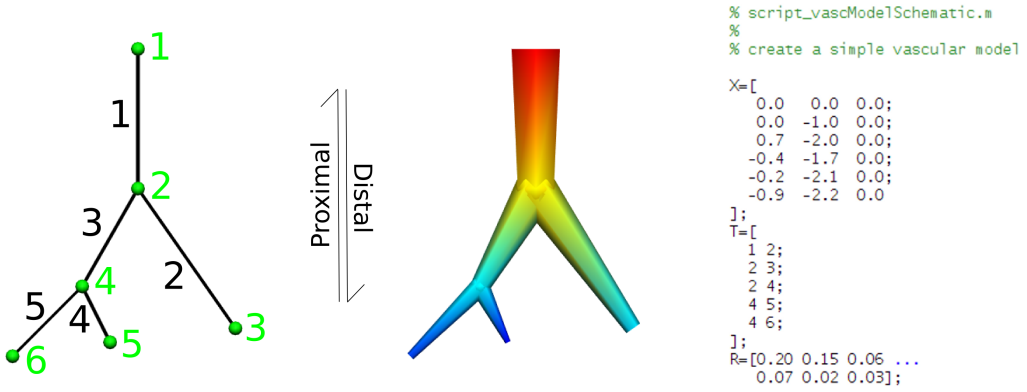


Figure 2.4: Schematic for a simple vascular model, visualised in the xy plane. Nodes are displayed in green while segments are in black. Node 1 is referred to as the 'root node', while in this example nodes 3,5, and 6 are the distal terminal nodes.

data or volume stack. As some experimental artifacts can be difficult to account for in the image processing stage, errors can propagate through to the vascular model *e.g.* tissue deformation prior to freezing, or smearing of the casting polymer during the slicing process (see Chapter 3 for further discussion of these issues). These artifacts can have a non-negligible effect on a flow solution using such a model. Anatomical models also have a complex vessel radius-length relationship, which could introduce a confounding factor that would obscure our basic understanding of the parameterisation techniques featured in this work. Thus, for the purposes of *in silico* testing, a synthetic vascular model was created which is devoid of such complex factors.

This constructed model is used in preference to a more physiological model as: *(i)* it allows for a controlled definition of the 'parent-daughter' vessel radius relation and multi-scale aspects; and *(ii)* it is a fully-connected network within a regular domain for ease of simulation.

A volume-filling bifurcating algorithm was employed to construct the vessel centrelines, similar to that used to model bifurcating lung airways [107]. In

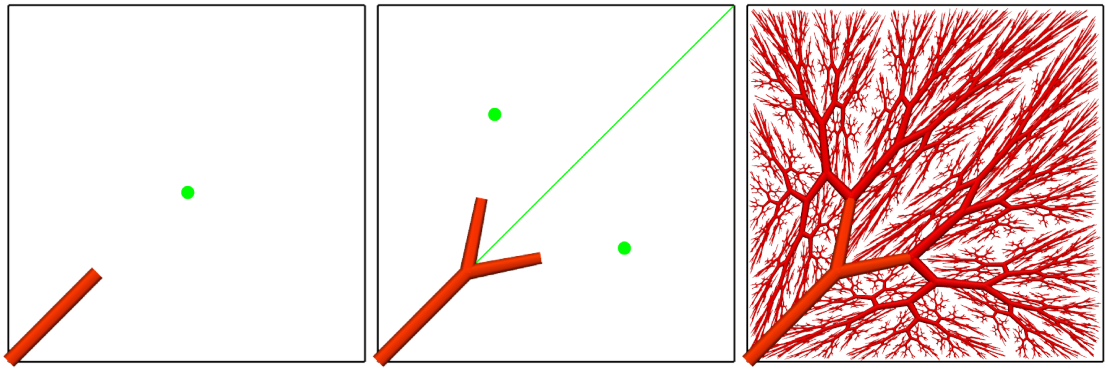


Figure 2.5: Synthetic 2D network construction with $f = 0.5$. (left) Each vessel added is defined to be fraction f along the line joining the vessel start point to the centre of mass, represented by the dot, of the target volume. Here the target volume is the full square. (centre) The previous target area is evenly split into two subregions, each of which becomes a new target area. (right) The algorithm is run for the desired number of iterations, creating a dichotomous network that is distributed across the initial target domain.

brief, given an initial convex volume V_0 and segment start node, $s0$, the first vessel is defined to be a fraction f along the line joining $s0$ and $c0$ where $c0$ is the centre of mass of V_0. The target volume V_0 is next split into two sub-volumes. In 2D this partition is defined by projecting the line $\overline{s0c0}$ onto the boundary of V_0. In 3D, a plane containing this line is required for the partition. The initial plane is defined by the two lines $\overline{s0c0}$ and $\overline{s0s1}$ where $s1 = s0 + (0, 0, 1)$. This plane is then rotated clockwise with respect to $\overline{s0c0}$ until the sub-volumes on either side of the plane are numerically deemed to be of equal volume whereby the subdomain volumes were calculated using Monte Carlo integration [151]. An illustration of the synthetic network generation in two dimensions is provided in Figure 2.5. The following algorithm can then be employed for the desired number of iterations:

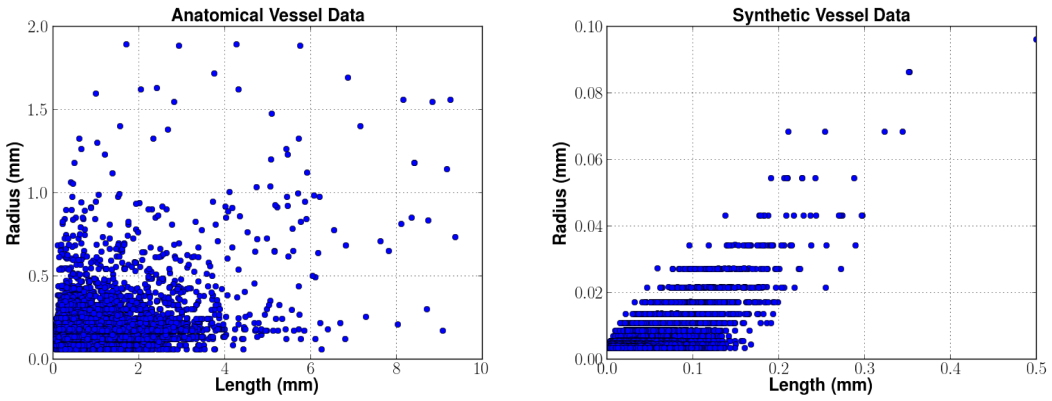


Figure 2.6: Plots of vascular model's vessel radius (average of nodal values) versus the vessel length. (left) Anatomical porcine vessels of length less than 10mm. (right) Synthetic network constructed on the domain $[-1, 1]\text{mm}^3$, hence the smaller range of vessel length. By design, there is a clearer relationship between the two variables for the synthetic network than that of the anatomical model.

Input: Initial convex volume, vessel start point, f value, and n the number of iterations required
Output: Bifurcating volume-filling synthetic network
foreach *i in n* **do**
  foreach *svol in* $svols_i$ **do**
    Obtain $v0$, the vessel start point for *svol* ;
    Construct $\boldsymbol{v}$, the vector from $v0$ to *svol* centre-of-mass ;
    Construct vessel from $v0$ to $v1 = v0 + f\boldsymbol{v}$;
    Partition *svol* into two sub-volumes and add to $svols_{i+1}$;
    Add $v1$ twice to set of vessel start points for iteration i+1;
  end
end

Algorithm 1: The generation pseudocode for a volume-filling bifurcating synthetic network.

With the vessel centrelines having been distributed throughout the target domain, it remains to assign the vessel radii. For this purpose, mass-conserving fluxes were assigned to all vessels by assuming that: *(i)* all terminal vessels have unit flux, and *(ii)* the flux through a parent vessel is equal to the total flux of its daughter vessels. Vessel radii were then assigned based on the flux–radius

relation

$$r = [(q/\alpha_1)^{(1/\alpha_2)}]\alpha_3, \tag{2.2.1}$$

where r is the vessel radius and q is the flux. The following parameter values were used to create the network used in the following sections: $\alpha_1 = 1$, $\alpha_2 = 3$, and $\alpha_3 = 0.001$. Using these parameters, one can see that this relation is similar in form to Murray's Law (see Eq.(7) in [99]). This law was derived from an energy optimisation analysis related to the fact that larger vessels have less resistance, but require more blood volume. Note however, that our generated network by definition only satisfies an equation similar to the form of Murray's Law, but it has not been optimised for energy expenditure in any way. To verify the desired improvement in vascular control and regularity, the synthetic network's topology is compared to an anatomically-derived network's topology in Figure 2.6.

2.2.2 Poiseuille Flow Model

To ascertain the validity of the main hypothesis, one wishes to compare continuum and discrete model flow results. To fulfill this requirement, the assumption is made that vascular flow is governed by Poiseuille's law [85]. Specifically, the Poiseuille vessel flow rate is given by

$$q = \frac{\pi r^4}{8\mu l} \triangle p, \tag{2.2.2}$$

where r is the vessel radius (assumed constant along the vessel, with value equal to the mean of the vessel nodal radii), l is the vessel length, μ is the dynamic viscosity of the fluid, and $\triangle p$ is the difference of the pressure at the

vessel's defining end nodes. Conservation of mass is enforced at each junction via

$$\sum_{i \in I, j \in S} L_{ij} q_j = 0, \tag{2.2.3}$$

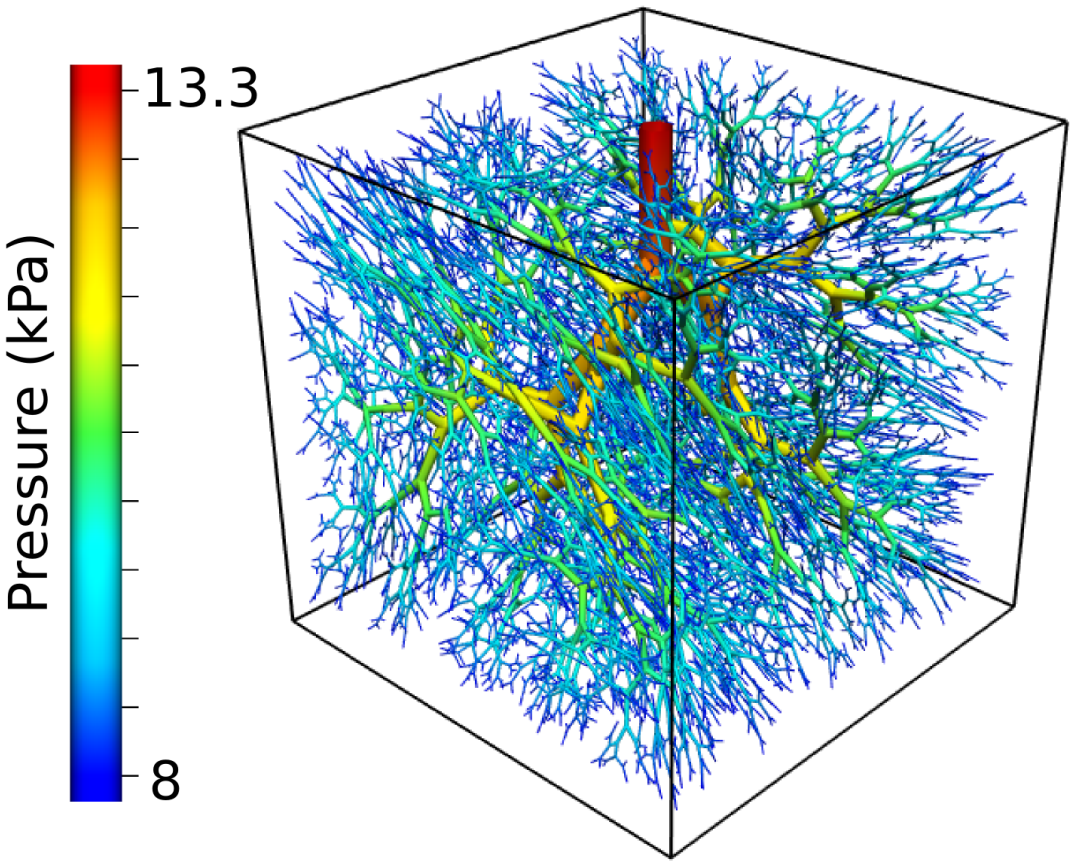


Figure 2.7: Poiseuille pressure solution for the volume-filling synthetic network defined on $\Omega = [-1, 1]^3$mm. Boundary condition pressures of 13.3kPa and 8kPa have been applied at the root node (located at [0,0,1]) and the remaining terminal nodes respectively. The same vasculature is used to parameterise the Darcy model.

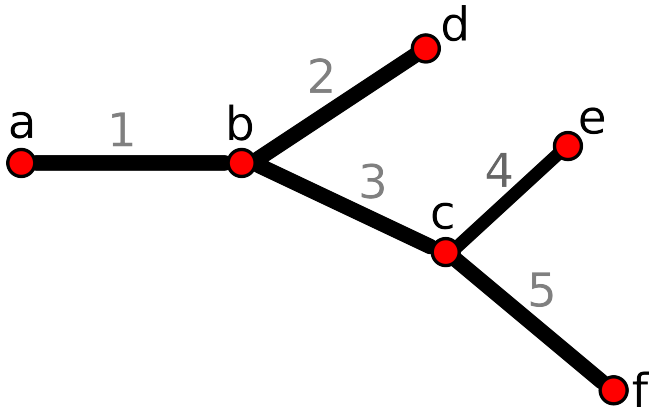
where I is the set of internal nodes, S is the set of vessels, and the matrix $\mathbf{L}$ is defined to be

$$L_{ij} = \begin{cases} +1, & \text{if for node } i, \text{ segment } j \text{ is incoming.} \\ -1, & \text{if for node } i, \text{ segment } j \text{ is outgoing.} \\ 0, & \text{if node } i \text{ is not part of segment } j. \end{cases} \tag{2.2.4}$$

Using this formulation, a constant dynamic viscosity of 0.0035 Pa s, (for more discussion on the value of μ see Section 4.3.1) and Dirichlet pressure BCs of 13.3kPa and 8kPa for the root and distal terminal nodes respectively, the discrete pressure field can be solved for on the entire discrete network (Figure 2.7).

2.2.3 Vascular Partition

The vascular model is partitioned into multiple distinct groups of vessels, that are subsequently used to parameterise the individual porous domains. In general, experimentally derived networks are not sufficiently regular to apply a simple metric such as radius for this partitioning purpose, as distal vessels in a non-idealised network may have a larger or similar radius in comparison to proximal vessels. Hence, there is a need for a more robust partitioning metric that preserves the natural order of the flow *i.e.* proximal vessels should be used to parameterise proximal Darcy compartments. This metric, called the *hierarchic parameter* (ζ) field, is defined such that distal terminal nodes have $\zeta = 0$, the proximal terminal node has $\zeta = 1$, and intermediate vascular nodes have have a ζ value in the range $[0, 1]$. In this work, the definition of ζ is based on the network morphology via a normalised distal vessel length metric *i.e.* ζ at a



Node	HP
a	1
b	$\sum_{i=2}^{5} l_i / \sum_{i=1}^{5} l_i$
c	$\sum_{i=4}^{5} l_i / \sum_{i=1}^{5} l_i$
d	0
e	0
f	0

Figure 2.8: (Left) Schematic of a simple 2D vascular model. Vessels are numbered from $1-5$ and nodes are labeled $a-f$. (Right) Table of hierarchical parameter field, ζ, for the schematic shown on the left, where l_i denotes the length of the i^{th} vessel.

node is the sum of the distal vessel lengths divided by the total network's vessel length (Figure 2.8).

Hence, if one desires N porous compartments then $N-1$ distinct, increasing ζ values are chosen, in addition to $\{0,1\}$, to form an ordered vector Z of dimension $N+1$. Then the i^{th} vascular group is defined to be all vessels with average ζ value $\in [Z_i, Z_{i+1})$. This same group is used to parameterise the permeability tensor field for the Darcy compartment i.

For the following simulations, mean vessel radii of 30μm, 6μm and 3μm were sought for compartments 1, 2, and 3 respectively. This yields a partition defined by the hierarchic parameter array of $Z = [1, 0.019879, 0.000118, 0]$, whereby compartment i vessels are defined by those with average ζ value in the range $[Z_i,\ Z_{i+1})$. The resulting $N = 3$ grouping is displayed in Figure 2.9, and topological statistics are presented in Table 2.1.

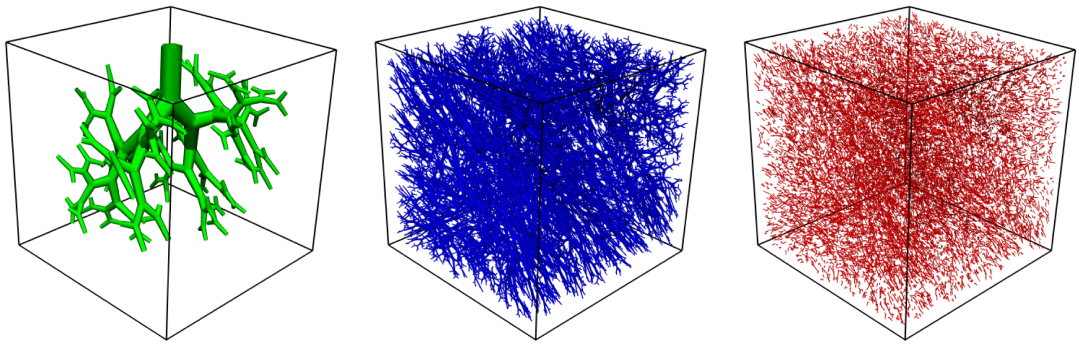


Figure 2.9: A partition of the vascular model shown in Figure 2.7. Mean vessel radii of 30μm, 6μm and 3μm were sought for compartments 1 (left), 2 (centre), and 3 (right) resp. This yields a partition defined by the hierarchic parameter array of $Z = [1, 0.019879, 0.000118, 0]$, whereby compartment i vessels are defined by those with average ζ value in the range $[Z_i,\ Z_{i+1})$.

		Length				Radius			
Cpt #	**# vessels**	**Min.**	**Max.**	**Mean.**	**S.D.**	**Min.**	**Max.**	**Mean**	**S.D.**
1	221	0.0467	0.4999	0.1538	0.0608	0.0215	0.0961	0.0295	0.0120
2	32645	0.0033	0.2547	0.0376	0.0217	0.0041	0.0216	0.0056	0.0022
3	32867	0.0013	0.1608	0.0252	0.0150	0.0034	0.0037	0.0034	1.4e-5

Table 2.1: Compartmental statistics for the synthetic network depicted in Figure 2.9.

2.3 Darcy Model Parameterisation

2.3.1 Spatially-averaged Discrete Fields

Heuristically, the RVE is defined by the minimum volume within which the property of interest remains largely constant [8]. The idea of an RVE is extensively used within the HvC permeability parameterisation method (see Section 2.3.2). However, this method assumes a homogeneous distribution of the property of interest across the RVE, *e.g.* it is assumed that the vascular space is evenly distributed throughout the material (see Eq.(5) of [55]). This assumption

is questionable for a vascular network at the scale of transmural and arteriolar vessels [132], thus the applicability of the HvC method to biological tissue perfusion modelling is one of the issues that this thesis addresses.

One can still hypothesise that the local vessels encode all the necessary information to determine the local permeability tensor, provided of course that this idea is adequately validated via the discrete-continuum model comparisons. Therefore, to parameterise a point $\boldsymbol{x} \in \Omega$ for the Darcy compartment i, only the vessels of the associated vascular group and within the spherical RVE centred at $\boldsymbol{x}$, denoted RVE($\boldsymbol{x}$), are considered.

The same RVE is used to derive a spatially-averaged discrete pressure, $\overline{p}$, for the i^{th} Darcy compartment at $\boldsymbol{x} \in \Omega$ via

$$\overline{p}_i(\boldsymbol{x}) = \frac{\sum_{v \in V_i(\boldsymbol{x})} P_v \; vol_v}{\sum_{v \in V_i(\boldsymbol{x})} vol_v}, \tag{2.3.1}$$

where $V_i(\boldsymbol{x})$ is the set of vessels assigned to Darcy compartment i within RVE($\boldsymbol{x}$), vol_v is the volume of the vessel, and P_v is the average nodal pressure for the v^{th} vessel within $V_i(\boldsymbol{x})$. The discrete pressure is averaged in this manner to provide a comparison with the continuum model pressures, as the discrete pressure is only defined along the vessel cross-sections whereas the Darcy model has a pressure defined over all of Ω. The spatial averages of the other discrete fields of interest are defined in a similar fashion. The porosity of compartment i, denoted ϕ_i, is defined to be

$$\phi_i(\boldsymbol{x}) = \frac{\sum_{v=1}^{V_i(\boldsymbol{x})} vol_v}{vol_{RVE(\boldsymbol{x})}}, \tag{2.3.2}$$

where $vol_{RVE(\boldsymbol{x})}$ is the volume of RVE($\boldsymbol{x}$) within Ω, and thus the porosity of the

material is

$$\phi_f(\boldsymbol{x}) = \sum_{i=1}^{N} \phi_i(\boldsymbol{x}). \tag{2.3.3}$$

Finally, the value of the discrete mass flux from compartment i to k, where $i > k$ without loss of generality, is also required. The set of all vessels within the RVE that belong to compartment k but share a node with a compartment i vessel is denoted by $c_{i,k}$. Then the discrete flux traversing from compartments i to k, denoted $Q_{i,k}$, is spatially-averaged via

$$Q_{i,k}(\boldsymbol{x}) = \sum_{v \in c_{i,k}(\boldsymbol{x})} \frac{\pi r_v^4}{8\mu l_v}(\triangle p_v). \tag{2.3.4}$$

2.3.2 Determination of Permeability

The following three methods for parameterising the Darcy permeability tensor fields are considered:

(i) porosity-scaled isotropic. The vascular beds have frequently been treated as an isotropic porous medium [19, 58, 147, 149], despite the fact that biological networks are rarely isotropic. Vessels with radii in the order of mm are clearly anisotropic as can be ascertained visually from corrosion casts or cryomicrotome images. For example, the large epicardial arteries tend to run along an apex-base direction, and the transmural feeding arteries are radial in orientation. This preferred directionality is functionally related, as their purpose is to rapidly distribute flow over a large volume [133]. Even at the microscale, capillaries with vascular radii in the order of microns are known to lie parallel to the myocytes in organised sheets [82, 84]. Furthermore, the scale of the isotropic

permeability is often taken to be constant across the domain *i.e.*

$$\boldsymbol{K}(\boldsymbol{x}) = k\boldsymbol{I}, \tag{2.3.5}$$

for $k \in \mathbb{R}^+$ and $\boldsymbol{I} \in \mathbb{M}_{3\times3}$ being the 3D identity tensor with assumed units of $\text{mm}^2\ \text{Pa}^{-1}\ \text{s}^{-1}$ (similar to the units assignment seen in Table 1 of [19]), thereby failing to take into account known heterogeneities in vascular scale and density across the heart. Thus, for this permeability parameterisation method, the identity tensor is scaled by the spatially varying porosity field to yield the permeability for compartment i, *i.e.*

$$\boldsymbol{K}_i(\boldsymbol{x}) = \phi_i(\boldsymbol{x})\boldsymbol{I}. \tag{2.3.6}$$

This is arguably the least complex biophysical permeability parameterisation method that provides a spatially-varying $\boldsymbol{K}$ field.

(ii) HvC. In Huyghe and Van Campen [55], the authors derived an expression for a 4D (3D for intra-compartmental flow, and inter-compartmental flow constituting the extra dimension) permeability tensor based on the Slattery-Whitaker spatial-averaging theorem [3, 126, 156]. The formulation was for use in a deforming porous media model and, to the best of our knowledge, it was the first attempt to utilise the detailed geometry of an underlying vascular network to parameterise the permeability tensor field. Notably, this formulation was only applied to a *2D idealised* network. While the work of HvC focused on a 4D Darcy model and the derivation of the permeability field for their framework, for this thesis, one implements the 3D spatial aspect of their 4D perme-

ability tensor given entry-wise by:

$$K_{ij} = \frac{\pi}{128 vol_{RVE} \delta x_0 \mu} \sum_{ns} \frac{d_{ns}^4 \triangle x_{ns,i} \triangle x_{ns,j}}{l_{ns}}, \quad i,j = 1,2,3, \tag{2.3.7}$$

where δx_0 is an infinitesimal element of the hierarchic parameter, ns is the set of vessels within the hierarchic parameter range δx_0, d is the vessel diameter, and l remains the vessel length. $\triangle x_{ns,i}$ is the absolute difference in spatial coordinate i between the vessel end points. Crucially, the averaging theorem employed in their derivation is exact only in the limit of infinite vessel density, and until this work the results obtained for coarse networks using this method have not been shown to yield reasonable approximations *vis-a-vis* continuum and discrete pressure comparisons. On a practical note, a finite number of porous domains, N, must be chosen for simulation purposes, and the approach taken in [55] was to set $\delta x_0 = 1/N$.

(iii) projected-PCA. Firstly, Principal Components Analysis (PCA) is a technique of deducing orthogonal vectors that lie parallel to the vectors of largest data variance. It is generally applied as a dimensional-reduction tool for large data sets, and has been successfully used for determining material parameters within geomechanics studies [40, 63]. For this study, this approach has been specifically tailored for the purpose of permeability derivation from coarsely connected networks. It provides a realistic alternative to the HvC method that can also yield anisotropic permeability fields. In order to determine $\boldsymbol{K}(\boldsymbol{x})$ the vessels within RVE($\boldsymbol{x}$) are first extracted. Each local vessel is translated such that the node closest to $\boldsymbol{x}$ is mapped to the origin, $\boldsymbol{0}$. The vessel is re-scaled such that its length is equal to the value of the vessel's Poiseuille conductance, C. In this fashion, a data set is constructed such that each vessel contributes one datum

that is length C from $\mathbf{0}$, and this vector is oriented parallel to the original vessel direction. The zero-mean step of the PCA method is applied by duplicating each datum via reflection through $\mathbf{0}$. The covariance matrix is then calculated from each dimension of the data set in the standard manner *i.e.* in this scenario, the entry in the (i, j) position is the covariance between the i^{th} and j^{th} coordinate vectors of our data set [61]. The resulting eigenvectors upon eigendecomposition of the covariance matrix are the principal components of the data set. However, the eigenvalues of the covariance matrix are related to the variance of the Poiseuille conductivities, not the conductivities themselves. Thus, to relate the eigenvalues to the conductivities, the vessel orientation vector is projected onto the orthogonal eigenvector basis, the projections are normalised such that the sum of the projected lengths equal the vessel conductance, and then this normalised value is added to each associated eigenvalue of $\boldsymbol{K}(\boldsymbol{x})$.

We note that all of the above methods result in a SPD tensor field as required, and have the correct physical units of $\mathrm{mm}^2\ \mathrm{Pa}^{-1}\ \mathrm{s}^{-1}$.

2.3.3 Determination of Pressure-coupling Coefficients

With regards to the inter-compartmental conductivities *i.e.* the β fields, one can continue with the Poiseuille flow analogy, as outlined in Eq. (2.3.4). If one considers the connectivity between two compartments, i and k say, then one can conclude that, per unit fluid density,

$$\beta_{i,k}(p_i - p_k) = \tilde{q}, \tag{2.3.8}$$

where $\tilde{q}$ is a Darcy volumetric source, and so has units of $\text{mm}^3\ \text{s}^{-1}$. This implies that $\beta_{i,k}$ has units of $\text{mm}^3\ \text{Pa}^{-1}\ \text{s}^{-1}$, and thus it can be recognised as another conductance parameter. If one was to rely on the local vessel data only, it would be an open question as to the appropriate formulation for β *i.e.* determine a form for $\Gamma(r, l)$ which is defined to be the function of proportionality between $\beta_{i,k}$ and the cross-sectional area of the vessels connecting the two Darcy compartments, or equivalently

$$\beta_{i,k}(\boldsymbol{x}) = \sum_{v \in c_{i,k}} \pi r_v^2\, \Gamma(r_v, l_v). \tag{2.3.9}$$

Yet, it is clear that the network pressure is a function of the *entire network morphology*. Thus there may not exist such a function Γ, that depends on the local vessel morphology alone, that can adequately represent the inter-compartment coupling. Hence, one uses the Poiseuille model to aid in the derivation of the β field as the Poiseuille pressure field uses data from the entire network morphology in the construction of the Poiseuille network matrix [109] (Eq. (2.2.3)). From the perspective of the Darcy model, $\beta_{i,k}$ can be viewed as the local constant of proportionality between the fluid flux transfer, and the difference of the Darcy pressures. Or, from the discrete model perspective,

$$\beta_{i,k}(\boldsymbol{x}) = \begin{cases} 0 & \text{if } \overline{p}_i(\boldsymbol{x}) - \overline{p}_k(\boldsymbol{x}) = 0. \\ \frac{Q_{i,k}(\boldsymbol{x})}{|\overline{p}_i(\boldsymbol{x}) - \overline{p}_k(\boldsymbol{x})|}, & \text{otherwise.} \end{cases} \tag{2.3.10}$$

for $i >= k$. This latter restriction is enforced for two reasons: (i) we have already shown that β is symmetric, therefore it would be redundant to separately calculate $\beta_{i,k}$ and $\beta_{k,i}$, and (ii) recall that $Q_{i,k}$ is the *directed* spatially-averaged mass flux between vessel groups associated to compartments i and k (Eq. (2.3.4)),

and by virtue of the definition of $c_{i,k}$, it follows that $Q_{i,k} \neq Q_{k,i}$. Note also that $\beta_{i,k}$ is dependent on spatially-averaged discrete pressures, $\overline{p}$ and not the Darcy pressures p, thus the denominator of β (*i.e.* $|\overline{p}_i - \overline{p}_k|$) does not cancel out with the pressure terms of Eq. (2.1.1)(b) *i.e.* $(p_i - p_k)$. Henceforth, the method of β determination used to produce the results presented in Section 2.4 is given by Eq. (2.3.10).

2.4 Results

All continuum model simulations were solved numerically via the Finite Element Method (FEM), using linear Lagrange pressure basis functions over tetrahedral elements and applying a reduced Darcy formulation [97] (see also Appendix A).

A rms error metric, $\triangle$, is employed to provide a method of comparison between the spatially-averaged discrete pressure, $\overline{p}$, and other relevant fields such as the continuum Darcy pressure. The effect of the chosen boundary conditions used in the discrete/continuum models, in particular the difference between input and output pressures, on this metric should be reduced as much as possible. Thus, when comparing $\overline{p}$ to a spatially varying field f say, $\overline{p}$ is first normalised between 0 and 1. The same normalising transformation is applied to f, and the error between the two fields is defined to be

$$\triangle_f(\overline{p}, f) = \sqrt{\frac{\sum_{m=1}^{n}(\overline{p}(\boldsymbol{x}^m) - f(\boldsymbol{x}^m))^2}{n}}, \tag{2.4.1}$$

where there are n points chosen from Ω at which the two fields are compared, and x_m are the coordinates of the m^{th} point to be compared. There are several

reasons as to why Eq. (2.4.1) is an appropriate measure to compare the continuum and spatially-averaged discrete models: *(i)* root-mean-square error is a cross-discipline, frequently-used, and well-understood measure of the differences between model results, *(ii)* considering the scalar pressure fields rather than the vector velocity fields arguably allows for the definition of a simpler and more transparent error metric, *(iii)* the possible implementation of a velocity comparison is non-trivial due to potential confounding factors such as an RVE with non-zero Poiseuille flow having spatially-averaged zero flow, and *(iv)* given the difference in scale between pressure and velocity fields, it would be difficult to combine measures of both pressure and velocity without introducing a subjective (if not arbitrary) preferential weighting between the two different field types.

In practice, the only fields compared to the averaged discrete pressure are the Darcy pressure (p), and the actual Poiseuille pressure ($\tilde{p}$) which is evaluated at the vascular model nodes. Unless otherwise stated, the fields are compared on a regular grid with a grid-spacing of 0.125mm. This regular grid forms the finite element computational domain, and all parameter fields are evaluated at the mesh nodes.

Dirichlet pressure boundary conditions are imposed on compartments 1 and 3, and are taken to be the averaged pressure values of the same vascular compartments via Eq. (2.3.1). Thus, this testing framework compares the Darcy pressure for compartment 2 against the average discrete pressure of the vascular compartment 2 vessels, and uses the parameterised fields $\beta_{1,2}, \beta_{2,3}$ and $\boldsymbol{K}_2$ (Figure 2.10), thereby reducing the synthetic problem to the smallest number of parameterised fields. Note that $\beta_{1,3}(\boldsymbol{x}) = 0 \ \forall \ \boldsymbol{x} \in \Omega$ as the algorithm for

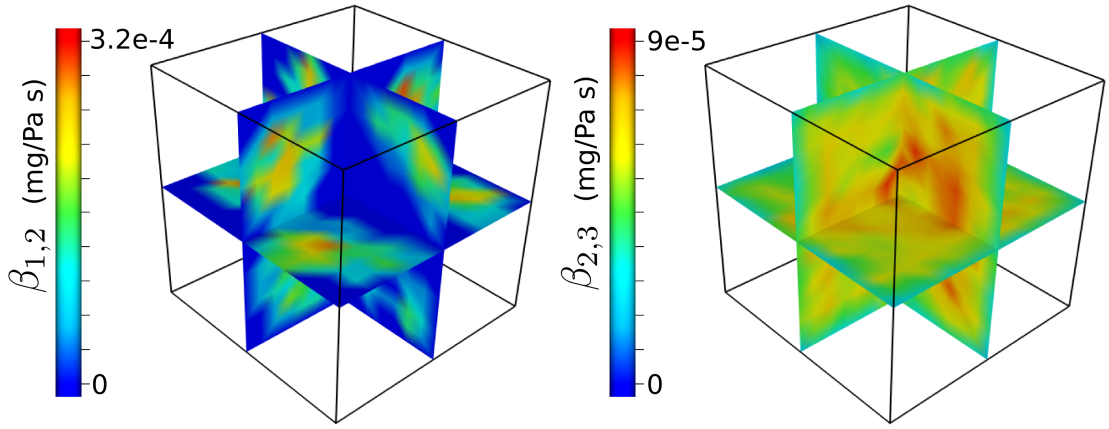


Figure 2.10: Using a three-compartment Darcy model requires three scalar pressure-coupling fields. Non-trivial values for any $\beta_{i,j}$ such that $|i - j| > 1$ allow for coupling between non-neighbouring compartments i and j. By construction of the synthetic network, $\beta_{1,3}$ is zero on Ω. (left) $\beta_{1,2}$ field. (right) $\beta_{2,3}$ field.

constructing the synthetic network ensures that there is no connection between vessels of compartments 1 and 3, due to the regular decrease in distal radius.

Furthermore, none of the three permeability parameterisation methods provide the optimal scaling in terms of reducing the rms error. Thus in the following results sections, all $\boldsymbol{K}$ tensor fields are scaled by the constant that yields the lowest rms error for each individual method. This scaling necessity is linked to the the fact that the challenge of parameterising the porous compartments using discrete data is currently not well-posed. As the problem is over-parameterised, obtaining a satisfactory $\boldsymbol{K}$ field should be possible – however, *uniqueness of solution* is not guaranteed. Of course, a data-driven parameterisation is itself a form of regularisation *e.g.* if one trusts the data-derivation process to accurately capture the principal flow directions at a point, the number of $\boldsymbol{K}$ entries, or Degrees Of Freedom (DOF), decreases. For example, at every parameterisation point, one has six DOF as $\boldsymbol{K}$ is a 3D SPD tensor. If one assumes that the chosen $\boldsymbol{K}$ parameterisation method provides accurate principal flow directions, then the problem has been reduced to 3 DOF *i.e.* the eigenvalues or principal

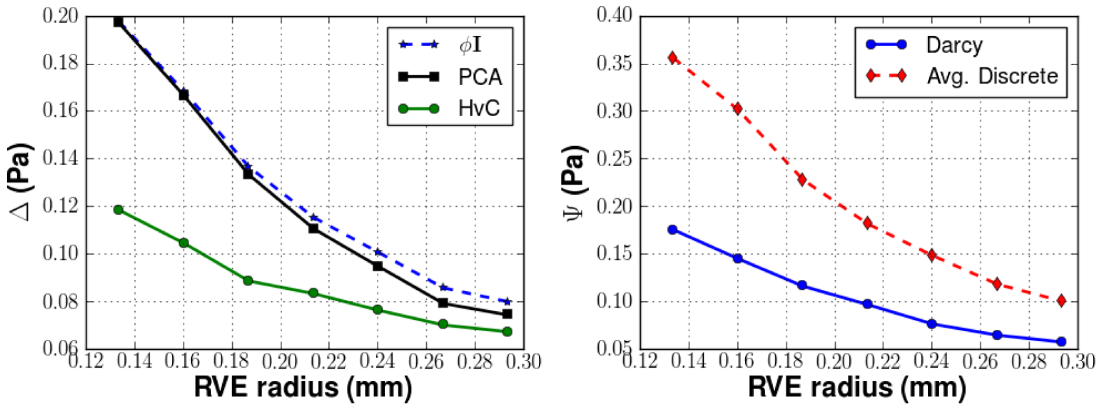


Figure 2.11: (left) Plot of the rms error between the discrete and continuum models for varying RVE radius comparing the three $\boldsymbol{K}$ parameterisation methods tested. Here, $\triangle = \triangle_p$. (right) The reduction in the rms error is seen to be closely correlated with the smoothness of the Darcy and averaged Poiseuille pressure solutions. Our 'unsmoothness' metric, Ψ, is defined via summation of the discrete Laplacian operator, A, applied to the pressure fields evaluated at the mesh nodes of the finite element model of Ω *i.e.* for the Darcy pressure we have $\Psi = \sum_{i=1}^{m} \sum_{j=1}^{m} A_{ij} \overline{p}_j$, $A \in \mathbb{M}_{m \times m}$.

flow strengths. Again, if one then assumes that the chosen $\boldsymbol{K}$ parameterisation method provides an accurate *relative* principal flow strengths, then the problem has been reduced to a single DOF *i.e.* the scale of the permeability.

2.4.1 RVE Radius

RVE size is an important parameter with respect to $\triangle_p$, and a suitable size is dependent on the particular material application. For this application, it is dependent on the vascular scale and density of the Darcy compartment being parameterised, however a suitable RVE radius is not obvious *a priori*. The RVE size should ensure a desired level of smoothness in the averaged field, but it should also capture the feature(s) of interest. An unsuitable RVE size can produce various undesired artifacts *e.g.* constant porosity across Ω, or the creation of unphysiological flow paths. A lower bound for the RVE size can be set by insisting that every point in Ω lies within at least one RVE.

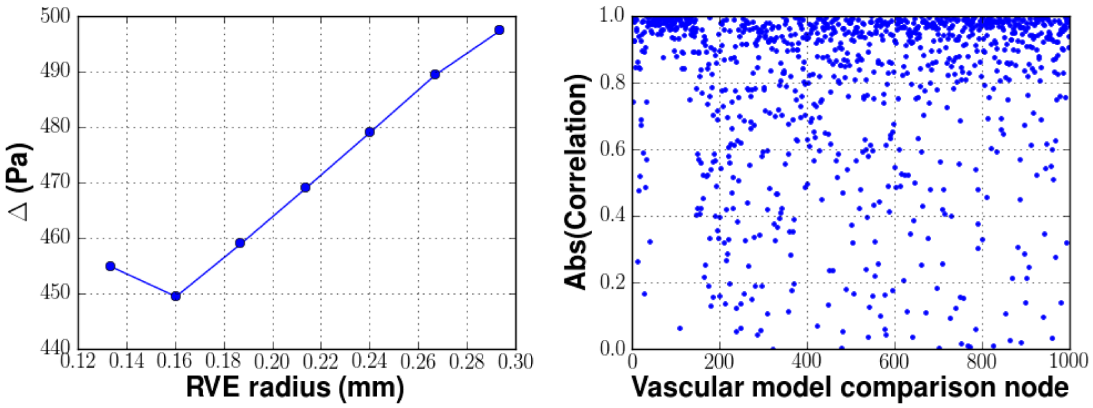


Figure 2.12: (Left) Error measures demonstrating the difference between the actual nodal pressure of the discrete flow model ,$\tilde{p}$, versus the spatially-averaged pressure for a changing RVE radius, *i.e.* here $\triangle = \triangle_{\tilde{p}}$. The error was calculated using a random selection of 1000 vascular nodes from vascular compartment 2, and the $\overline{p}$ values evaluated at the same spatial coordinates. The linearity of the left-most plot is due the high correlation of the individual nodal points with respect to the RVE size. (Right) The absolute value of correlation between the pressure from selected vascular nodal points and the RVE radius is shown.

To investigate the effect of RVE radius on the continuum pressure solution, $\triangle_p$ is evaluated for parameterisations defined using various RVE radii values. It is observed that the error decreases with increasing radius, and that this result is closely correlated to the increased smoothness in the average discrete solution (Figure 2.11). This allows the continuum solution, which is guaranteed to be smooth due to its use of interpolating functions, to better approximate the $\overline{p}$ field. Obviously, as the averaged pressure field becomes smoother with increasing RVE radius, the difference between the average discrete pressure field and the actual discrete pressure field existing on the vascular model increases. Figure 2.12 demonstrates this, and a clear linear trend is observed between $\triangle_{\tilde{p}}$ and the RVE radius which is explained by the high correlation between the individual average discrete pressure values at the comparison points and the RVE radius used. Thus, in choosing a RVE radius for a given vascular compartment, a suitable balance must be sought between increasing the smoothness of $\overline{p}$ and

the divergence of $\overline{p}$ from the Poiseuille pressure $\tilde{p}$. Based on this knowledge, an RVE radius of 0.2667mm was chosen for the remaining synthetic network simulations. Furthermore, Figure 2.11 not only shows that the HvC method performs better than the other two methods with respect to the quantitative rms error metric, but also produces a qualitative match to the spatially averaged discrete pressure, as seen in Figure 2.13.

2.4.2 K Parameterisation and Vessel Density

The sensitivity of the $\boldsymbol{K}$ parameterisation methods with respect to vessel density is now examined via comparison of their $\triangle_p$ values, as defined in Eq. (2.4.1). Not only should the optimum method have the lowest error, but it should also be robust against varying vascular partitions. Here, vessel density was varied by uniformly increasing the ζ range of compartment 2. Thus, Figure 2.14(a) compares the errors over a varying vessel density range for the second Darcy compartment. It can be seen that the HvC method outperforms the other $\boldsymbol{K}$ parameterisation methods for all vessel densities tested. Of significant interest is the fact that the porosity-scaled isotropic method performs as well as the projected-PCA method, despite using less vascular model detail and being a more simplistic method in general. This finding is discussed further in Section 2.5.

2.4.3 Independence from Poiseuille Pressure BCs

It remains to be shown that the HvC $\boldsymbol{K}$ and β parameterisation methods are robust against changes in the Poiseuille model BCs. The inter-compartment

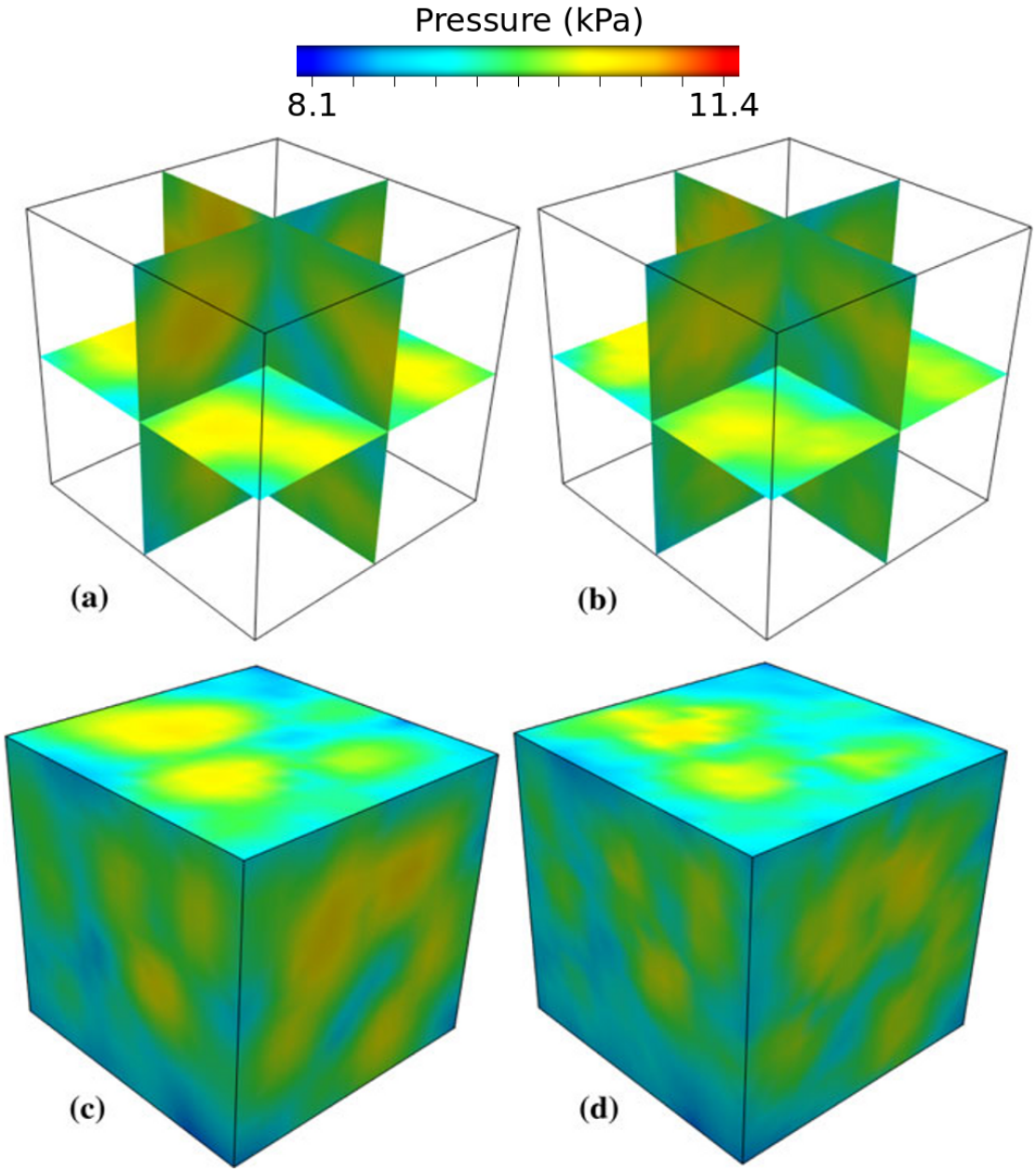


Figure 2.13: Darcy pressure results using the Huyghe and Van Campen method for determining K_2. Figures (a) and (c) show the Darcy pressure field for internal isosurfaces and the external surface of Ω resp. Similarly, figures (b) and (d) show the average discrete pressure field resulting from the Poiseuille model, also on the internal isosurfaces and the external surface of Ω resp.

connectivity array β has been defined specifically with this need in mind, hence it uses local flux *per unit pressure difference*. As such, it should not require re-

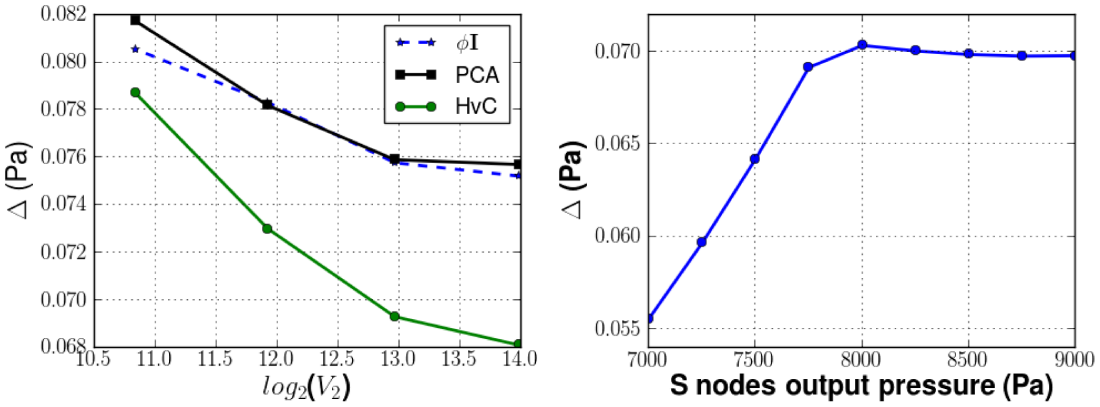


Figure 2.14: $\triangle = \triangle_p$ for both sub-figures. (Left) Plot of the rms error between the discrete and continuum models for the three $\boldsymbol{K}$ parameterisation methods as the vessel density is varied. The axis displays the logarithm to the base 2 of the number of vessels in vascular compartment 2. There are three main points to note: *(i)* All three methods display decreasing rms error with increasing vessel density. *(ii)* The porosity-scaled isotropic method performed as well as the projected-PCA method. This suggests that the synthetic network is inherently isotropic due to its volume-filling nature. *(iii)* The HvC method consistently yields a significantly lower error than either of the other two methods. (Right) Terminal nodes in the subdomain $[0,1]^3$mm were subjected to varying Dirichlet pressure BCs. The parameterisation of the Darcy model was done using a homogeneous output pressure of 8kPa. Subsequently, only the Darcy Dirichlet pressure BCs are varied amongst the simulations. The decreasing rms error for output pressures less than 8kPa is due to the normalisation step within the rms error estimation.

parameterisation when a change in a pressure BC occurs, which would clearly be an untenable scenario for a dynamic large-scale perfusion model.

In order to demonstrate this independence, the pressure BCs at terminal nodes in the subdomain $[0,1]^3$mm of Ω (denoted S) were varied, while the remaining terminal nodes were kept at 8kPa. The Darcy parameter fields were derived with all terminal nodes at 8kPa. The pressure at the subdomain nodes were then varied over the range $7-9$kPa. Thus, the only change to the Darcy model was the Dirichlet pressure BCs applied on Darcy compartments 1 and 3, which were still taken to be the averaged pressure values of the same vascular compartments via Eq. (2.3.1) as before.

Two trends are visible in Figure 2.14(b). Firstly, and most importantly, there

is no increase in the rms error across the boundary pressure range tested, in particular for $8 - 9$ kPa. This demonstrates the independence of the parameterisation from the discrete boundary conditions used to define the β array. Secondly, the decrease in rms error for boundary pressures less than 8kPa is explained by the normalisation step in calculating the rms error. As the averaged discrete pressures are spread over a relatively wider range for these boundary pressure values, the normalisation step decreases the variance of the pressure discrepancies, thereby yielding a rms error that decreases in conjunction with the linearly decreasing discrete pressure boundary condition.

2.4.4 Compartmental Mass Transfer

One wishes to briefly consider the general difference in flux between the two models, even though it does not feature in the optimisation cost function. To compare the two model results, the net flux traversing xy-planes were calculated. Mass transfer moving in a negative z-direction was deemed to be positive, as this is general trend of transfer given the root node position of the vascular network. The results are shown in Figure 2.15, whereby unit fluid density has been assumed. Note that there are two mass transfer 'spikes' for the continuum model compartment 1 results, which are due to minor numerical integration factors. Specifically, while mass is conserved on a total volume basis, the mass flux crossing the specified z-plane surface involves the evaluation of the z velocity field at the points of intersection of the tetrahedron and the particular z-plane.

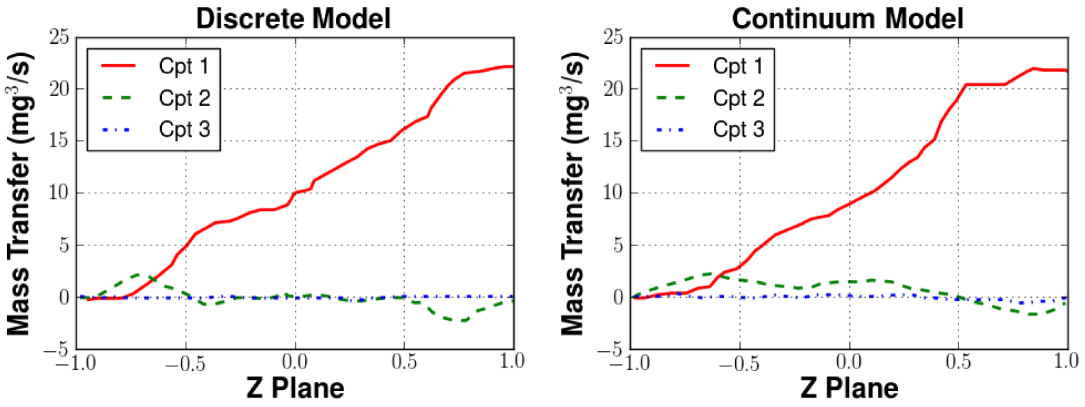


Figure 2.15: Mass transfer across z-plane isosurfaces were calculated for both the discrete (Left) and continuum models (Right).

2.5 Discussion

In this chapter, 3D Darcy porous domains have been successfully parameterised using 1D vascular data and a combination of new and previously existing homogenisation methods. The quantitative and qualitative results of Figure 2.11 and Figure 2.13 justify the original hypothesis *i.e.* that a satisfactory Darcy pressure, with respect to a discrete pressure model, can be obtained via spatial homogenisation of 3D vascular networks. The HvC method was shown to be the optimum tested method across the range of the simulation study, which included varying vessel density and sampling domain size. This is most likely due to its rigorous mathematical foundation, but importantly, it was also better for relatively coarse vascular networks where the assumptions underlying the HvC method are questionable, particularly the homogeneous distribution of the averaged fields within the RVE. Clearly the vascular densities simulated were thus still within a range where the HvC method is applicable.

We verified that the porosity-scaled isotropic permeability parameterisation method produced larger rms errors, in comparison to methods that used direc-

tional vessel data, when anisotropy was known to be present in the network. However, it is worth noting that this error converges towards the HvC error with increasing RVE size (Figure 2.11), yielding a 22% increase in the porosity-scaled isotropic error over the HvC error at the preferred RVE radius of 0.2667 mm. This could allow for the use of the less complex porosity-scaled isotropic method for parameterising models where detailed vascular data is not available. In the near future it may even be possible to determine *in vivo* total macroscale porosity measures of tissue, using a combination of high resolution MRI and intravascular contrast agents.

Furthermore, a significant proportion of the rms error to vessel density relationship for the synthetic network has been characterised. The derivation of the inter-compartment coupling fields β has also been shown to be robust in relation to discrete pressure BCs. This is a critical finding with respect to the future application of the Darcy parameterisation to dynamic perfusion models.

In common with many spatial averaging techniques however, a limitation of the parameterisation process is the choice of RVE size. In Section 2.4, Figure 2.11 shows a decrease in rms error with increasing smoothness of the averaged discrete pressure. Concomitantly, Figure 2.12 reveals the divergence of the averaged discrete pressure from the true Poiseuille solution. We suggest that the RVE size should be chosen based on analysis of these two relationships to yield an RVE based upon a desired error and faithfulness to the discrete pressure over the network. The RVE should also be of a sensible size with respect to any available validational data *e.g.* the RVE radius should be smaller than the in-plane resolution of the perfusion imaging data, as otherwise the model is averaged over a larger volume than the data we wish to compare to.

RVE size is also sensitive to the hierarchic parameter, ζ, and hence the vascular partition. The ζ field relies on the quality and type of the vascular model. A poorly segmented network with missing subtrees would yield vessels with unusually small ζ value compared to vessel radius. Of course these could be easily detected via statistical tests on the network. If vascular loops are present in the arterial network model then ζ could be defined using a discrete pressure solution [149] (Section 4.1.1).

We believe that the 3D Darcy model plus volumetric sources scaled by pressure difference for inter-compartment connectivity is more representative of the perfusion process in tissues than the pioneering 4D Darcy model of Vankan *et al.* as we use global network data in the definition of the inter-compartment coupling field β (see Eq. (2.3.10)). While Vankan *et al.* do use a discrete pressure field in the definition of one of their hierarchic parameter fields, this merely determines which vessels belong to each compartment, and is not used in the determination of the parameter values themselves.

The porosity-scaled permeability parameterisation method performed well in comparison to the more data-reliant projected-PCA method. One possible cause of this finding is that the volume-filling network has an intrinsic level of isotropy, thus aiding the former method. This hypothesis is tested in Chapter 4 whereby the three $\boldsymbol{K}$ parameterisation methods of this chapter are applied to a capillary network derived from confocal microscopy images.

Summary

Several permeability and pressure-coupling parameterisation methods based on discrete vessel data were investigated. The optimum method tested was established, and the role of RVE size and vascular density has been further elucidated. However, this *in silico* validation on a static domain using a *synthetic* network does not necessarily translate to more realistic networks. The following chapter describes how such an anatomical network can be extracted from experimental data, and is manipulated into a form suitable for data-driven parameterisation of perfusion models.

3 Arterial Model Creation and Analysis

As demonstrated in the previous chapter, the creation and use of idealised and/or synthetic vascular models has proven to be extremely beneficial to the field of biomedical engineering. For example, an idealised periodic network was used to model drug delivery to tumour growths [20], and CCO generated networks have been applied in investigating transient coronary blood flow [129] and for testing spatial-averaging techniques within model parameterisation problems [59, 148][Chapter 2 of this thesis]. In the majority of these cases, including the work of Chapter 2, their creation and use was justified by the lack of experimental anatomical data at the time.

However, such artificially constructed networks can lack physiological realism in general, but in particular on local scales *i.e.* the statistics derived from the entire network may match histological data in a global sense, but the local structure is not representative of the physiological network. This lack of realism, and use of generic data is at odds with the current era of patient-specific modelling – which is to the forefront of modern clinical research efforts, driving the desire for improved biophysical parameterisation and modelling. Furthermore, it can be difficult to derive physiologically valuable information from synthetic

networks

As discussed in Chapter 1, the desire for increased anatomical data has led to the development and implementation of several direct imaging methods. However, these modalities cannot resolve the vasculature at fine scales and across the larger organs, with the exception of the cryomicrotome. This imaging modality is the most advanced and recent development in whole-organ high-resolution direct visualisation of vascular networks. This chapter will focus on how cryomicrotome data can be used to create anatomically-derived vascular and myocardial models.

Thus, in Section 3.1 the cryomicrotome experimental protocol and subsequent vascular model creation and LV tissue model creation for a general animal study are outlined. The whole-organ vascular model is then manipulated into a suitable form for continuum perfusion modelling, as described in Section 3.2. The resulting arterial network statistics are presented in Section 3.2.1, allowing for a partial assessment of the quality of the extracted networks. Finally, an in-depth analysis of the advantages and disadvantages of cryomicrotome-derived vascular models are discussed in Section 3.4.

3.1 Cryomicrotome Imaging

Given that there is presently no *in vivo* method to image vessels at the required scale and resolution, it is a necessity that the animal is sacrificed in a controlled manner, and its heart excised. To minimise any stress caused to the animal, and follow the current best-practice: *(i)* experimental procedures were undertaken in strict accordance with the Institutional Animal Care and Use Commit-

tee (IACUC) of the University of Amsterdam, and *(ii)* cryomicrotome imaging data was acquired according to standard procedures developed at the Department of Biomedical Engineering and Physics, Academic Medical Center, University of Amsterdam. While the full details can be found in the original literature for the experimental study [54, 143], for reasons of conciseness the process is now only briefly elucidated. The excised heart was perfused with adenosine-loaded ($100\mu g/L$) phosphate-buffered saline, followed by the fluorescent vascular casting agent (Batson #17 casting resin (Polysciences Europe, Eppelheim, Germany)) at a pressure of 90mmHg. After the cast has solidified, the heart was suspended in 5% carboxymethylcellulose solution (Alfa Aesar, Karlsruhe, Germany) and frozen at -20° Celsius. The heart was then transferred to the cryomicrotome and serially sliced (slice thickness is typically 50μm, and can be adjusted by the operator) and imaged using fluorescent optical surface imaging in a repetitive fashion until the entire organ had been processed. On a practical note, the CDC camera used in the cryomicrotome captures an image with pixel dimensions of $4096x4096$. With approximately $4,000$ images per data stack, this implies that 8 bit greyscale images (1 byte per pixel) will generate a data-stack size of greater than 64GB, which constitutes a significant challenge to subsequent data-processing techniques.

3.1.1 Vascular Model Creation

Once acquired, the resulting data stack was enhanced using our previously reported procedure [49]. Specifically, a multi-scale vesselness filter [45] was applied to the data stack, which was then binarised using a combination of Sauvola local adaptive and Otsu global thresholding [106, 121], thereby remov-

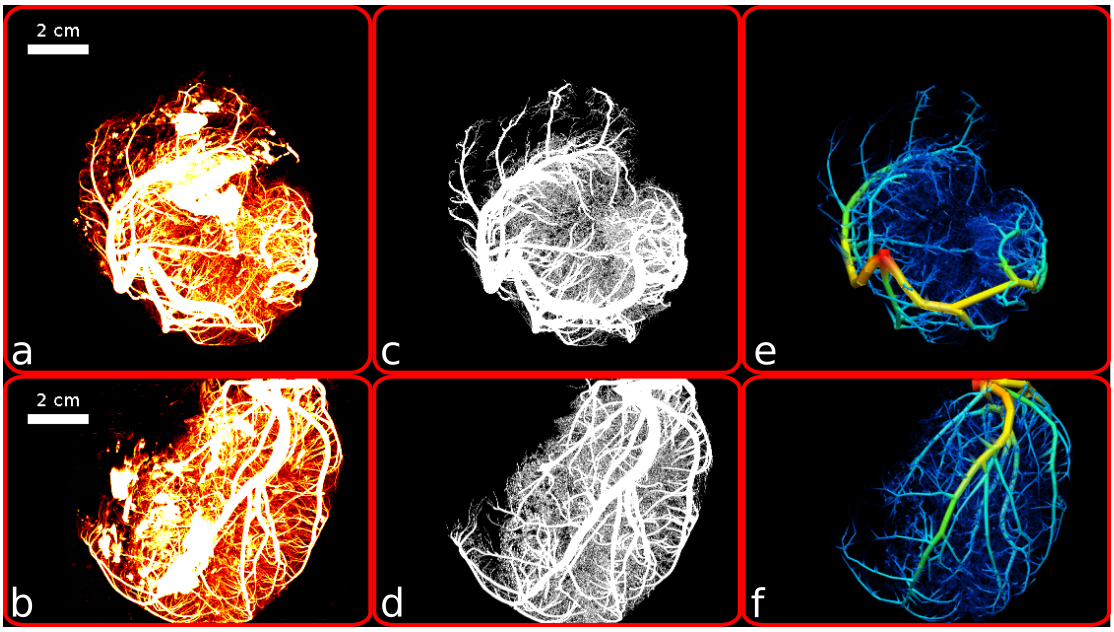


Figure 3.1: Projections (top row short-axis, bottom row long-axis) from the same porcine vascular model creation process. (a-b) Maximum intensity projections of the original cryomicrotome imaging data stack. Note the varying intensity and globular structures where leakage of the casting agent occurred. (c-d) Projections of the enhanced and binarised vascular tree, post-vesselness filtering. (e-f) After skeletonisation and radius estimation, a coronary arterial network is created. The radius field is displayed on a linear colour scale from $0 - 1.8$mm (blue-red), with an alpha channel applied to all radii < 0.2mm to enable the visualisation of the larger arteries.

ing non-vessel structures. Connected component analysis was conducted to extract the fully-connected vascular network. This structure was skeletonised via distance-ordered homotopic thinning [116] and subsequently pruned in a semi-automatic manner to remove any spurious branches. The vessel radii were evaluated at the skeleton voxels using a model-based radius estimation technique [49]. As this technique assumes a circular cylindrical vessel, cylindrical vessel segments were fitted to this data to provide a mathematical model of the anatomical vasculature in a consistent manner (see Figure 3.1 for a schematic of this process and Figure 3.5 for an image of the full porcine arterial tree).

3.1.2 Myocardial Tissue Model Creation

A corresponding finite element LV myocardial mesh was required for the purposes of the Darcy perfusion model, as applied in Chapter 4. To this end, the white-light imaged data stack was downsampled to approximately 40 image slices. A binary mask of the tissue domain was then manually segmented from this data stack (Figure 3.2(a)). A cubic Hermite finite element mesh was automatically fitted to the mask (Figure 3.2(b))[77]. Finally, a tetrahedral mesh of our desired resolution was constructed from the exterior surfaces of the cubic Hermite mesh using the open-source tetrahedral meshing software, *NetGen* [1] (Figure 3.2(c)).

Two data sets were processed in this manner, with an isotropic voxel resolution of 64μm and 50μm, yielding a porcine and a canine model respectively. These vascular models are said to be representative of the coronary diastolic state (see Section 5.4 for more discussion on this point).

3.2 Vascular Model Reduction

The extracted vascular model in its full form is unsuitable for our continuum perfusion modelling needs. This is because there exist distal terminal nodes that reside outside the LV tissue model, *e.g.* in the atria, the RV, and the papillary muscles. Furthermore, with respect to the discrete flow model, each one of these terminal nodes nodes would require a prescribed pressure or velocity BC to be applied, the values of which are unknown. It was deemed infeasible to extend the LV tissue model as: *(i)* an extended LV model would result in

[1] http://www.hpfem.jku.at/netgen/

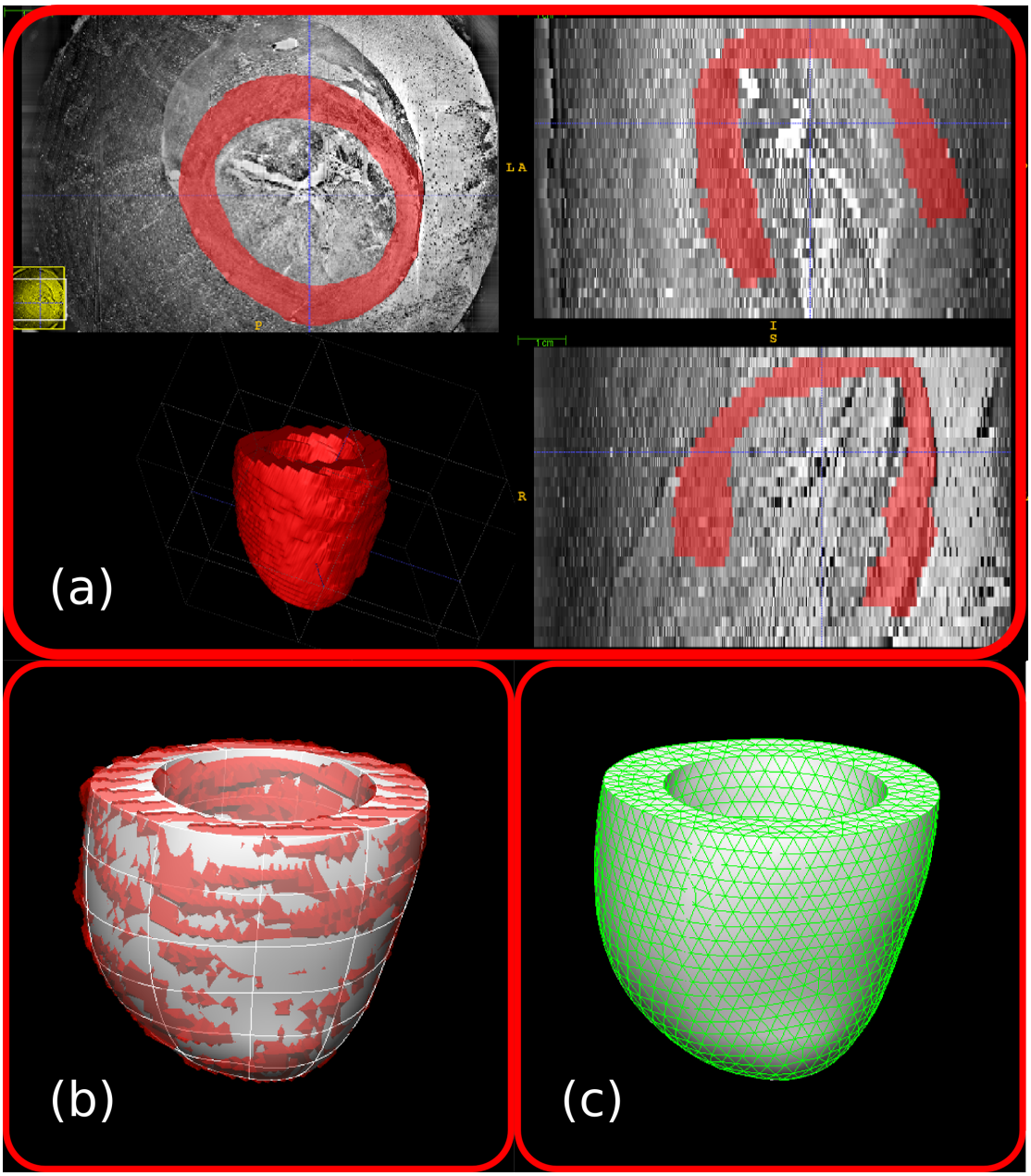


Figure 3.2: LV myocardial tissue model generation. (a) The cryomicrotome white light data stack is uniformly downsampled to yield approximately 40 slices, from which the LV tissue voxels are manually segmented. (b) A cubic Hermite mesh is automatically fitted to this binary mask using bespoke software [77]. (c) The tetrahedral meshing software, *NetGen*, was used to create a mesh of the desired finite element resolution from the exterior surfaces of the cubic Hermite mesh.

severe LV endocardial tissue invaginations that would create serious difficulties for a future hyperporoelastic perfusion model due to the likelihood of high

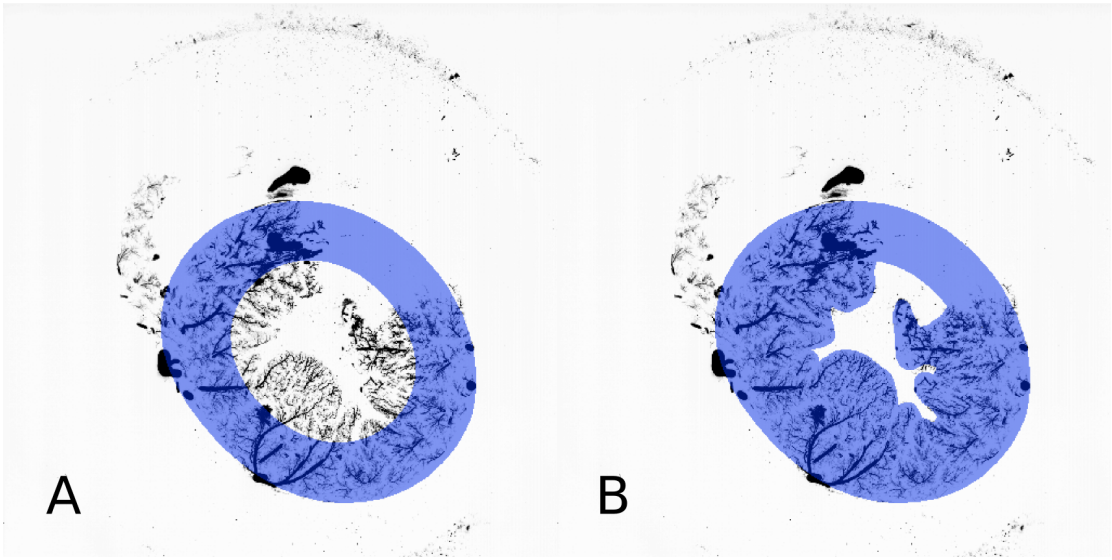


Figure 3.3: (A) A short-axis slice of the LV tissue model as used in the forthcoming perfusion simulations. (B) A representation of the same slice if all LV vessels were to be encapsulated with the tissue model. The severe tissue invaginations would present a significant challenge to a deforming perfusion model.

stress development at tissue cusps, as these points are associated with the shortest distances to the epicardium and circumferential expansion during diastole. Furthermore, the requirement for a constrained solution solver able to the handle what would become a contact mechanics problem (see Figure 3.3); *(ii)* an extended LV model would require the spatial-averaging of the sparse atrial vessels to parameterise this region, which was shown in the vessel density study of Section 2.4.2 to cause a decrease in solution accuracy. Thus, in order to reduce possible ambiguities with respect to these unknown vascular model BCs, and to retain a tissue model applicable in the hyperporoelastic framework, it was decided to reduce the whole-organ vascular model to the vessels involved in perfusing the LV tissue model only.

This vascular model reduction was done by constructing the Path of Least Resistance (PLR) from each terminal node to the root node, *i.e.* the most proximal node. Dijkstra's algorithm was employed for this purpose, using the calculated

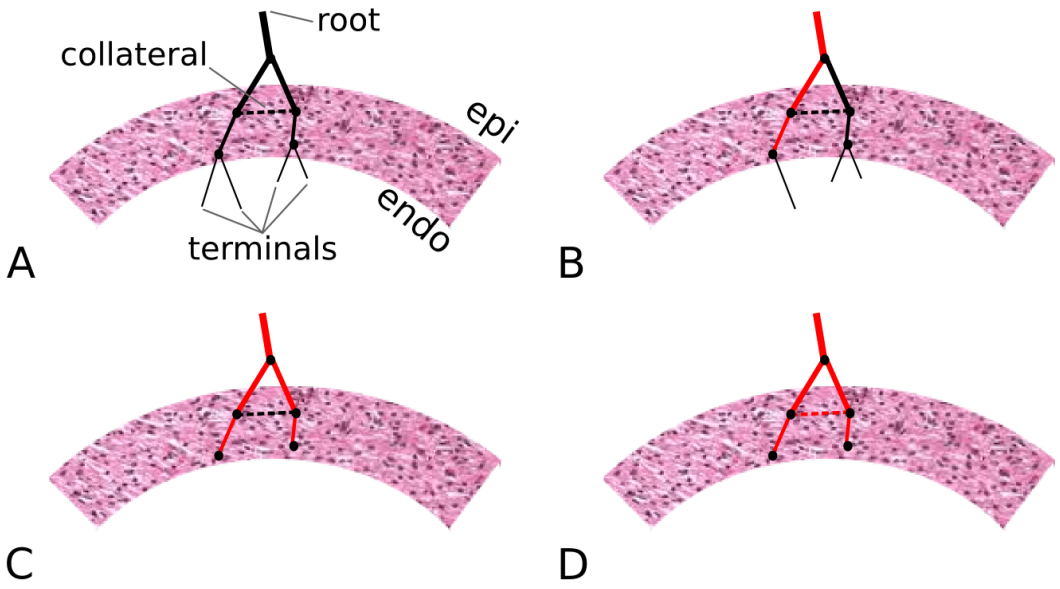


Figure 3.4: Schematic in two dimensions of the vascular model reduction process. (A) A simple network is shown that has vessels terminating outside of the tissue model. (B) The vascular model reduction process is applied to the first such vessel. The Path of Least Resistance to the root node is calculated, and the largest continuous section that terminates within the tissue model is kept (red vessels). The terminal vessel is removed. (C) The process is applied to all terminal vessels that reside outside of the tissue model. (D) Finally, any remaining vessels that lie fully within the tissue model but that have not formed part of a PLR are added to the reduced model tree. This ensures that all collaterals are kept.

value of Poiseuille resistance as the cost function for each vessel[31]. The portion of each such PLR consisting of the first vessel internal to the tissue model encountered from the terminal node through to the root node was added to the total reduced vascular model. To avoid erroneously removing collateral vessels lying between any two PLRs, a final post-processing step added any vessels that lay completely within the LV tissue model (Figure 3.4). This reduced model is henceforth denoted as the Left Ventricular Model (LVM).

The vessels removed in this process are not local to the tissue model, and as such do not affect the Darcy permeability fields calculated in Chapter 4 even if they are not removed. Note that the porcine model does not have a Right Coro-

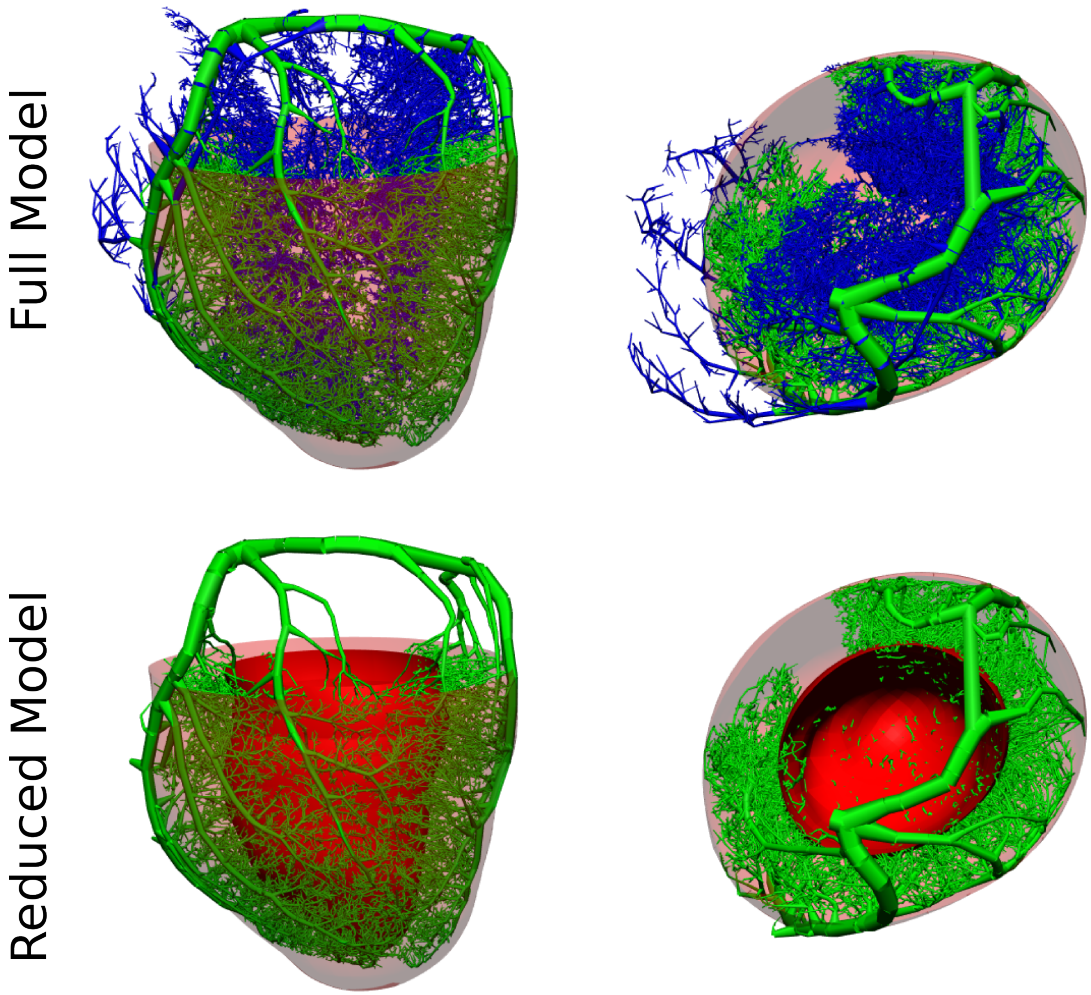


Figure 3.5: To simulate the perfusion state of the LV tissue model, all vessels that are not involved in this process are removed, for instance, vessels suppling the RV, atria, or papillary muscles. The LV endocardial surface is visible in red for the reduced vascular model images. (top row) Long and short axis views of the full vascular model. The removed vessels are shown in blue. (bottom row) Long and short axis views of the reduced vascular model only.

nary Artery (RCA) due to difficulties encountered during the casting process. Thus, to effectively remove this portion of the computational domain from the simulation, zero pressure was assigned to finite element mesh nodes in this region. This reduction process yielded arterial networks with 42,752 and 27,416 vessels for the canine and porcine LVM, respectively (Figure 3.5). Of the vessels

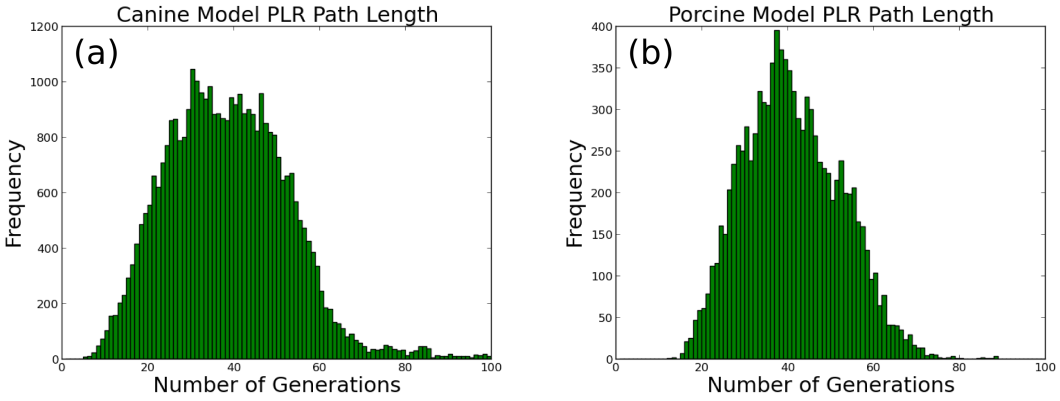


Figure 3.6: Distribution of the PLR path length from each terminal node to the root node for the canine model (a) and the porcine model (b). The mean of these distributions is often used as a surrogate for the 'size' of the network.

removed from the canine (porcine) model, 26% (29%) were atrial vessels, the remainder being papillary muscle vessels.

3.2.1 Reduced Arterial Model Statistics

The number of vessel generations, or the number of vessels in series, is often reported as a measure of the 'size' of a vascular model. To quantify this metric, the number of vessels along the PLR from each terminal node to the root node is calculated. As the reduced vascular models in question are anatomically-derived, and not constructed models, there is a significant variance in these path lengths. Figure 3.6 shows the distribution of the path lengths for the canine and porcine LVMs, and the number of generations are 38 ± 14 and 41 ± 11 respectively (mean$\pm$Standard Deviation (SD)).

One next considers the vascular morphological distributions for the canine and porcine LVMs, as presented in Figure 3.7. Note that the PDFs of the canine and porcine vessel lengths are log-normal distributed (see left-hand column of Figure 3.7), which was previously shown to be the case for the rat microcircu-

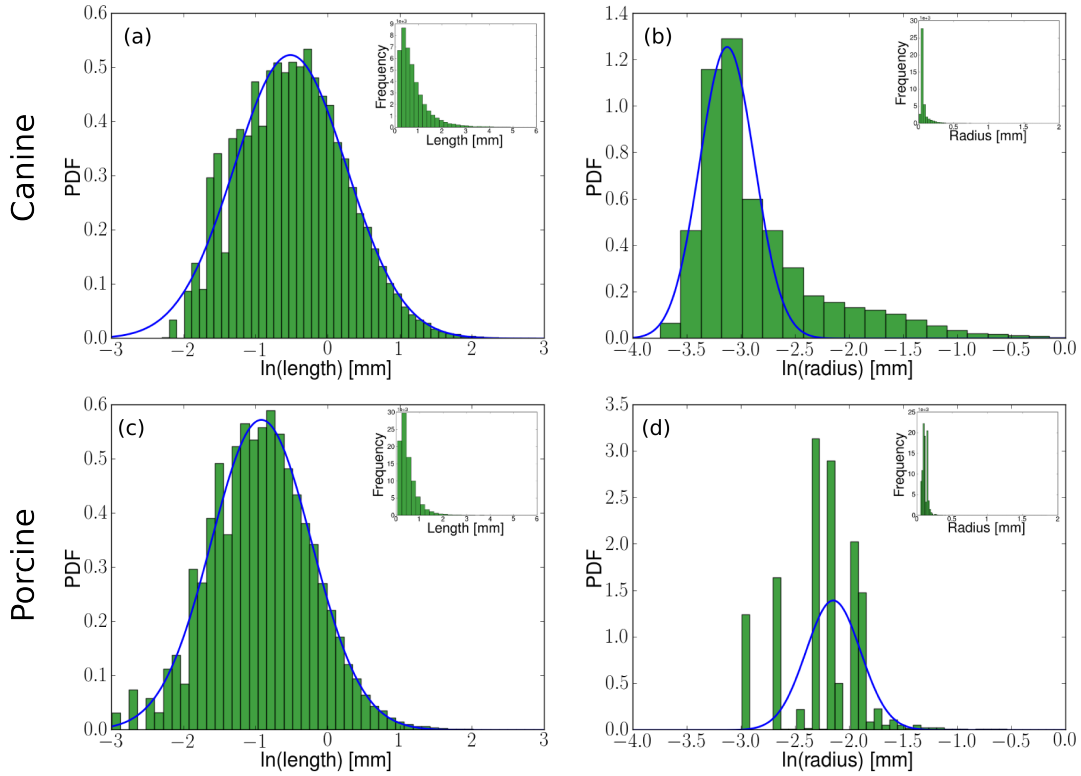


Figure 3.7: Network statistics for the canine model (top row) and the porcine model (bottom row). The left-(right-) hand column shows the distribution of the logarithm of the vessel lengths(radii). These distributions have been fitted with log-normal PDFs (blue lines).

lation [79]. The log-normal fit does not hold for the vessel radii however (see right-hand column of Figure 3.7). This is particularly true for the porcine vessel radii distribution, the histogram of which is remarkably discontinuous. This result is unlikely to be caused by inter-species variation alone. Rather, it may reflect the influence of the microsphere deposition study which was conducted in the same heart just prior to the injection of the casting agent in the case of the porcine experiment, whereas no microspheres were injected for the canine experiment. The possible effects of microsphere deposition on network extraction are discussed further in Section 3.4. Prior to the discussion, and due to the concerns raised with regards to the porcine radii distribution, it is appropriate

to first examine the extracted netwroks with regards to known physiological features.

3.3 Model Comparison to Experimental Data

As previously mentioned, it is extremely difficult to get pressure and/or flow data on the scale of the microvasculature (see Chapter 1). However, it is possible in some limited circumstances to obtain such data from epi- and sub-epicardial vessels. The work of Chilian et al. [22] is one of these rare examples, which reports experimental measurements of pressure in arterial and venous vessels less than 400μm in diameter. In this study, the researchers were interested in determining the active sites of vasodilation due to endogenously-produced adenosine in the beating myocardium of anesthetised cats ($n = 24$). To investigate the redistribution of coronary microvascular resistance they sought to detail microvascular pressure under control and extra-adenosine conditions, via a complex system of micropipette movement control and high-frequency stroboscopic imaging [21, 22]. To induce the extra-adenosine condition, dipyridamole was administered (0.4 mg kg^{-1} min^{-1}, iv) which caused an approximately 40-fold increase in myocardial adenosine levels.

It is our intention to use this pressure data to define Dirichlet pressure BCs on the distal terminal nodes of the porcine arterial network, and to compare the total network pressures to the *same* data for a qualitative assessment. To this end, the data contained in Figure 3 of Chilian et al. [22] was extracted using bespoke data-extraction software. As recommended by the authors, a sigmoidal function was chosen to produce a continuous fit to this discrete data. Specifically,

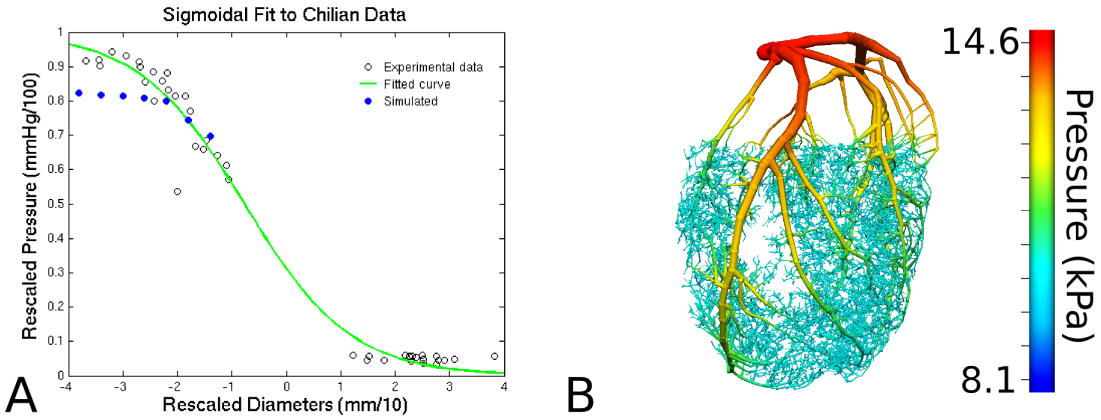


Figure 3.8: (A) Sigmoidal curve (green line) fitted to the data (black circles) from Chilian et al. [22]. Negative(positive) diameters correspond to the arterial(venous) system. The simulated pressures averaged by radii bins are also shown (blue dots). (B) Poiseuille flow pressure solution on the porcine anatomical network using the experimental pressure boundary conditions derived from the curve in (A).

we sought to optimise the parameters of the following function with respect to the experimental data:

$$S(x;a,b) = 100\left(1 - \left(\frac{1}{1+e^{-a((x/100)+b)}}\right)\right),\ x \in [-400, 0]. \tag{3.3.1}$$

The optimised parameters were found to be $a = 1.0057$, $b = 0.7407$, and this fit was calculated using a non-linear fitting function from a commercial software package (MATLAB R2012b, The MathWorks Inc., Natick, MA, 2000). The extracted experimental data and the optimally fitted sigmoidal curve, S, are shown in Figure 3.8(A). The root pressure was assigned a value of 14.6kPa (see Table 2 of Chilian et al. [22]), and the remaining terminal pressures were assigned according to S. The resulting Poiseuille pressure field is visualised on the network geometry in Figure 3.8(B). To compare the simulated pressure from the network, all nodes with diameters in the range $0 - 0.4$mm (the experimental data did not report pressure data for vessels greater than 0.4mm) were grouped in consecutive bins of width 0.04mm and their average pressure per bin was cal-

culated. These simulated pressures are directly compared to the experimental data in Figure 3.8(A). These results are promising, but caution should prevail when comparing unequal network preparations. The experimental pressures were measured in live cats whereas our simulated results were computed on a cryomicrotome-derived, and hence static, porcine network.

Finally, it is worth noting that the technique used to measure the vascular pressure is not suitable for clinical use as the experimental protocol: *(i)* requires direct access to the heart via a thoracotomy, *(ii)* uses high-frequency jet ventilation synchronised to the cardiac cycle to eliminate respiratory-induced cardiac movement, *(iii)* applies several 22-gauge needles to enable partial immobilisation of the heart, thereby preventing out-of-plane movement of the myocardium relative to the imaging system.

3.4 Discussion

Vascular Reduction

The vascular reduction process described in this chapter is a necessary step in order to produce an arterial vascular model that is applicable to: *(i)* our current multi-compartment Darcy perfusion modelling framework, and *(ii)* the future anatomically-based hyperporoelastic modelling framework. This step also highlights one of the main advantages of the continuum modelling approach over its more discrete counterparts. The discrete arterial network has many unknown BCs that are difficult to validate, whereas the continuum models require simply a coronary root pressure and either a typical capillary pressure (for the models presented in this thesis) or ideally the right atrial pressure (for a model

featuring explicit venous compartments also). This latter case is particularly of interest as these two BCs are easily measurable *in vivo* using pressure catheters.

Radius Estimation: Importance and Confounding Factors

In conjunction with sensible BCs, one also needs a reliable method of estimating the vessel radii. The importance of the radii is obvious given that the Poiseuille conductance is proportional to the fourth power of the radius (see Eq. (2.2.2)). One can appreciate that an error in the radius estimation process is greatly magnified in terms of the model flow solution. For example, to examine the sensitivity of the Poiseuille flow model to radius estimation, the estimated radii across the network were varied by $\pm 10\%$, while keeping the remaining model parameters constant. Unsurprisingly, this produced a significantly greater alteration to the total network influx, which varied from -35% to 48% with respect to the reference influx (see Figure 3.9).

For this reason, great effort has been made to improve the image processing aspect of the radius estimation by our research group [49]. However some key challenges with the raw data have been identified:

- The failure of the LV cavity balloon to deploy correctly has resulted in some data sets being frozen, and subsequently imaged, in unphysiologi-

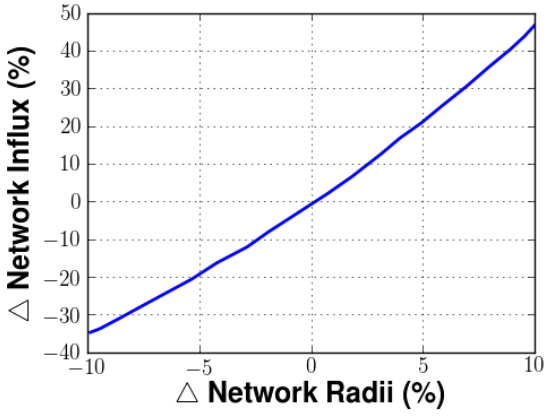


Figure 3.9: Effect of vessel radius on total network influx. The radii from all vessels of the porcine left ventricular reduced model were varied by $\pm 10\%$. Constant pressure boundary conditions of 12.5kPa - 3kPa were applied to the root and distal terminal nodes respectively. For this model, one can see that such a change in radius can lead to an almost 50% change in fluid influx.

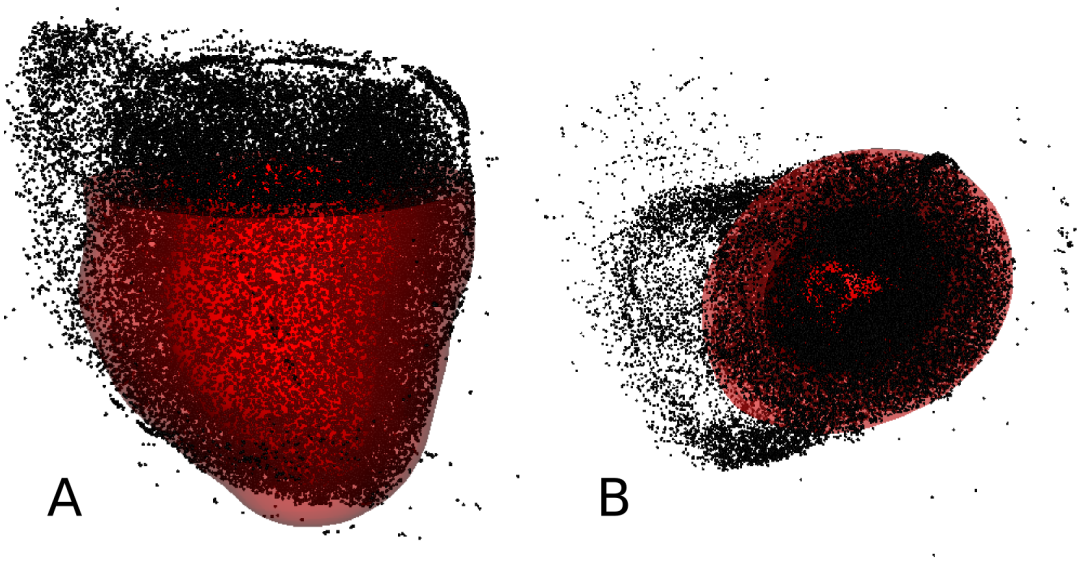


Figure 3.10: Carmine microsphere distribution for the porcine heart. Each black dot represents an individual microsphere, the location of which has been determined by post-processing of the cryomicrotome data stack. The LV tissue model is shown in red. (A) Long axis view. Conglomeration of microspheres are visible towards the base of the heart. These are microspheres that have lodged within the large coronary arteries, most notably in the LCX. (B) Short axis view. Displacement of microspheres by the cutting action of the cryomicrotome is apparent by the microspheres lying remote to the cardiac volume.

cal states.

- Smearing of thawed vascular casting agent disfigures the cross-sectional profile of vessels, thereby making an accurate radius estimation extremely difficult (see Figure 2.2, in particular the anterior portion of the LV).

- The influence that microsphere deposition studies have on the distribution of the vascular casting agent has not yet been clarified. Most vascular casting experiments are conducted concomitantly with microsphere deposition studies for the practical reason of maximising the data obtained from a specific experimental preparation. Microsphere distributions are frequently used as the 'gold-standard' for regional absolute perfusion quantification [89, 115], and they offer a unique insight into the

optical characteristics of tissue [49]. A systematic study of the number of microspheres one can inject into a single heart while retaining a high-level of confidence in the efficacy of the vascular casting procedure is certainly desirable, however obtaining this data would be expensive. Until such a study is done, there will remain uncertainty as to the effect of microsphere deposition on the distribution of the casting agent. This is turn limits the usefulness of comparing microsphere distributions with flow based on the *extracted* vascular model, as microspheres are deposited based on flow within the true network.

This last point is the primary barrier is using microsphere distributions to validate a continuum perfusion model. There are a series of secondary factors that further contribute to the difficulty of such a validational approach: *(i)* Microspheres are displaced by the cryomicrotome blade during the slicing and imaging process, as demonstrated in Figure 3.10. Indeed, this problem should be expected given that the microspheres are typically 15μm in diameter, and the slice thickness can be as small as 40μm [145]; *(ii)* Microspheres can be seen to deposit along the major arteries (see the linear aggregations in the basal portion of Figure 3.10(a)). This is undesired as the use of microsphere distributions as a surrogate for perfusion assumes that they are all lodged in the pre-capillary arterioles; *(iii)* The myocyte contractile machinery was not decoupled from the calcium concentration state of the cell, and momentary spontaneous myocardial fibrillation can occur during the experiment. This intrinsic activation is an uncontrolled variable within the experimental framework. One might assume that an actively contracting myocardium, and thus its associated deforming vascular network, would produce a different flow distribution to a wholly static

domain (for further discussion on this issue, see Section 5.2); and *(iv)* 'skimming effects', whereby the flow of microspheres at asymmetric vessel branches does not represent the flow of the fluid [105], cannot be incorporated into the continuum perfusion models where discrete factors such as bifurcation junctions are not represented.

Experimental and Modelling Feedback

The points of discussion outlined above are further indications for the need of a close collaboration between experimentalists and modellers. Closer collaboration should lead to improved data quality, and the optimisation of experimental efforts, the critical use of animal models, and research funding. It is also important to develop methods of testing and validating extracted vascular models. Encouragement can be taken from the favourable comparison of the discrete flow pressure to the experimental results, as shown in Section 3.3. Although these results must still be interpreted with caution, as in making this comparison, one has intrinsically applied an epicardial vessel scale-pressure relationship across the whole heart, ignoring the effects of intramural myocardial pressure. For the purposes of this thesis however, we can conclude that cryomicrotome imaging provides the cardiac modelling community with unique data, and that a robust method to extract both LV tissue geometry and the embedded anatomical arterial model has been presented. In the following chapter, this data is used to biophysically parameterise the Darcy porous domains.

Summary

A method for constructing anatomically-based LV tissue and vascular models has been described, and successfully applied to a canine and a porcine cryomicrotome data sets. Due to the issue of unknown boundary conditions for terminal vessels, and the need for a porous domain suitable for deforming perfusion models, the arterial vascular models have been reduced to those vessels that perfuse the LV myocardial model only. The key attributes of cryomicrotome-derived arterial networks have been discussed, along with their weaknesses. This includes the main challenges surrounding the experimental protocols with respect to the accuracy of the extracted vascular models and validation of the subsequent flow solutions. The resulting reduced vascular models can, for the first time, be used to parameterise our multi-compartment Darcy perfusion model in a biophysical manner, as shall be seen in the following chapter.

4

Darcy Model Parameterisation: Application to Anatomical Networks

The results based on the synthetic network of Chapter 2 have shown that it is possible to sensibly incorporate discrete vessel data into continuum perfusion models. Yet, one should not assume that the same is true for anatomically accurate vascular networks due to natural variability of biological vasculature and the application of complex experimental and image enhancing processes to construct the vascular model. Furthermore, no previous study has used an anatomical vascular model to parameterise porous compartment parameters. In this chapter, a systematic comparison of methods is undertaken to test and quantitatively compare parameterisation methods. Some of the more subtle properties of the perfusion model itself are simultaneously revealed, such as the model sensitivity to the number of porous compartments and the robustness of the model to the selection of the coupling point between the 1D 'feeding arteries' and the 3D continuum model.

This chapter commences with a description of the parameterisation methods for anatomical models. Firstly, the size of the 1D model component is defined

in Section 4.1.1. Then the parameterisation methods for the anatomical models are listed in Section 4.1.2, and the treatment of the BCs is stated in Section 4.1.3. The various anatomical model results and analyses are presented in Section 4.2, and are subsequently discussed in detail within Section 4.3.

4.1 Parameterisation Methods

In this section, all required parameter fields for the continuum perfusion model are derived. For an overarching picture of how these fields are related to each other and to the original data, see Figure 4.1.

4.1.1 1D Model Component and Vascular Partition

A proximal portion of the LVM was designated as the 1D model component, and its vessels were not used to parameterise the Darcy permeability or pressure-coupling fields. Rather, a Poiseuille flow solution was solved on the entire LVM, with the flux exiting the terminal vessels of the selected 1D model component being used to define element-wise volumetric source fields within the Darcy model *i.e.* s_i in Eq. (2.1.1)(b). A variable yet robust method of defining this 1D model component was required such that its size can be easily adjusted, according to the needs of the specific application or available data. The chosen method of extraction was to fix a threshold radius value (τ) and then determine the set of all LVM nodes that reside within the LV tissue model and have a radius $r \geq \tau$, denoted $\Theta(\tau)$. The 1D model component was then defined to be the union of the vessels from each PLR (see Section 3.2) from each node of $\Theta(\tau)$ to the root node of the LVM (Figure 4.2).

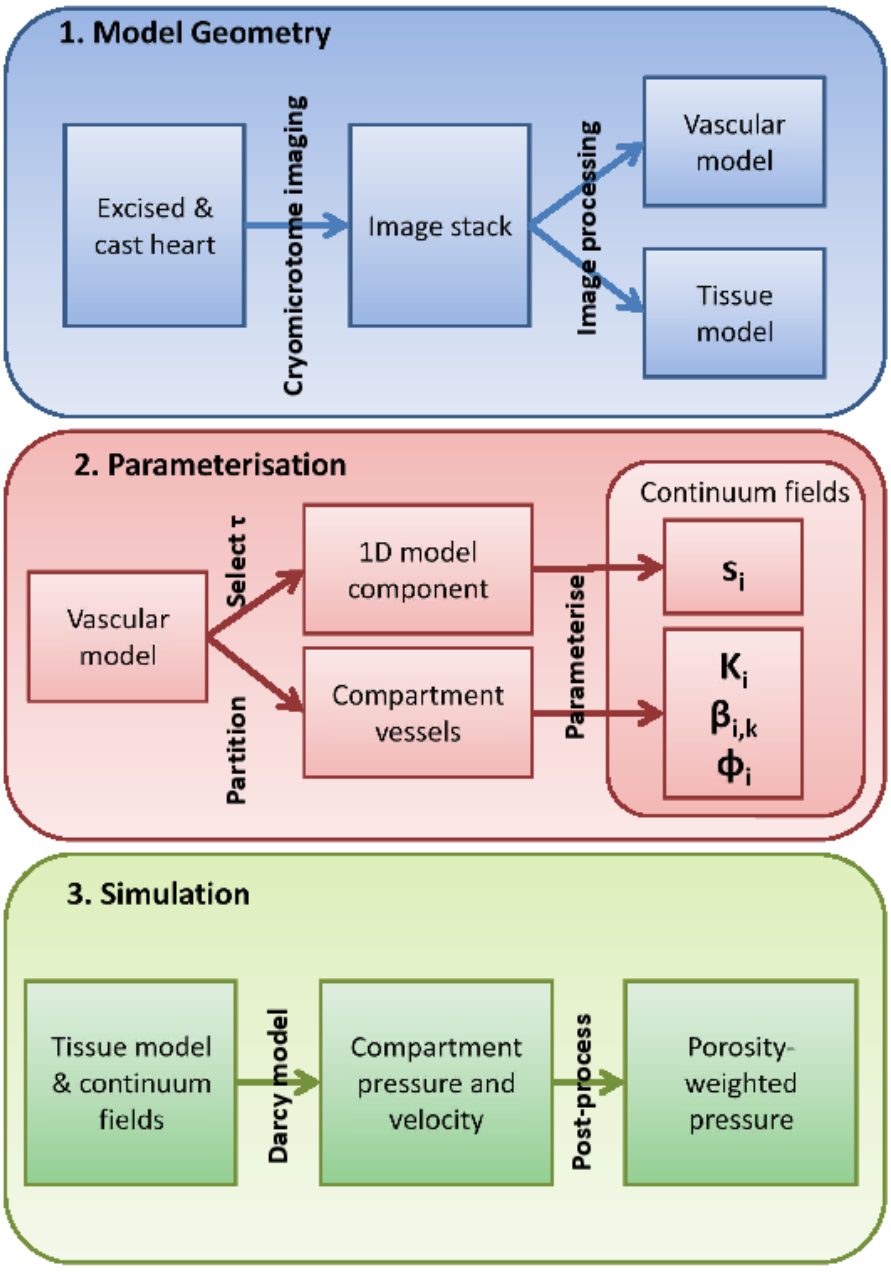


Figure 4.1: Schematic of the anatomically-derived perfusion model parameterisation process. The first component, 'Model Geometry' was described in Chapter 3. The 'Parameterisation' component is the subject of Section 4.1. One can see from which discrete model component the continuum model parameters are derived.

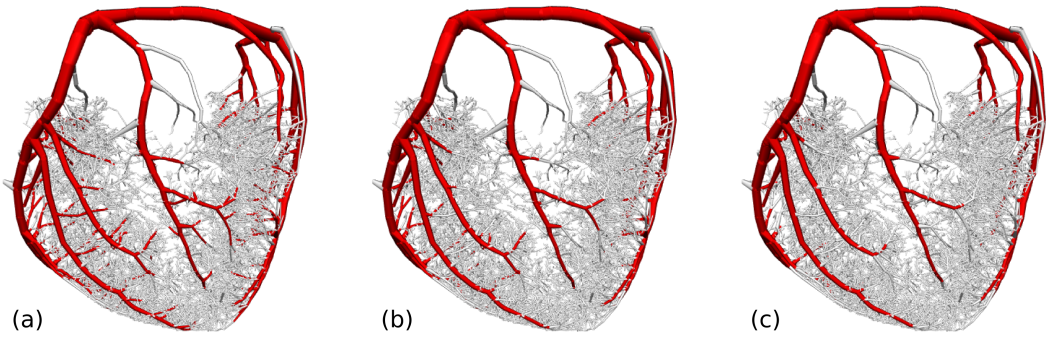


Figure 4.2: The porcine left ventricular vascular model whereby the various proximal 1D components (displayed in red) are defined by the radius threshold, τ, of values (a) 0.2 (b) 0.25 (c) 0.3 mm. The spatial distributions of the incoming volumetric flux fields for the continuum component, s_i, are dependent on the 1D model component size.

Prior to the partition of the network into the groups for the parameterisation of individual porous compartments, one must first decide on the number of porous compartments to apply in the model. Experimental data suggests that $N = 2, 3$ are reasonable values for the number of Darcy compartments (see Section 4.3 for discussion surrounding the choice of N range). Thus, in conjunction with the capillary compartment, the remaining $N - 1$ arterial Darcy compartments were anatomically parameterised using the discrete vascular data. The capillary vessels are below the resolution of the cryomicrotome data and thus do not feature in the discrete LVM. Due to this lack of explicit data, the capillary compartment was parameterised using a simple isotropic permeability field of 0.1 $\text{mm}^2\ \text{Pa}^{-1}\ \text{s}^{-1}$ [19]. Note that the subsequent results were found to be insensitive to this parameter within the range 0.01–1.0 $\text{mm}^2\ \text{Pa}^{-1}\ \text{s}^{-1}$.

For the chosen value of N, the discrete vessels were partitioned, or compartmentalised, into groups corresponding to each of the $N - 1$ anatomically parameterised Darcy compartments via the hierarchic parameter field ζ, as described previously in Section 2.2.3. In order to define ζ for anatomical networks, and overcome the issue of looping pathways, each vessel was assigned

to a unique proximal vessel by means of its greatest incoming flux from a Poiseuille model simulation (the applied discrete BCs for this simulation are presented in Section 4.1.3). For $N = 2$, there is a trivial partition vector of $\zeta = [1, 0]$ *i.e.* all LVM vessels not in the 1D model are used to parameterise the first Darcy compartment. For the case of $N = 3$, the set of discrete vessels to be spatially-averaged is divided equally between the two compartments (in terms of total number of vessels), to the extent that the hierarchic parameter field will allow. For example, the porcine model partition vector for $\tau = 0.3$mm is $\zeta = [1,\ 8.67 \times 10^{-5},\ 0]$ – determined via the bisection method, and it yields an almost equal split in vessels between the first and second Darcy compartments (13,497 and 13,498 vessels respectively). This vascular partition method is suitable for this study where the parameterisation process itself is being investigated. Otherwise, the point of partition with respect to ζ should be guided by the specific model application (see Table 4.1 for examples of application dependent vascular scales of interest).

4.1.2 Anatomical Parameterisation Methods

In the anatomically-based porous perfusion results presented below, there are three different anatomical vascular models used, and each one concerns an individual question that the particular vascular model was specifically chosen for.

Firstly, a cuboid of male Wistar rat myocardium tissue (of dimension approximately $2 \times 2 \times 1$mm) was imaged by micro-CT and then reconstructed into a vascular model. The purpose of this model is to examine the applicability of the same permeability methods as featured in Chapter 2 to a clearly anisotropic

network.

Secondly, a single arterial subtree was extracted from the full porcine LV model. The aim of this model application is to investigate the importance of general-connectivity β fields as opposed to strictly-hierarchical connectivity only. The specific question was: is it important to allow flow between non-neighbouring compartments *i.e.* compartments whose indices i, j are such that $|i - j| > 1$? The permeability method of median complexity was chosen, *i.e.* the PCA method for this study, as defined in Chapter 2.

Thirdly, a comprehensive approach is applied to the parameterisation of the entire anatomical left ventricular models whereby the permutations of $\boldsymbol{K}$ and β parameterisation methods are simultaneously tested on the same vascular models. To reduce the computational burden of an expanded set of methods to be permuted, the median complexity method, projected-PCA, was sacrificed. This choice was made based on the findings of Chapter 2 and the requirement of relatively computationally expensive operations such as the covariance calculation and vector projections for the PCA method. Specifically, the methods tested are listed below in decreasing order of their usage of detailed vascular information:

(i) M_{HvC} – the method of Huyghe and Van Campen [56] is used to define the permeability, and anatomically-derived β fields were applied,

(ii) $M_{\phi \boldsymbol{I}}$ – porosity-scaled isotropic permeability fields and anatomically-derived β fields were applied,

(iii) $M_{\boldsymbol{I}}$ – isotropic permeability fields and anatomically-derived β fields were applied,

(iv) $M_{\phi \boldsymbol{I} c\beta}$ – porosity-scaled isotropic permeability fields and constant/ homogeneous β fields were applied, and

(v) $M_{\boldsymbol{I} c\beta}$ – isotropic permeability fields and constant/homogeneous β fields were applied (*i.e.* no vascular data was used).

4.1.3 LVM Boundary Conditions

Zero flux BCs were applied on $\partial\Omega$, and the flow was driven by volumetric source fields, s_i. These source fields were derived from the Poiseuille flow through the LVM, which had prescribed pressure BCs of 12.5kPa at the root node, and 3kPa at its terminal nodes. The s_i are also dependent on the 1D model component size as determined via τ, for example, a smaller τ value would include more vessels in the 1D model component and the source fields exiting these vessels would be more homogeneously distributed throughout Ω. Specifically, the flux through each terminal vessel of the 1D model component was taken to be the flux from the corresponding vessel of LVM, and these fluxes were spatially mapped to the corresponding finite element from the LV myocardial mesh to form the source fields. For a given value of τ, the terminal fluxes were linearly scaled such that their total was equal to the total flux through the entire LVM, this ensures consistency amongst 1D model components and that the same volumetric influx is applied for all simulations. Note that for the networks and values of τ applied in this thesis, the only non-trivial in-flow source field is s_1. Finally, a pressure-dependent sink term, compatible with the discrete model BCs, was applied for s_N of the form

$$s_N = N_s(p_N - p_{cap}), \tag{4.1.1}$$

Action	Diameter range A	Diameter range B	Animal	Reference
Dipyridamole	$> 170\mu$m 67% decrease in CVR	170μm – *150μm 92% decrease in CVR	Cat	[22]
Nitroglycerin	300μm – 100μm 90% relaxation	100μm – 60μm No effect	Pig	[123]
Coronary arterial occlusion	$> 150\mu$m 11.9% constriction	$< 150\mu$m – 10μm 10.4% dilation	Dog	[30]
Critical stenosis	$> 150\mu$m 6.9% constriction	$< 150\mu$m – 10μm 15% dilation	Dog	[30]
Coronary perfusion pressure (60 mmHg)	$> 100\mu$m No effect	$< 100\mu$m – 10μm 17% dilation	Dog	[65]
Coronary perfusion pressure (40 mmHg)	$> 100\mu$m 13% constriction	$< 100\mu$m – 10μm 11% dilation	Dog	[65]

Table 4.1: Effect of various actions on different coronary vascular ranges. *venous as opposed to arterial vessel diameter.

similar to Michler *et al.* [97], where $p_{cap} = 3000$ Pa is the capillary pressure parameter and $N_s = 0.1$ mm^3 Pa^{-1} s^{-1} is the constant of proportionality between the pressure difference $(p_N - p_c)$ and the sink field strength s_N.

4.2 Results

For single porous compartment comparisons, the root-mean-square error as defined by Eq. (2.4.1) is once more used to quantify and compare the continuum model results. Note that for the remainder of the dissertation only the spatially-averaged discrete pressure is compared to the continuum model pressure *i.e.* $\triangle = \triangle_p$. In the eventuality that several porous compartments are being comparing, the total pressures fields were defined by the cumulative porosity-weighted compartment pressures *i.e.* ,

$$a_0 = \sum_{i=1}^{N-1} \phi_i \cdot a_i, \tag{4.2.1}$$

where a is $\overline{p}$ or p for the spatially-averaged discrete or continuum pressures respectively. These total pressure fields are then normalised and compared in our usual manner as described in Section 2.4.

4.2.1 Capillary Anisotropic Network Test

To further examine the merits of each $\boldsymbol{K}$ parameterisation method presented in Section 2.3.2, one considers the anisotropic network shown in Figure 4.3. This vascular model was constructed from confocal data imaged from a rat left-ventricle tissue wedge, with radii ranging over $1 - 84\mu$m [83]. This network has

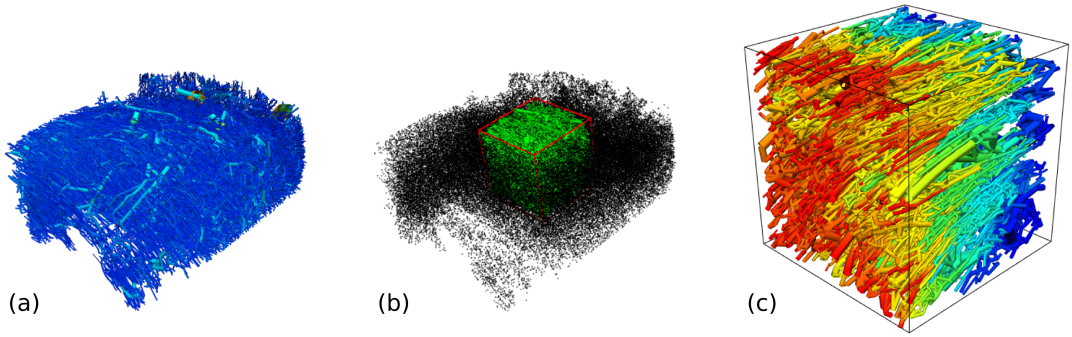


Figure 4.3: (a) A vascular model resulting from a confocal study of a rat LV tissue wedge. (b) The depicted cube shows the location of the extracted vessels of Case 1 in relation to the sample in (a) (see also Table 4.2). (c) Poiseuille pressure was solved on the extracted subnetwork with pressure boundary conditions on two opposing faces (input pressure of 2kPa and outflow pressure of 1kPa), and no flux conditions on all other terminal nodes. Note that the subnetwork has been rotated from the view in (b).

a clear preference of vessel direction, with the vessels (predominantly capillaries) being generally aligned with the local myofibres, as well as being organised into inter-weaving sheets. A cube of side length 0.67mm was selected from the block, which has dimension 1814 x 2243 x 671 μm. Pressure BCs of 2kPa and 1kPa were assigned to all terminal nodes on two opposing faces, while the remaining terminal nodes were constrained to have zero flux. The averaged Poiseuille pressure was calculated at regular grid points, which were simultaneously parameterised using the various $\boldsymbol{K}$ parameterisation methods. Equivalent Darcy pressure/flux BCs were applied in order to match the discrete model

Case	ϕ**I**	**PCA**	**HvC**
1	1.239e-01	1.085e-01	9.330e-02
2	1.189e-01	1.049e-01	9.773e-02

Table 4.2: Root-mean-square error values between the continuum and spatially-averaged discrete pressure fields for the anisotropic networks extracted from confocal imaging data of a rat left ventricle tissue wedge. Observe that the projected-PCA method has outperformed the porosity-scaled isotropic permeability assumption. Case 1 is illustrated in Figure 4.3. Case 2 is another extracted subnetwork from the same wedge that does not share any vessel with the Case 1 network.

as closely as possible, *i.e.* 2kPa and 1kPa Dirichlet pressure BCs were assigned to the associated flow faces, and zero flux was enforced on the remaining four faces.

The results displayed in Table 4.2 demonstrate that once more the HvC method has the lowest rms error of the three methods. Of greater interest given the purpose of this particular study, a significantly smaller rms error is obtained from the projected-PCA method in comparison to the isotropic assumption, suggesting that the local vessel directionality is more effectively captured by the former method, as one might reasonably expect given the anisotropic nature of the network.

4.2.2 Single Arterial Subtree Reveals the Importance of β

A single arterial subtree was targeted for this study (see Figure 4.4(a) to determine its location relative to the LV). There was no unique or distinguishing feature to this subtree that would otherwise bias the study result. A binary mask of the tissue volume containing vessels of the chosen arterial tree was manually segmented. A tetrahedral mesh consisting of 66,780 elements (with a mean edge length of 783μm) was subsequently constructed from this binary mask using the open-source meshing software *NetGen* [1]. To parameterise the continuum perfusion model for this region, the subtree was extracted from the porcine LV geometry (for further details on the extraction algorithm, see Section 6.2.1). We chose $N = 3$ as this is the minimum number of compartments that can have non-neighbouring vessel connections. The projected-PCA method was used to parameterise the permeability tensor fields with an RVE of radius 3mm. The

[1] http://www.hpfem.jku.at/netgen/

average compartmental porosities were 0.0208 ± 0.0219, 0.0038 ± 0.0029, and 0.0064 ± 0.0044 for compartments 1, 2, and 3 respectively. The effects of having a general-connectivity model for the pressure-coupling was examined by comparing the results to the strictly-hierarchical scenario, *i.e.* $\beta_{i,k} = 0$ for $|i-k| > 1$. Note that by setting a trivial $\beta_{1,3}$ field, we have effectively removed the scaling parameter on this field, and thereby reduced the problem DOFs by one. For comparison purposes, a Poiseuille flow solution was solved on the explicit subtree, using pressure BCs of 11kPa at the root arterial node and 8kPa at the distal terminal nodes. The results are shown in Figure 4.4(b-d). The rms errors were 0.104Pa and 0.509Pa for the general-connectivity and strictly-hierarchical models respectively. This result suggests that the general-connectivity treatment of β, as opposed to strictly-hierarchical connectivity, leads to an improvement of the continuum total pressure field. Applying the latter approach increases the resistivity of the porous domains by constraining 'vertical' flow, and consequently increases the compartmental pressure in the higher compartments (lower indices) which have a higher porosity, thereby causing a significant increase in the porosity-weighted pressure shown in Figure 4.4(d).

4.2.3 Anatomical LV Perfusion Model

As for all the continuum models, the system parameters were determined at the respective tetrahedral mesh nodes. For the canine and porcine models, a spatial-averaging window of size 1.5 times the average element edge lengths was used, which were 4.09mm and 2.82mm respectively.

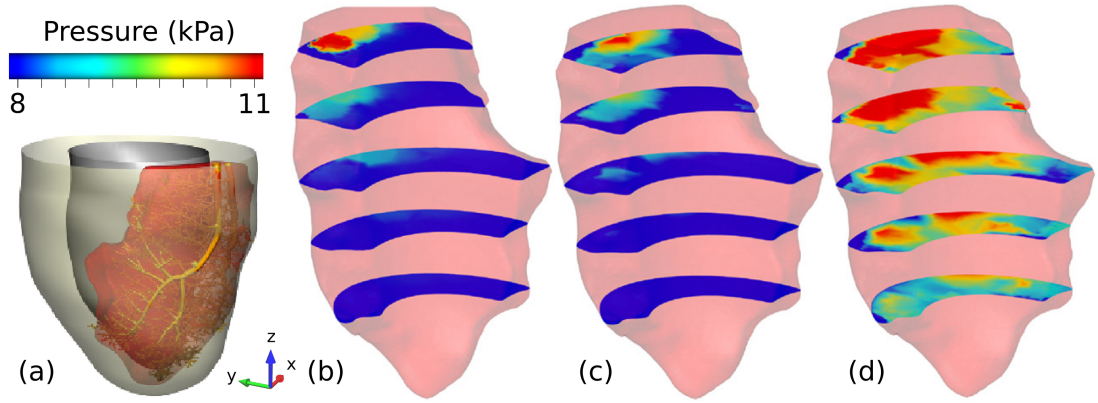


Figure 4.4: A single arterial tree and its subtended volume was extracted for Darcy perfusion modelling. (a) Location of the single artery within the porcine LV geometry. The pressure solution is displayed on several z coordinate isosurfaces for the spatially-averaged Poiseuille solution (b), multi-compartment general-connectivity Darcy solution (c), and the multi-compartment strictly-hierarchical Darcy solution (d).

4.2.3.1 Extracted Porosity Values

It was important to consider the spatial distribution of the continuum porosity field for two reasons: *(i)* to investigate if there was an observable physiological trend for this field with respect to some spatial gradient within the heart, either transmural or apex-base; and *(ii)* to assess the quality of the vascular model, by comparing our data against reported values in the literature. For clarity of presentation, the results presented in this section are for the porcine $N = 2$, $\tau = 0.3$mm model as *(i)* the porcine heart is more similar to the human heart than the canine heart in terms of vascular anatomy[28], and *(ii)* this selection of N and τ yields the largest number of vessels to be spatially-averaged across all porcine model scenarios.

Thus, the porosity field was evaluated at the finite element mesh nodes as per Eq. (2.3.3) (see Figure 4.5(A)). Quantitative analysis was undertaken to investigate potential differences in porosity amongst the septum, the inferior LV, and the lateral LV (the anterior LV was not considered due to the lack of an RCA

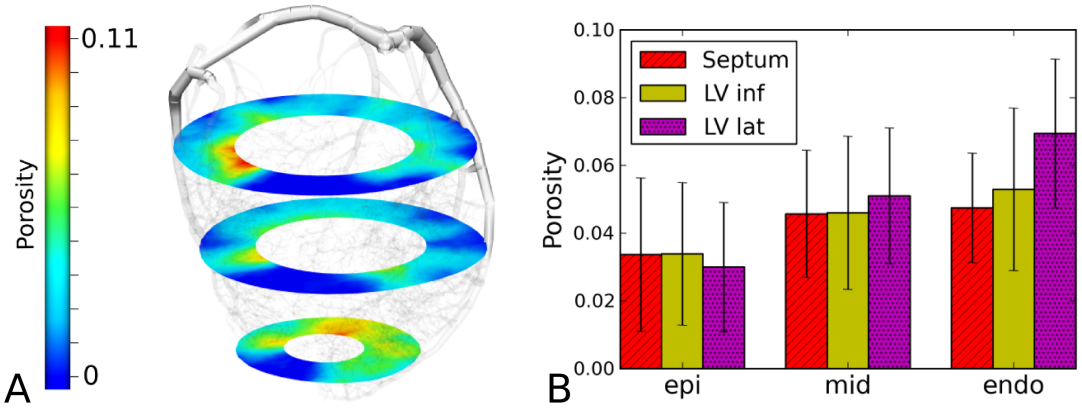


Figure 4.5: Overview of the porosity field for the spatially-averaged porcine coronary arterial tree. (A) Three short-axis slices are displayed at the base, the equator, and the apex. (B) Three distinct regions were considered for quantitative analysis – the septum, the inferior LV, and the lateral LV. The myocardium was further discretised into equal transmural sections representing the epicardium, the mid-myocardium, and the endocardium. The observed regional mean porosities are indicative of a physiological difference between septal and the remaining LV arterial morphology.

model). The myocardium was further discretised into equal transmural sections representing the epicardium, the mid-myocardium, and the endocardium. The calculated regional mean arterial porosities (see Figure 4.5(B)) are indicative of a physiological difference between septal and non-septal LV arterial morphology. Furthermore, the differences in mean porosity between the inferior and septal regions, and the lateral and septal regions were statistically significant (using a one-sample t-test, $P < 0.05$). The average arterial porosity across all three regions was 4.8%. No substantial apical-base porosity gradient was found.

4.2.3.2 Variability of Permeability Properties

In this section, we report on the key properties of the HvC permeability parameterisation method via frequency distribution plots. The following results are for the $N = 2$, $\tau = 0.25$mm model scenario *i.e.* there is only one anatomically-

parameterised Darcy compartment. Initially, there were 5,370 data points distributed within the porcine Left Coronary Artery (LCA) perfused region. For the purposes of analysing this data in meaningful ranges however, 2.23% of these points are not visualised due to their having unusually high permeability values. This finding alone is of great importance as shall be seen in the later Darcy model results, and is discussed further in Section 4.3.

The following statistical properties of interest are displayed: *(i)* Figure 4.6 shows information on the principal flow strengths *i.e.* the $\boldsymbol{K}$ eigenvalues. These have been ordered such that 'Eigenvalue 1' is the largest eigenvalue and 'Eigenvalue 3' is the smallest. Note that all eigenvalues are positive as $\boldsymbol{K}$ is SPD by design. *(ii)* Figure 4.7 shows the distribution of the permeability field determinants, which is given by the product of the eigenvalues. To further analyse the data and extract more physical information from the given data set, the relative anisotropy, denoted Υ, for a data point is defined to be

$$\Upsilon = \frac{\sqrt{(\lambda_1 - \overline{\lambda})^2 + (\lambda_3 - \overline{\lambda})^2 + (\lambda_3 - \overline{\lambda})^2}}{\sqrt{3}\,\overline{\lambda}}, \tag{4.2.2}$$

where λ_i is the i^{th} eigenvalue and $\overline{\lambda}$ is the mean of the three eigenvalues. Thus defined, a Υ value of zero indicates an isotropic permeability whereas increasing Υ is indicative of increased variance in the point-wise eigenvalues. The distribution of Υ values is shown in the inset of Figure 4.7. Finally, statistical properties of each of the derived data fields discussed in this section are quantified and presented in Table 4.3.

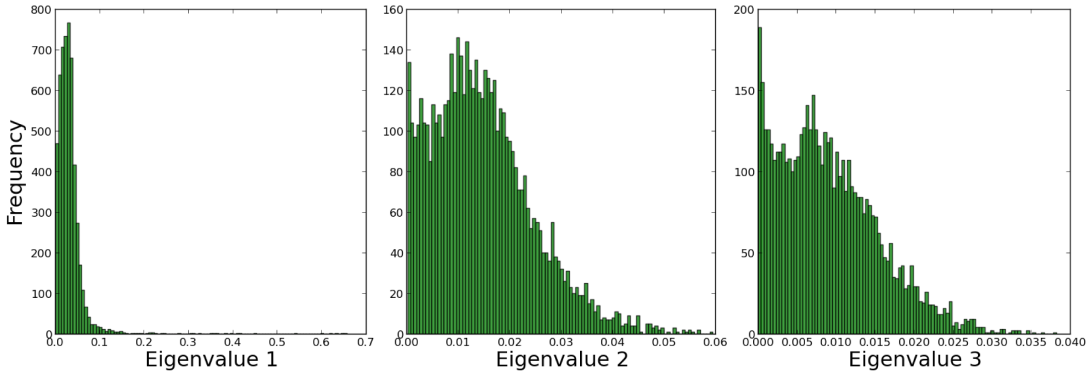


Figure 4.6: Eigenvalue distributions for the permeability field derived using the Huyghe and van Campen method for the porcine arterial model with $N = 2$, $\tau = 0.25$mm. Note the varying x and y axis scales for each subplot.

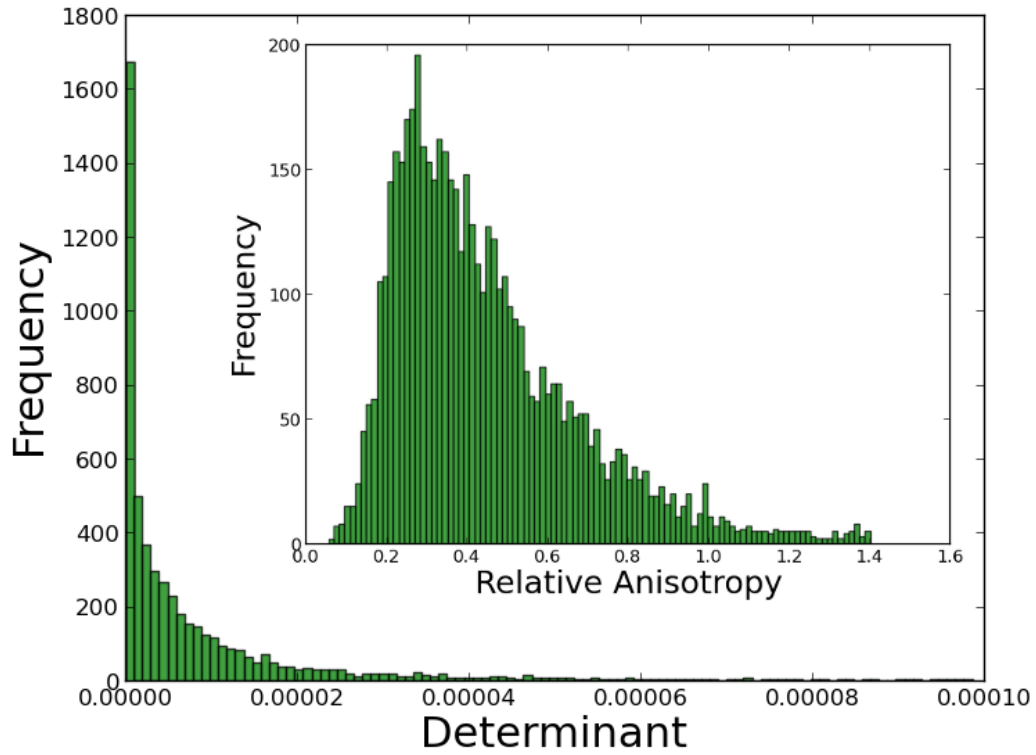


Figure 4.7: (Main figure) Histogram of the determinants of the permeability field derived using the Huyghe and van Campen method for the porcine arterial model with $N = 2$, $\tau = 0.25$mm. (Inset) Histogram of the relative anisotropy calculated from the same determinant field.

4.2.3.3 Effect of Anatomical Parameters

We consider 12 model scenarios, consisting of each possible combination of $N = 2, 3$, $\tau = 0.2, 0.25, 0.3$mm and the canine or porcine coronary model. The dominant factor in terms of reducing the rms discrepancy is the presence of the anatomically-derived β fields (Figure 4.8), as opposed to using homogeneous β fields. The effect of removing anatomical data from the β parameterisation ($M_{\phi \boldsymbol{I}}$ to $M_{\phi \boldsymbol{I} c\beta}$) yielded an average increase of 9.66 ± 6.11 times the rms discrepancy achieved when anatomical data were not used to parameterise the $\boldsymbol{K}$ fields but anatomically-derived β fields were used ($M_{\phi \boldsymbol{I}}$ to $M_{\boldsymbol{I}}$). This clearly demonstrates the importance of anatomically-derived β fields. Overall, the parameterisation methods which did not apply the anatomical β fields did not sustain locally high pressure gradients, and this feature is the primary cause of the increase in rms discrepancy. The finding that it is important to apply anatomical β fields is further supported by observing the relative variability in the spatial distribution of β (Figure 4.9). For an example of this feature, a typical subset of the canine results is displayed in Figure 4.10, specifically showing the porosity-weighted pressure fields and the spatially-varying error between the continuum and discrete models. All continuum fields related to this result are presented in the supporting figures: Darcy velocity components

Field	Mean	Median	Variance
Ev_1	3.232e-02	2.741e-02	1.360e-03
Ev_2	1.481e-02	1.356e-02	9.498e-05
Ev_3	9.078e-03	8.127e-03	4.092e-05
$\lvert\boldsymbol{K}_1\rvert$	8.672e-06	3.239e-06	2.124e-10
Υ	0.448	0.393	0.054

Table 4.3: Statistical properties of the HvC-derived permeability field for the porcine arterial model with $N = 2$, $\tau = 0.25$mm. Ev_i is the i^{th} ordered eigenvalue.

(Figure 4.11); porous domain porosity (Figure 4.12); compartmental Darcy pressures (Figure 4.13); and the spatially-averaged discrete pressures (Figure 4.14). Furthermore, the parameter field scales solved for to minimise the rms discrepancy are presented in Table 4.4, and the well-behaved scaling landscape is shown in Figure 4.15.

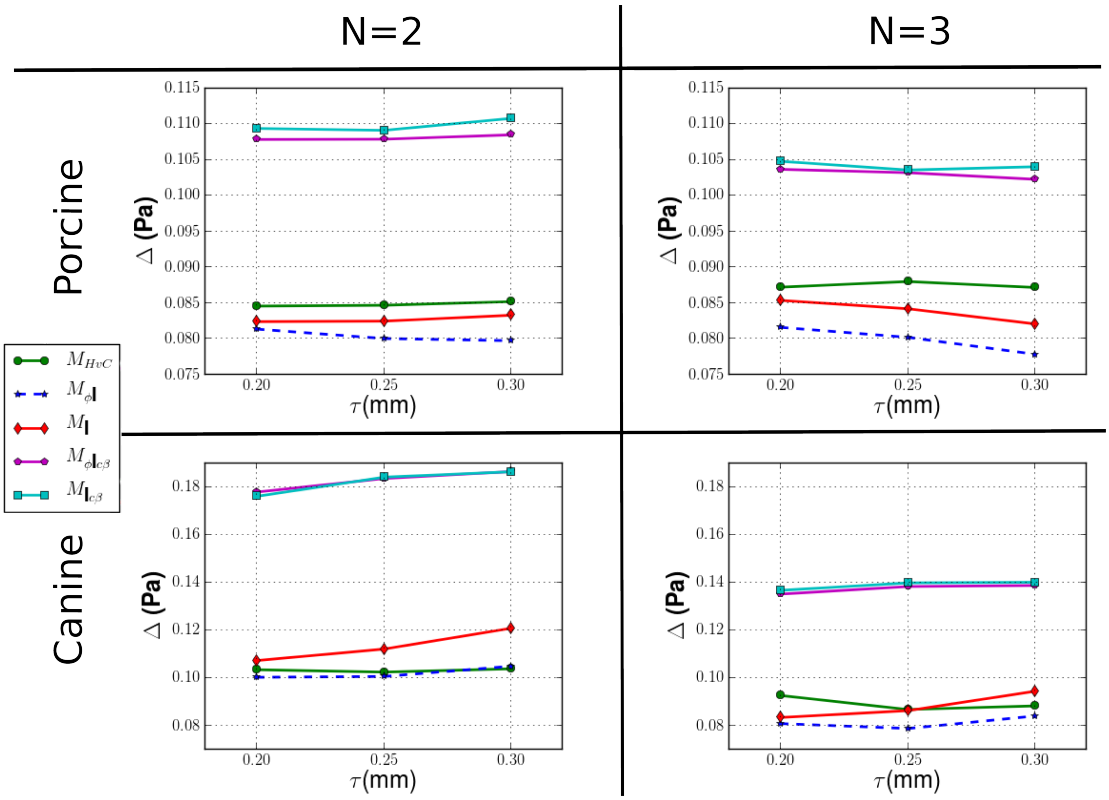


Figure 4.8: Array of plots comparing the various parameterisation methods used. The root-mean-square error, △, compares the porosity-weighted continuum and spatially-averaged discrete total pressure fields. The total number of Darcy compartments applied is N, and the 1D model component size is determined by the variable τ. There is a marked decrease in △ when anatomically-derived pressure-coupling fields are used (methods M_{HvC}, $M_{\phi\boldsymbol{I}}$ and $M_{\boldsymbol{I}}$) as opposed to the methods that assume homogeneous pressure-coupling fields (methods $M_{\phi\boldsymbol{I}_{c\beta}}$ and $M_{\boldsymbol{I}_{c\beta}}$).

With regards to $\boldsymbol{K}$ parameterisation, the porosity-scaled isotropic method ($\phi\boldsymbol{I}$) is demonstrably the most reliable in terms of producing the minimum rms discrepancy, obtaining the minimum in 11/12 of the model scenarios. Note

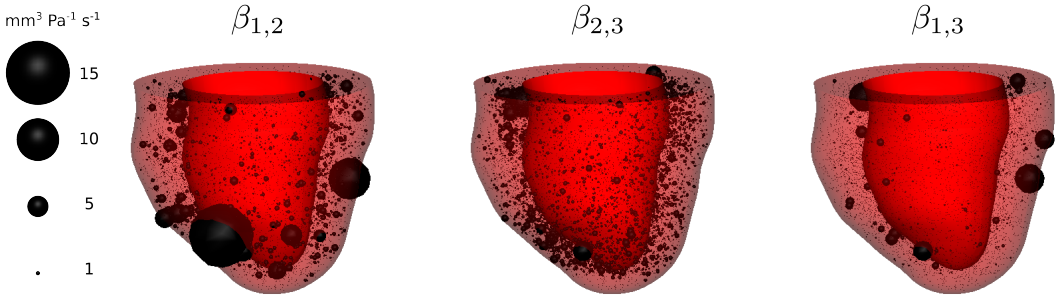


Figure 4.9: The spatial distribution of the continuum β fields allows for heterogeneous mass transfer amongst compartments. Here we consider a three-compartment Darcy model, where the left ventricular endocardial surface is opaque while the epicardial surface is transparent. Each finite element mesh node is represented by a spherical glyph whose diameter is equal to the β value at that node. Note in particular the non-trivial $\beta_{1,3}$ field, which illustrates the level of non-hierarchical coupling in this $N = 3$ model scenario.

that this finding appears to contradict the earlier results of Chapter 2 (see Section 4.3.1 for a discussion of this point).

4.2.3.4 Model Sensitivity to τ and N

We consider here only the $M_{\phi \boldsymbol{I}}$ parameterisation method results to gauge the sensitivity of the perfusion model results to the remaining two parameters of interest – specifically τ which determines the size of the 1D model component, and the number of Darcy compartments, N. The average increase in rms discrepancy going from $\tau = 0.2$mm to $\tau = 0.3$mm was $0.49 \pm 4.53\%$. Such a relatively small change in rms discrepancy is indicative of a high level of robustness to the model results with respect to τ, at least across the tested range $0.2 - 0.3$mm. The addition of an extra Darcy compartment also yielded a reduction in rms discrepancy, with the minimum rms discrepancy value decreasing by 21% and 2% for the canine and porcine models respectively.

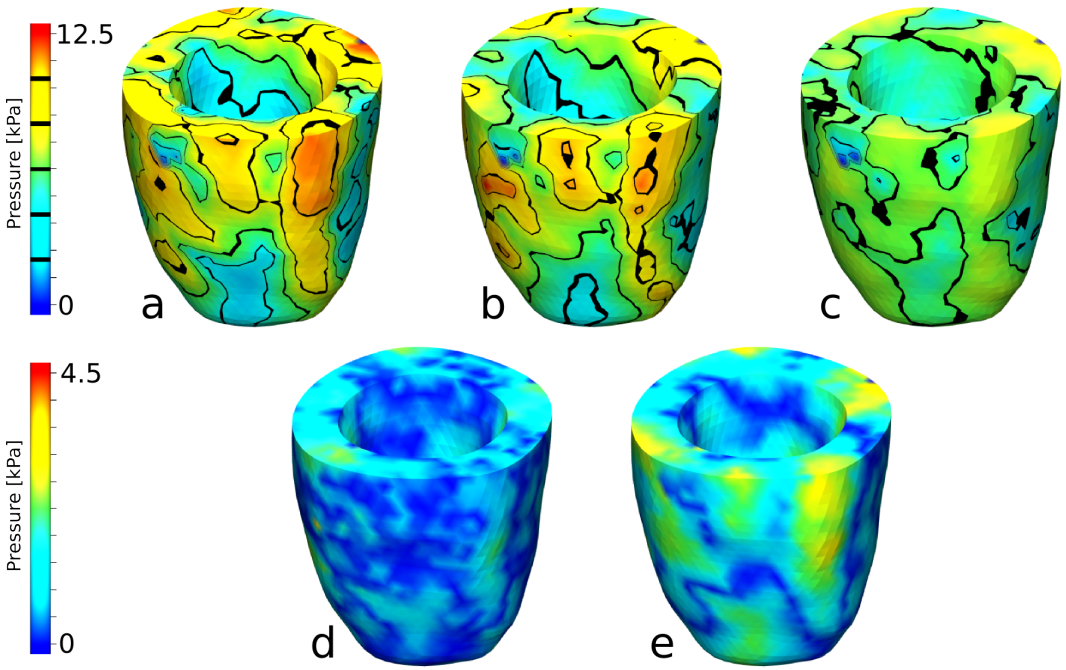


Figure 4.10: Qualitative results for the canine model scenario of two anatomically parameterised Darcy compartments and the 1D model created using τ= 0.25mm. (a) The porosity-weighted spatially-averaged Poiseuille pressure field. (b) The Darcy solution with the minimum rms error of the methods tested was given by the porosity-scaled isotropic permeability with anatomically-derived pressure-coupling fields method (*i.e.* method $M_{\phi \boldsymbol{I}}$). (c) The Darcy solution with the largest rms error of the methods tested was given by the most basic method, which used no discrete vascular data at all (*i.e.* method $M_{\boldsymbol{I}c\beta}$). To further demonstrate the improvements in the model parameterisation by applying the discrete data, the bottom row shows surface plots of the absolute differences. (d) is the difference between (a) and (b), whereas (e) is the difference between (a) and (c).

4.3 Discussion

In this study, a method has been proposed for the incorporation of whole-organ high-resolution anatomical vascular networks within a continuum perfusion model via spatial averaging techniques. This method accounts for the morphology and orientation of vessels across multiple scales of the vascular model, and it provides for a natural scale separation of flow and anatomical characteristics. It has been shown that the inclusion of vascular data significantly

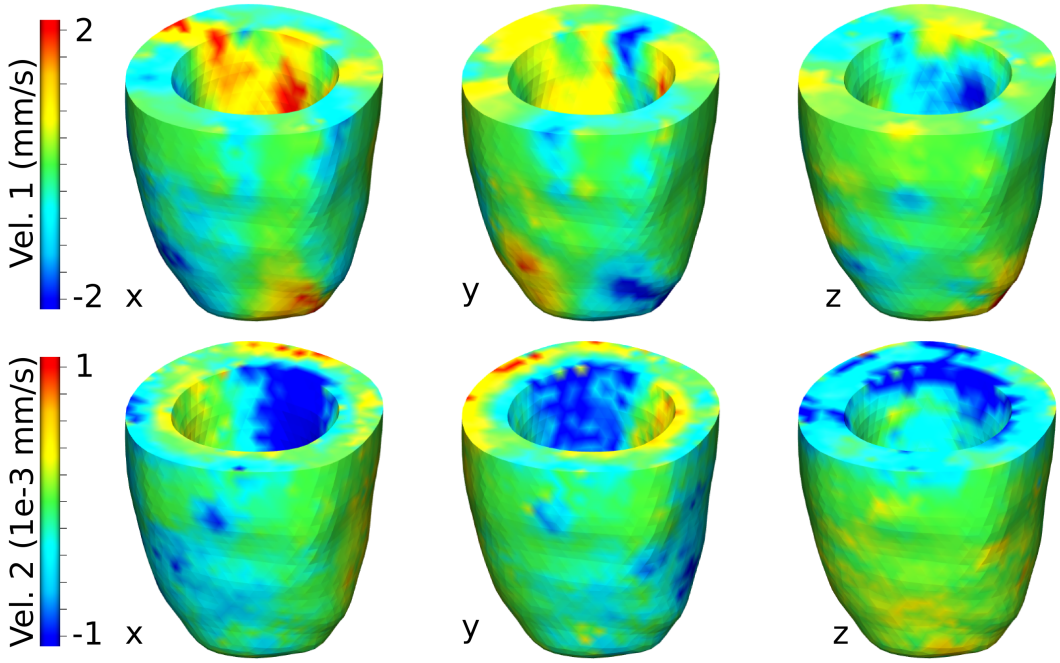


Figure 4.11: Darcy velocity components for the two anatomically-parameterised Darcy compartments corresponding to the simulation results shown in Figure 4.10.

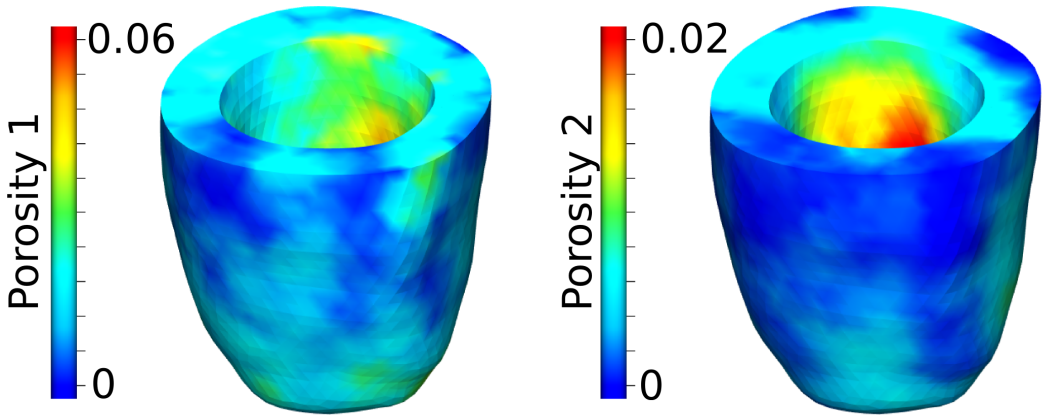


Figure 4.12: Spatially-averaged discrete porosity for the two vascular groups corresponding to the simulation results shown in Figure 4.10.

improves the continuum perfusion results in comparison to a simplistically parameterised model. The results for both the canine and porcine models were definitive with regards to this matter, as shown quantitatively in Figure 4.8 and the qualitative result of Figure 4.10. In particular, the use of anatomically-

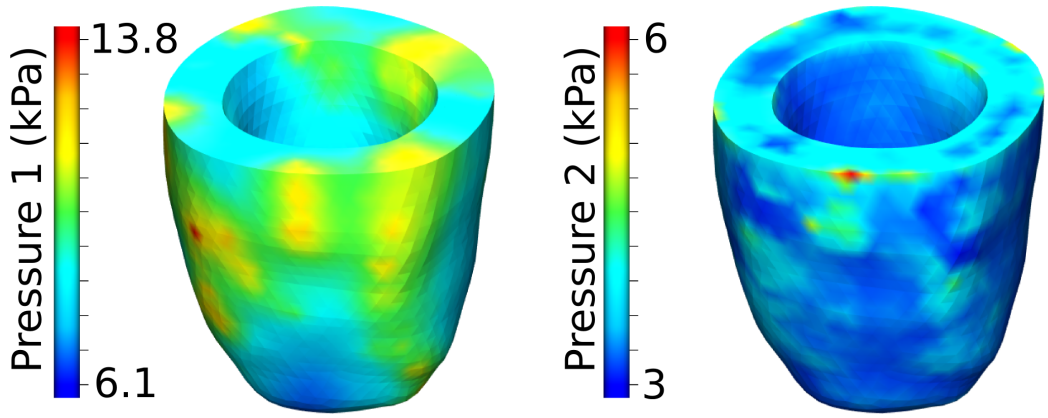


Figure 4.13: Darcy pressure for the two anatomically-parameterised Darcy compartments corresponding to the simulation results shown in Figure 4.10.

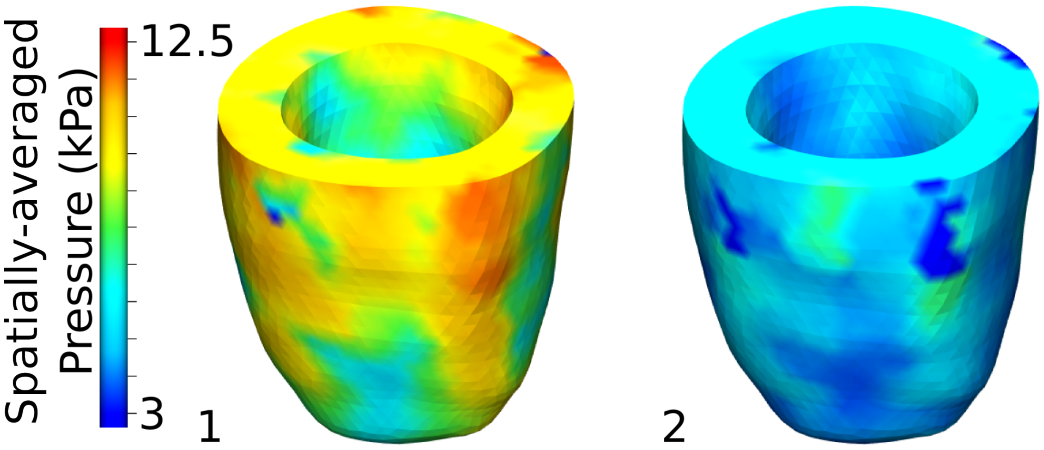


Figure 4.14: Spatially-averaged discrete pressure for the two vascular groups corresponding to the simulation results shown in Figure 4.10.

derived β fields is crucial for the formation of pronounced pressure gradients. Furthermore, it appears that the ability of non-neighbouring compartments to 'communicate' with each other produces more physiological pressure fields (see Section 4.2.2). The parameterisation method consisting of the porosity-scaled isotropic $\boldsymbol{K}$ fields and the anatomical β fields performed best with respect to the minimum rms discrepancy, producing the minimum rms discrepancy in 11/12 model scenarios. We believe that this study represents a substantial step towards an anatomically parameterised porous perfusion model.

Canine Model						
N	2			3		
τ	0.2	0.25	0.3	0.2	0.25	0.3
k_1	1.81e+00	1.21e+00	1.07e+00	1.11e+01	7.08e+00	6.44e+00
k_2	-	-	-	1.00e+00	1.00e+00	1.00e+00
b_1	1.04e-03	1.05e-03	1.05e-03	3.78e-01	3.87e-01	3.90e-01
b_2	-	-	-	8.02e-01	8.02e-01	8.02e-01
$\overline{\beta_{1,2}}$	4.49e-02	4.62e-02	4.87e-02	1.23e-01	1.23e-01	1.22e-01
$\overline{\beta_{2,3}}$	-	-	-	1.44e-04	1.37e-04	1.34e-04
$\overline{\lvert K_1 \rvert}$	1.14e-07	1.14e-07	1.14e-07	1.14e-07	1.14e-07	1.14e-07
$\overline{\lvert K_2 \rvert}$	-	-	-	1.54e-15	1.54e-15	1.60e-15
$\overline{s_1}$	3.18e-01	2.75e-01	2.61e-01	2.61e-01	2.75e-01	3.18e-01

Porcine Model						
N	2			3		
τ	0.2	0.25	0.3	0.2	0.25	0.3
k_1	4.98e+00	4.18e+00	2.88e+00	2.50e+01	1.90e+01	1.18e+01
k_2	-	-	-	2.33e+00	1.76e+00	1.10e+00
b_1	2.63e-03	2.64e-03	2.69e-03	2.67e-01	2.91e-01	3.17e-01
b_2	-	-	-	3.26e-01	4.37e-01	7.26e-01
$\overline{\beta_{1,2}}$	1.12e+00	1.04e+00	1.03e+00	2.79e+00	2.82e+00	2.91e+00
$\overline{\beta_{2,3}}$	-	-	-	2.63e-02	2.56e-02	2.51e-02
$\overline{\lvert K_1 \rvert}$	1.13e-07	1.13e-07	1.13e-07	1.13e-07	1.13e-07	1.13e-07
$\overline{\lvert K_2 \rvert}$	-	-	-	9.73e-12	1.05e-11	1.20e-11
$\overline{s_1}$	4.71e-01	4.38e-01	3.98e-01	4.71e-01	4.38e-01	3.98e-01

Table 4.4: Tables displaying various quantitative results from the continuum model simulations qualitatively shown in Figure 4.10. Each animal model has a total of six simulation results to report on, corresponding to variations in the number of porous compartments used and the size of the 1D model component. The optimised variables displayed in the tables are: k_i, the scale on $\boldsymbol{K}_i$ *i.e.* the anatomically-derived permeability tensor field for compartment i; and b_i, the scale on $\beta_{i,i+1}$ *i.e.* the anatomically-derived inter-compartment, or pressure-coupling, field between compartments i and $i+1$. The derived data displayed in the tables are: $\overline{\beta_{i,j}}$, the average value for the $\beta_{i,j}$ field; $\overline{|\boldsymbol{K}_i|}$, the average value for the determinant of the $\boldsymbol{K}_i$ field; and $\overline{s_1}$, the average value for the compartment 1 source field.

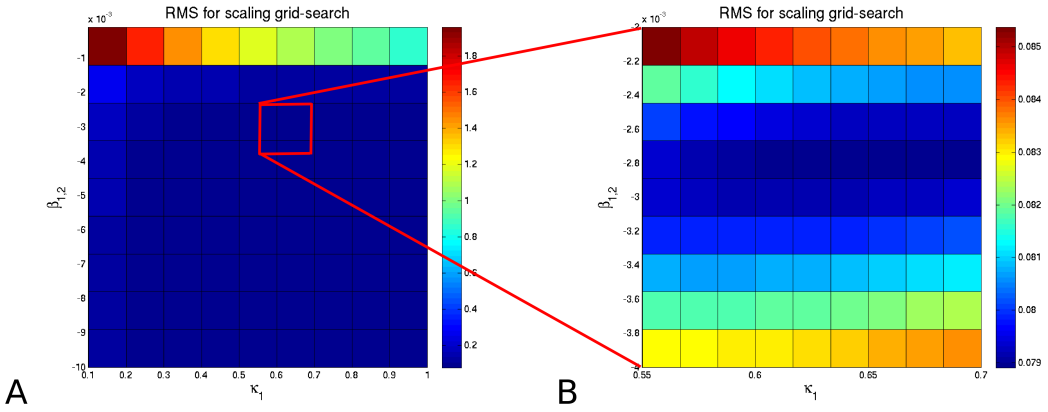


Figure 4.15: Scaling landscapes for the two scales κ_1 (scaling the permeability field $\boldsymbol{K}_1$) and $\beta_{1,2}$ scale corresponding to the simulation results shown in Figure 4.10. Note that (B) is a zoomed-in subsection of (A). The scales that minimised the rms error were found using a standard non-linear Newton-Raphson optimisation solver.

However, the quantitative results also point to key issues associated with using experimentally-derived vascular models to parameterise the Darcy component.

4.3.1 Limitations of Darcy Parameterisation via Anatomical Networks

The creation of an anatomical vascular model from the experimental data is a difficult and complex process [49, 54]. The occurrence of an error or artifact during this process could lead to a failure to extract all vessels within the theoretical range established by the imaging modality. If an extraction failure occurs at a proximal portion of the network (or indeed if an unsuitably small τ value is applied) then a region of artificially high volumetric source and low permeability would result. This lack of local permeability implies that the mass influx could only dissipate through 'vertical' transport (*i.e.* mass transport to another Darcy compartment), potentially causing an unphysiological spike in pressure. This phenomenon would be exaggerated in the $N = 2$ scenarios as the only

other compartment is then the capillary compartment, which has a prescribed distributed pressure sink term, thereby constraining the pressure field for this compartment. Thus all efforts should be made to perfect the vascular model creation process.

More importantly, the HvC method failed to produce the minimum rms discrepancy in all but one model scenario (see Figure 4.8 for the canine $N = 2$, $\tau = 0.3$mm case). This is contrary to the observations in Hyde *et al.* [59] (Chapter 2 of this thesis), where the HvC method consistently yielded the best results. The principal difference between that study and the work of this chapter is the form of the vascular model. Unlike a synthetic network which was constructed in a repeatable and robust manner with determinable network statistics, the anatomically-derived networks are less regular. A statistical analysis of the HvC permeability field determinants for the porcine case $N = 2$, $\tau = 0.3$mm (*i.e.* the case with the worst performance of the HvC method) revealed that there were 10.8% mild outliers defined via the Inter-quartile Range (IQR) of the determinant field (specifically, this is defined to be $> Q3 + 1.5 \times IQR$, where $Q3$ is the 75^{th} percentile), and 5.5% extreme outliers (defined to be $> Q3 + 3 \times IQR$). These extreme outliers were all associated with relatively small length vessels. While the cause of some of these small length vessels was traced to the skeletonisation of the imaging data stack, some also appeared to be genuine features of the vasculature, observable in the original data images. As an illustrative example, imagine the scenario of two adjacent bifurcations. Now allow the vessel connecting these bifurcations to decrease in length. As the two bifurcations tend towards a single trifurcation, the connecting vessel length tends towards zero, and thus by Eq. (2.2.2) the Poiseuille conductance, C, tends to infinity. In this fashion, we can appreciate how a minor change to

the network in terms of the discrete model can have a tremendous effect on the spatially-averaged permeability when applying the HvC method. The presence of these outliers was first detected during the visualisation of the permeability field eigenvalues (see Section 4.2.3.2). Our results suggest that a modification of the HvC method is required if anatomical vascular data is to be used. Furthermore, despite showing that the projected-PCA method for parameterising $\boldsymbol{K}$ does outperform the $\phi\boldsymbol{I}$ method for networks with clear anisotropy (see Section 4.2.1), one can see from its formulation that it too would suffer from the presence of small length, large radius vessels.

The discrete flow solution is highly sensitive to the network radii, due to the formulation of Poiseuille conductance, C. Any error in the estimated vessel radii, however, will impact both the discrete and continuum pressure solutions in a similar manner, and thus the results of this study with respect to the parameterisation process are valid. Moreover, there is strong evidence as to the efficacy of the vascular extraction and radii estimation techniques applied, such as our earlier *in silico* and phantom-based studies [49]. In addition, the transmural porosity data determined in this study is within a reasonable physiological range (Figure 4.5). Previous works have reported the total myocardial blood volume to be 12% of the tissue volume [68], with 30% of this blood volume residing in the arterial system [70]. Thus our estimate of arterial porosity of 4.8% supports the anatomically accurate nature of the vascular models used in this study. The observed transmural porosity gradient for the LV inferior and lateral regions is expected considering the known transmural gradient in flow and conductance [42, 157]. These porosity results are also indicative of a clear physiological difference between the vasculature in the septum to that of the LV free wall, as has been previously noted [98].

Our choice of N was motivated by the available experimental data with respect to changes in Coronary Vascular Resistance (CVR) distribution after various chemical or physiological actions. The data presented in Table 4.1 is not an exhaustive list, but it does indicate that two arterial compartments are sufficient to model the key vasoactive agents and their effect on CVR. These two compartments could be classified as large conduit arteries and small conduit arteries and arterioles, with a vascular scale boundary of approximately 150μm in diameter, but this can be adjusted according to the available experimental data for a specific model application. Regardless of the amount of functional data available, one must also respect the assumptions underlying Darcy's Law, thereby effectively placing a limit on the number of Darcy compartments which could be applied using an anatomical parameterisation approach as the number of observable discrete vessels is currently restricted by the imaging resolution. It is possible that we are already seeing the effects of these assumptions, and the increase in N led to a much greater decrease in rms discrepancy for the canine model than the porcine model (21% vs 2%). This disparity could be due to the canine vascular model having 56% more vessels relative to the porcine model.

With respect to the dynamic viscosity, we chose a constant value throughout, regardless of the vessel scale. This is a simplifying assumption given that suspended elements in blood, especially red blood cells, influence the apparent viscosity. Such discrete effects are contrary to the continuum fluid assumption of Newtonian flow applied within the Poiseuille flow model. Moreover, it has been shown that apparent viscosity is dependent on many factors, including vessel diameter (effects are seen at diameters $< 300\mu$m), hematocrit and blood flow velocity [114]. These dependencies are generally accepted to be caused by the mechanical interaction between red blood cells and vessel walls which

can result in the formation of a region of reduced hematocrit adjacent to the wall (called the plasma layer), and an increased concentration of red blood cells near the center of the vessel. This 'axial migration' of red blood cells causes a reduction of intravascular hematocrit (Fahraeus effect), a reduction in expected flow resistance (Fahraeus-Lindqvist effect), and a disproportionate distribution of red blood cells and plasma at bifurcations (phase separation) [112]. Useful variable expressions for the dynamic viscosity, dependent on the vessel radius, have been experimentally determined from the study of flow of red blood cell suspensions through glass capillaries [112] and mesentery networks [113, 114]. However, we believe that the use of such an expression would not significantly alter the results of our present study given the vascular scale in question, as the effect of phase separation is most prevalent in vessels of diameter less than 30μm [114]. Note that if in the future a higher resolution vascular model incorporating small arterioles becomes available, a varying form of the dynamic viscosity could easily be included within the current parameterisation process.

As a general limitation of the model, our study was focused on the static perfusion of the circulatory system only, and it did not feature any autoregulatory or mechanical components. This autoregulatory aspect in particular poses a significant challenge for the future modelling of cardiac function.

4.3.2 Clinical Implications

In a clinical setting, the 1D model component size is determined by the available data. Thus, with respect to patient-specific modelling, it was important to demonstrate that our parameterisation process is insensitive with respect to reasonable 1D model component sizes. Of particular interest are the results for

the $\tau = 0.3$mm model scenarios, as this 1D model component size is representative of clinically measurable epicardial vessels. The results of this study indicate that our process is robust with respect to changes in τ, and that $\tau = 0.3$mm produces a satisfactory rms discrepancy level in comparison to larger 1D model components. This further suggests that epicardial vascular models derived via angiography data may be adequate for our perfusion modelling needs. Moreover, the possibility of defining patient-specific permeability fields via clinically acquired porosity data has already been noted [59], and the findings of this study with regards to the $\phi \boldsymbol{I}$ permeability parameterisation adds further credence to this idea.

It is important to note that this study has not focused on the functional role played by collateral vessels, and a 'healthy' LV has been assumed throughout. While collaterals may play a more minor role in terms of porcine or human hypoperfusion, this is not the case for the canine heart, where significant collateral flow has been measured [91, 143]. However, this modelling framework can be extended to include the action of a coronary stenosis via the appropriate application of additional flux BCs on internal perfusion boundary finite elements. In this manner, one could restrict intra-compartment flow between perfusion regions, or allow flow across a regional boundary in the presence of collateral vessels. This last point shall be discussed further in Section 6.2.

Summary

The Darcy parameterisation process was applied to a series of anatomical networks with increasing complexity: *(i)* a rat capillary network, *(ii)* a single porcine arterial subnetwork, and *(iii)* entire arterial LV networks. The importance of various continuum model parameter fields was highlighted. In particular, the effect of using anatomically-derived pressure-coupling fields was shown to be the single biggest factor in reducing the rms error. Unlike the synthetic network scenario, whereby the HvC method was optimal, for the anatomical LV networks, the HvC method was sub-optimal. The porosity-scaled isotropic method was the most consistent $\boldsymbol{K}$ parameterisation method. This finding was attributed to features of anatomical vascular models not found in more simplistic, rule-based networks.

5

Darcy Model Parameterisation: Treatment of Dynamic Networks

In the previous chapters, methods for parameterising a multi-compartment static porous perfusion model have been considered. As already stated, these static perfusion models provide the correct framework for interpreting a range of experimental perfusion data. For example, both perfusion microsphere deposition studies in static domain organs such as the kidney [89] and cardiac electrophysiological optical mapping studies [35], are carried out in the absence of active contraction of the tissue and at constant perfusion pressure. However, a static perfusion model is an inappropriate framework for *in vivo* myocardial perfusion modelling, which is a dynamic process in terms of both vascular fluid flow and motion of the myocardium. Therefore, in order to accurately describe LV perfusion dynamics, the deformation of the myocardium and of the embedded vasculature should be accounted for.

The current chapter describes the development and implementation of a general method for applying a realistic cardiac deformation to the cryomicrotome-derived myocardial tissue model, and quantifies the effect of the associated

dynamic strain on the vascular model. Furthermore, it is not obvious *a priori* that the porous parameters based on the undeformed network would suffice to well-represent the properties of the associated deformed network, for example, at systole. Thus, another key aim of this chapter is to determine: *(i)* whether the porous parameters can be dynamically updated in a computationally tractable manner, *(ii)* what modifications may need to be applied to the original undeformed permeability tensors to best capture the features of the deformed network, and *(iii)* if such modifications are warranted or could one simply use the original undeformed permeability tensors regardless of the tissue deformation. A schematic of the methodological steps undertaken is provided in Figure 5.1. In Section 5.1, the importance of myocardial deformation is discussed, in particular with respect to myocardial-vessel interaction. The application of a realistic cardiac deformation to the static LV tissue model is motivated and described in Section 5.2. Various strategies for the temporal updating of the now-dynamic Darcy porous parameters are discussed in Section 5.3. Finally, these strategies are applied to the porcine anatomical arterial model and quantitatively compared in Section 5.4.

5.1 Myocardial-vessel Interaction

As described previously in Section 1.1.1, the cyclical pumping motion inherent to cardiac function has a geometric effect on the vasculature and the resulting coronary blood flow. The consequences of this mechanical coupling between the solid deformation and the vascular fluid mechanics are further elucidated in this section to motivate the current work, and the associated modelling challenges are highlighted. It is important to note, however, that this section is not a

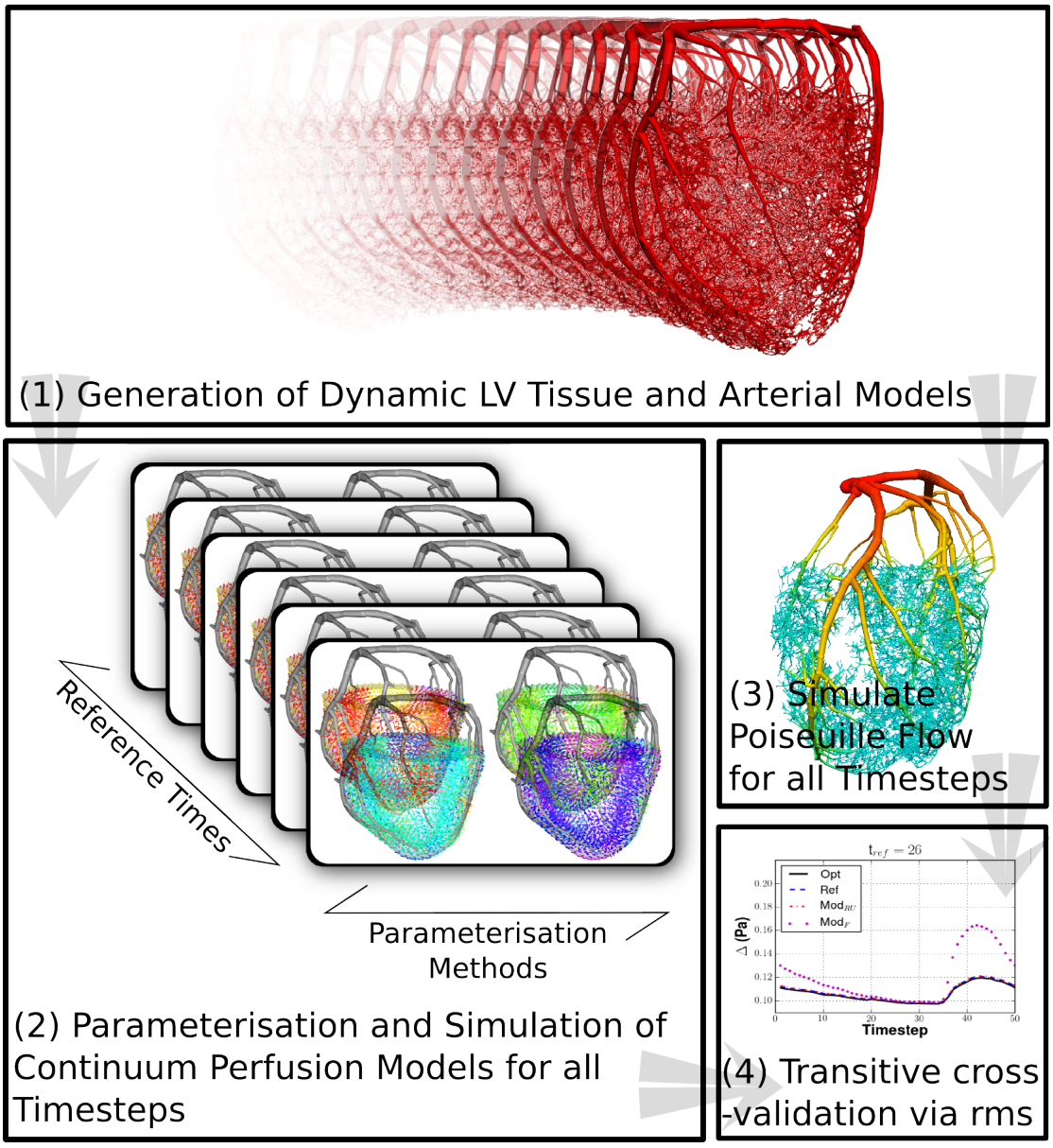


Figure 5.1: Schematic outlining the various steps of the dynamic Darcy parameterisation comparison. (1) A realistic cardiac displacement field is mapped onto the LV tissue model, and thus the embedded arterial vascular model. (2) The calculated vessel strains are used to create a set of continuum perfusion models created using a variety of parameterisation methods and reference configuration times. (3) Poiseuille pressure fields are solved for on the quasi-static discrete networks for each of the discrete timesteps representing the continuous cardiac cycle. (4) All continuum model pressure fields are quantitatively compared to the spatially-averaged Poiseuille pressure, thereby providing for a relative *in silico* cross-validation, and identification of suitable reference times and parameterisation methods.

comprehensive review of myocardial-vessel interaction and further details can be found in the literature [71, 81, 127, 155].

The coronary vasculature is embedded within the myocardium, and it follows that the volume of these elastic vessels is a function of the transmural pressure *i.e.* the difference between coronary blood pressure and Intramyocardial Pressure (IMP). The primary determinants of IMP are the transmission of ventricular pressure through the myocardial wall, and the increase in effective stiffness of the myocardium due to contracting muscle fibres. Thus, IMP increases when the myocardium contracts. The concomitant increase in coronary blood pressure decreases the longitudinal pressure gradient on the arterial side of the coronary network and increases the longitudinal pressure gradient on the venous side. This action has two major consequences: *(i)* the alteration to longitudinal pressure gradient decreases arterial blood flow and increases venous blood flow, and *(ii)* the blood volume reduction due to net outflow in high IMP areas, as well as increased transmural pressure, results in reduced vessel diameter, allowing for a positive-feedback effect on this systolic flow impediment via increased vascular resistance.

Of course, the volume change for a given vessel is likely to depend on local *myocyte* orientation with respect to the vessel orientation (see Figure 5.2 for a schematic of *myocyte* orientation throughout the LV). For this reason, the shape and pressure of the intramural vessels are likely to be influenced by local deformation and vessel orientation also. These factors have contributed to the initiation of many studies investigating the structural and functional relationship of the coronary system [47, 67, 104, 127, 133]. However, due to a lack of computational power and experimental data to parameterise their models,

most mathematical models focusing on this phenomenon have to date considered only a one-way coupling between the tissue mechanics and the coronary blood pressure. Typically, this one-way coupling only captures the effects of the tissue-generated wall stress on the elastic vessel's diameter [71, 129]. As such, this approach does not account for the mechanical effect of varying coronary perfusion pressure on the tissue's material properties *e.g.* tissue stiffening with increased coronary pressure [93, 96]. The notable exception to this statement is the study of May-Newman and McCulloch [92], which recognised the need for two-way coupling and implemented a mathematical model of the mechanics of perfused myocardium derived using homogenisation theory (see Section 1.2.2). Specifically, they modelled the perfused myocardium as a nonlinear anisotropic elastic solid with an embedded periodic structure of elastic cylindrical vessels. Two-way coupling was accounted for, as the diameter of the vessels were dependent on the perfusion pressure and the tissue stress, with the work done in altering the vascular volume contributed to the tissue's strain energy. However, their approach does rely on the assumption of periodic vessel structure and is thus most applicable to modelling the capillary bed as opposed to arterial/venous networks, which do not display such a spatially periodic structure.

In conclusion, it is desirable that a biophysical model of myocardial perfusion can incorporate two-way coupling between the coronary perfusion pressure and the myocardial deformation, while not depending on a periodic vascular structure. It is our belief that the hyperporoelastic framework is the most appropriate for this task, as it naturally satisfies these two requirements. While the parameterisation of the hyperporoelastic porous domains can follow the approach presented in Chapter 4, the form and parameterisation of the tissue

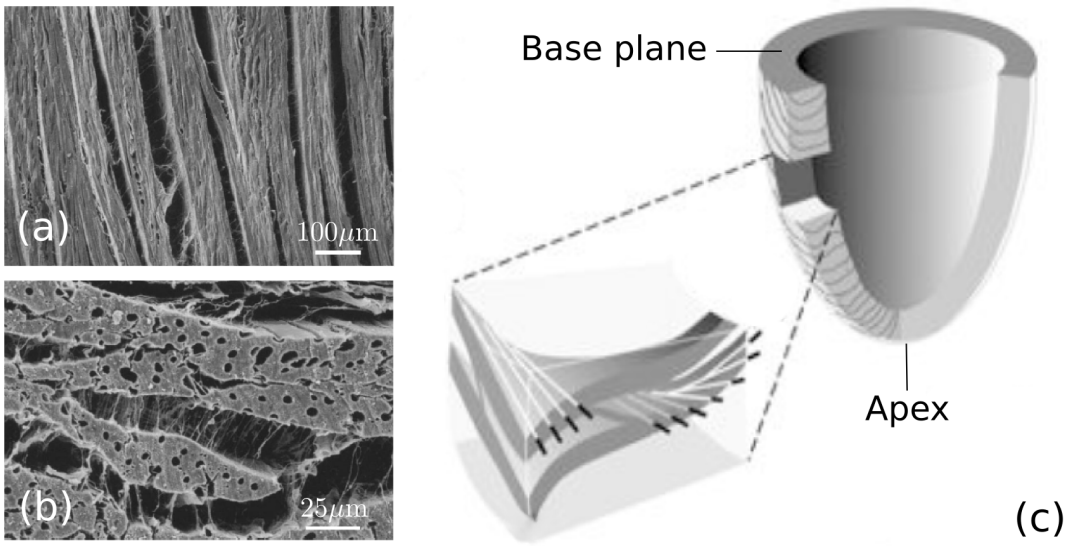


Figure 5.2: Electron Scanning Microscope images showing myocardial structure. (a) Tangential image of a fibre sheet showing the layered structure of the *myocyte*s. (b) Transverse image of a fibre sheet illustrating a high density of embedded capillary vessels. (c) Schematic of the fibre/sheet/sheet-normal material properties commonly used in electrophysiological and active-contraction modelling. Figures adapted from [84].

strain-energy function is more challenging. For this latter aspect, knowledge of the spatial distribution of vascular strain during a cardiac cycle would be extremely valuable. Particularly when one considers that dynamic structural alterations and local mechanical stresses are likely to be involved in the formation and location of *atherosclerosis* by generating or exacerbating an atherogenic mechanical environment [32]. An additional key aim of this chapter is to better characterise the typical strains experienced by the coronary arterial network.

5.2 A Deforming Myocardial Model

While cryomicrotome imaging is essential for providing the anatomical accuracy of the vascular model, the modality is inherently static (see Section 3.1). Ideally, to obtain tissue displacement data one would have acquired a cine MRI

or tagged MRI of the animal prior to commencement of the cryomicrotome experimental protocol. However, such data was not acquired for any of the animals from which the cryomicrotome data stacks were extracted.

Even if such data was available, it would require significant post-processing to calculate a continuous tissue displacement field given: *(i)* the spatiotemporal limitations of tagged and cine MRI *e.g.* a typical animal experimental protocol for cine MRI has a spatial resolution of $1.5 \times 1.5 \times 5$mm at 40 timeframes per cardiac cycle [16] which is better than the spatiotemporal resolution for tagged MRI data ($3.4 \times 3.4 \times 7.7$mm at 30ms intervals [17]), and *(ii)* that cine MRI only reveals incomplete surface displacements. Thus, for the currently available anatomical vascular/tissue models, there is a need to apply an externally-sourced cardiac cycle deformation.

To simulate a realistic cardiac deformation for a particular tissue model is a non-trivial task however, given the nature of tuning parametrically-sensitive, coupled components. For example, the biophysically based patient-specific coupled electromechanics heart model of Niederer et al. [103] features 16 parameters involved in the passive tissue model, fibre orientation, active contraction and Windkessel LV pressure components.

Thus, it was decided to apply a previously-computed tissue displacement field, obtained from an incompressible hyperelastic model of an actively contracting porcine LV geometry, to the porcine cryomicrotome-derived tissue model. This step requires a method to map tissue model displacement, that can robustly project the computed tissue displacement onto the desired target cardiac geometry. Furthermore, this technique should be as general as possible with the aim that, if in the eventuality of a future study where dynamic data was acquired,

the same displacement mapping pipeline could still be applied.

The remainder of this section details the work done to complete step 1 of the schematic shown in Figure 5.1, *i.e.* the generation of dynamic LV tissue and arterial models.

5.2.1 Displacement Mapping Method

As outlined above, we wish to apply a realistic cardiac cycle deformation to the static target cryomicrotome-derived tissue mesh which consists of 24,793 linear Lagrange tetrahedral elements. This displacement will be mapped from a left ventricular geometry consisting of 972 quadratic hexahedral elements. Thus the challenge is to map the tissue displacement from the dynamic displacement mesh of one element type and location, onto the static cryomicrotome mesh of a different element type and location.

Firstly, a template Cubic Hermite (CH) mesh is fitted to both the cryomicrotome mesh and the displacement mesh in its initial configuration. This is done using the same automatic tool as was used to create the cryomicrotome mesh in the first instance (see Section 3.1 of this thesis, and [77]). The topology of the CH mesh used in our study contained eight elements in the apical-base direction, nine elements in the circumferential direction, and a single radial element. The apical geometry of our anatomically-based tissue models was sufficient to ensure a consistent CH mesh alignment during the fitting process *i.e.* the lateral free walls correctly aligned. This latter point is important, as the automatic CH mesh fitting software relies on obtaining a quality affine transformation registration to the target mesh.

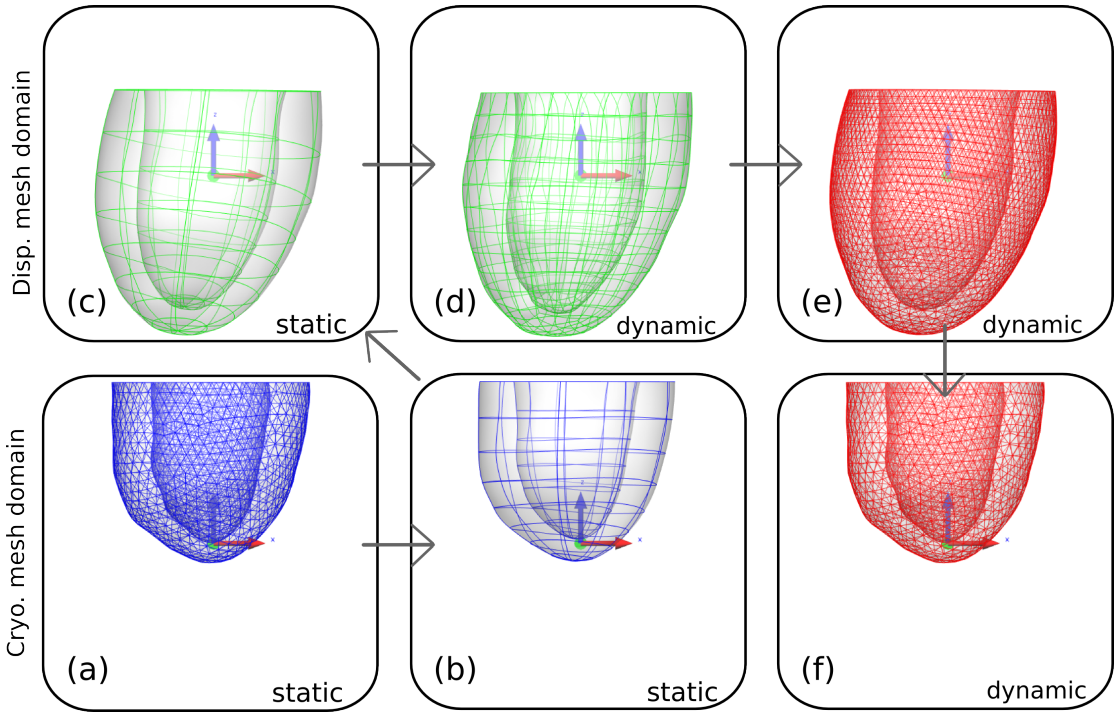


Figure 5.3: The tissue model displacement mapping pipeline. (a) Cryomicrotome-derived static tetrahedral mesh. (d) The hexahedral displacement mesh geometry at the initial timestep. The same cubic Hermite template mesh was fitted to each of the target geometries. (b) The cubic Hermite mesh fitted to the static mesh in (a). (c) The cubic Hermite mesh fitted to the displacement mesh geometry at the initial timestep. These fitted Hermite meshes allow for a bijection between any point of the cryomicrotome-derived mesh and the displacement mesh.

As a result of this alignment process, there exists a bijection between the cryomicrotome mesh and the displacement mesh. To demonstrate this, consider any point, denoted p_c, from the cryomicrotome mesh. There exists a unique fitted cubic Hermite local ξ-space coordinate for p_c (if p_c lies outside the fitted CH mesh, then the local element is taken to be that which contains the point closest to p_c). In almost the reverse of this step, one can convert from this local ξ-space coordinate back into Cartesian space, but now using the nodal coordinates of the displacement mesh fitted CH mesh. This process, denoted the Cartesian-ξ-Cartesian conversion method, has now mapped the cryomicrotome mesh point p_c into a displacement mesh point, denoted p_d. By considering the same pro-

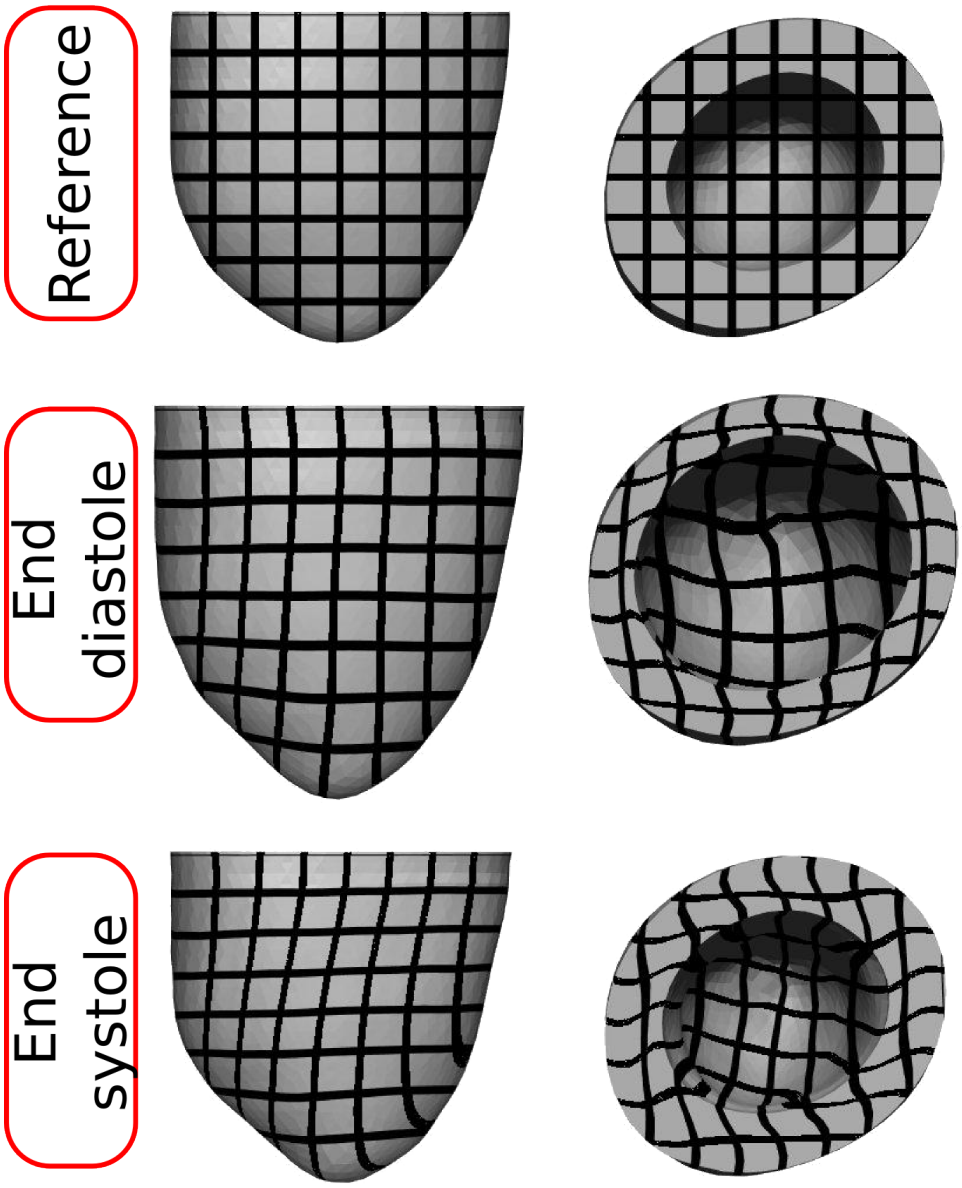


Figure 5.4: The simulated cardiac cycle deformation for the cryomicrotome-derived tissue model is illustrated via contours of the reference state coordinate field to produce a 'tagged MRI' image at different stages of the cardiac cycle. The top row displays the undeformed, or reference, configuration. The middle row displays the deformation at 'end diastole', which is taken to be the timestep when apical rotation commences. Note the apical-base elongation and the cavity volume increase. The bottom row displays the deformation at 'end systole', which is taken to be the timestep when apical rotation has reached its stationary point, before reverting to its unrotated reference state. Significant apical rotation and a shear mode of deformation are visible on the endocardial surface.

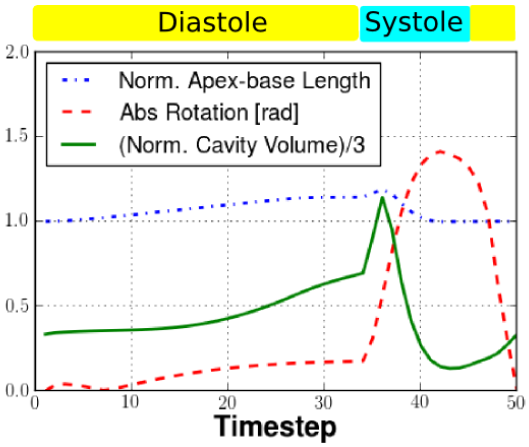


Figure 5.5: Data fields over time for the deforming myocardial tissue model. Fields are normalised with respect to their value at the initial timestep. One can see that the normalised LV apex-base length and cavity volume peak at timestep 36, which is deemed to be the end of diastole. The absolute rotation of the apex peaks at timestep 43, which is deemed to be end systole.

cess in reverse, one can map p_d onto p_c (Figure 5.3). If p_c were a cryomicrotome mesh node, one can determine its equivalent position in the displacement mesh and its displacement at time t by simply converting from the local ξ-space coordinate back into Cartesian space using the displacement mesh nodal coordinates at time t. Finally, to account for the scenario of the cryomicrotome and displacement meshes being in a different location or of a different scale, one must transform this displacement by the affine transformation that best registers the displacement mesh to the cryomicrotome mesh (equivalently this affine transformation could be applied to the displacement mesh first, before the template CH meshes are fitted). This registration was determined using the open-source Sheffield image registration toolkit (ShIRT) software [1].

The originally static cryomicrotome mesh now has a dynamic aspect via the spatial association of a modelled cardiac cycle deformation. The realism of the motion can be quantitatively assessed using the simulated tagged MRI images of Figure 5.4, providing an indication of the epicardial and endocardial strains, area changes, and shear stress. In more detail, the relative apex-base length,

[1] http://www.doc.ic.ac.uk/~dr/software/

apical rotation, and cavity volume changes are displayed in Figure 5.5. Note that for the purposes of timestep quantification the simulated cardiac cycle is split into 50 equal timesteps.

5.2.2 Deformation Gradient Tensor

The deformation of the myocardium is typically simulated using the Lagrangian equations of motion for a continuum, elastic body undergoing a finite deformation. For the purposes of the research conducted in this chapter, the deformation gradient tensor is introduced below. For a more complete coverage of continuum-based kinematics, the reader is referred to the relevant literature [10, 52, 87].

In describing the dynamic response of elastic bodies under external forces, a reference configuration $B \subset \mathbb{R}^3$ of the body at the reference time t_0 is selected, with the boundary of B being denoted as ∂B. The coordinates of points $\boldsymbol{X} \in B$ are used to identify material particles throughout the subsequent motion of the body, which is described by the displacement mapping

$$\boldsymbol{x}(t) = \psi(\boldsymbol{X}, t), \ \boldsymbol{X} \in B. \tag{5.2.1}$$

Thus, $\boldsymbol{x}$ is the location of material particle $\boldsymbol{X}$ at time t (see Figure 5.6 for a schematic of a body B undergoing a displacement ψ). In the event of a Dirichlet displacement boundary, denoted Γ_D, then the deformation mapping is subject to essential boundary conditions on the displacement boundary $\Gamma_D \subset \partial B$.

The local deformation of infinitesimal material neighbourhoods is described by

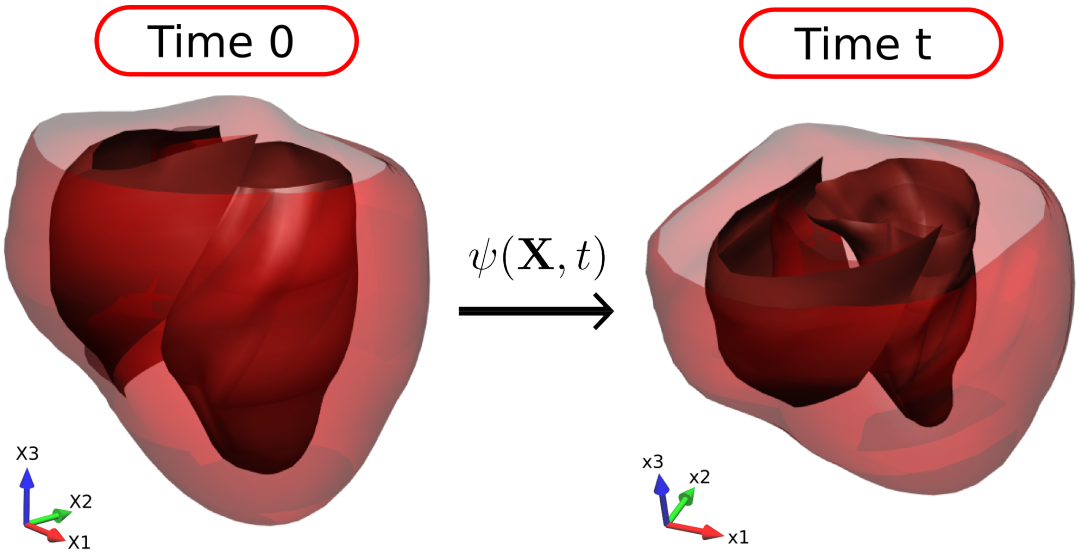


Figure 5.6: Schematic illustrating the general motion of a deformable solid body. The material particles are labeled by the coordinates $\boldsymbol{X}$ with respect to the Cartesian basis at time 0.

the deformation gradient

$$F_{ij} = \frac{\partial \psi_i}{\partial X_j}(\boldsymbol{X}, t) = \frac{\partial x_i}{\partial X_j}, \quad i, j = 1, 2, 3. \tag{5.2.2}$$

The scalar function

$$J = det(\boldsymbol{F}(\boldsymbol{X}, t)) \tag{5.2.3}$$

is the Jacobian of the deformation, which links the elemental material volume dV to the elemental spatial volume dv via $dv = JdV$. As the deformation gradient tensor $\boldsymbol{F}$ describes the relative spatial position of neighbouring particles after deformation in terms of their relative material position before deformation, it is thus central also to strain.

5.2.3 Treatment of the Vascular Model

The challenge presented by considering vascular models embedded within a deformable medium has been treated in a variety of manners in the literature. In the paper of Vankan et al. [147], a multi-compartment poroelastic model of blood perfused *contracting* skeletal muscle is presented. Due to a lack of discrete vascular data however, the permeabilities used were all assumed to be isotropic and constant. Similarly, in the multi-compartment porous models of Huyghe et al. [58] and Vankan et al. [149], the existence of an underlying idealised network is assumed, although no actual discrete network is referenced. Once more, due to the lack of an explicit vascular model, their approach was to assume *(i)* an isotropic permeability, and *(i)* that all coronary vessels change their volume at constant length. Under these assumptions, the volume of a vessel, v, is related to its radius by

$$v = \pi r^2 l \implies v \propto r^2. \tag{5.2.4}$$

Further guided by Poiseuille's law, one can see that the Poiseuille conductance, C, is related to the vessel volume by

$$C = \frac{\pi r^4}{8\mu l} \implies C \propto (r^2)^2 \implies C \propto v^2. \tag{5.2.5}$$

Thus, the permeability of the medium was scaled according to the square of the change in intramyocardial blood volume.

Given the dearth of experimental data at the time, the simplifying assumptions made were reasonable and justified. These papers were also primarily focused on model development and qualitative results rather than biophysical fidelity.

Nonetheless, their assumptions are debatable with regards to our application, given the large deformation that the heart is known to undergo in a typical heart beat [88]. This is especially true for the scale of vessels featured in the arterial vascular models available (see Figure 3.7). This thesis aims to build upon their pioneering work by applying modern data-acquisition and parameterisation methods. We have already described how the advent of the cryomicrotome imaging modality now provides anatomically-based arterial vascular and myocardial models (see Chapter 3). Furthermore, a method for applying a simulated cardiac cycle deformation to the static tissue models has been presented in Section 5.2.1. We now describe a similar method for projecting the tissue model deformation onto the embedded vascular model.

Firstly, the vascular model nodes are considered in two groups: those with a z-coordinate less than or equal to the LV tissue model base plane; and the remaining vascular model nodes. The application of the displacement field to the former group is conducted similarly to the displacement mapping between the two tissue models as described in Section 5.2.1. Each vascular model node is mapped to its cryomicrotome mesh ξ-coordinate, and this ξ-coordinate is

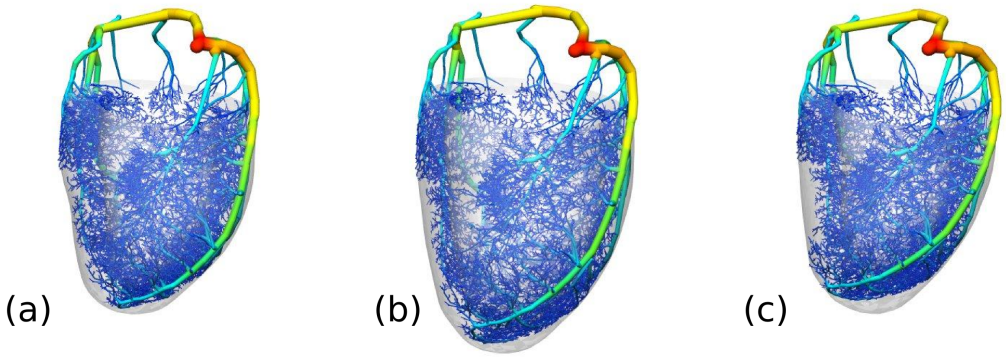


Figure 5.7: The deforming tissue model with the embedded vascular model, displayed at timesteps 1 (a), 36 (b) & 43 (c) corresponding to the reference, end diastole, and end systole configuration states.

mapped back into the Cartesian space using the mesh nodes at their deformed coordinates for each time step. For the latter group however, an extra step must be taken given that these vascular model nodes can often lie a significant distance from a cryomicrotome mesh element (6.6 ± 7.1mm (mean$\pm$sd) to the closest mesh node). This distance from their closest element renders the displacement mapping via the Cartesian-ξ-Cartesian conversion method prone to large errors. To address this issue, the vascular model nodes are projected onto the same xy-plane as the LV tissue model base plane. This greatly reduces the distance from the vascular model node location to its closest cryomicrotome mesh element (1.2 ± 1.3mm (mean$\pm$sd) to the closest mesh node). The Cartesian-ξ-Cartesian conversion method is now applied to obtain the nodal displacements in the x and y dimensions, before the nodal z-coordinates are reverted back to their original values. Note that all results presented in this thesis consider the strains for the former vascular nodal group only, due to the lack of an atrial tissue component and the requirement for this z-coordinate projection.

While this method results in a reasonable estimate of deformation *in terms of strain* for the vascular model, it remains to decide on how the vessel radii should be updated along with the calculated strain. To leave the vessel radii unchanged throughout the cardiac cycle would result in effectively instantaneous and significant Arterial Blood Volume (ABV) changes given the rapid nature of the cardiac cycle. In fact, by assuming a heart rate of 95bpm and a constant radius field given by the original cryomicrotome analysis, the peak ABV influx was calculated to be $6400\text{mm}^3 s^{-1}$ (Figure 5.8). A constant radius assumption is also contrary to experimental evidence which has shown that the radii of proximal epicardial arteries are a function of coronary perfusion pressure, and thus vary with time. For example, the study of Kelle et al. [74] used 3T

MRI measurements to calculate an average increase in proximal arterial radius of 5.5% from end-diastole to end-systole, and the study of Kanatsuka et al. [64] calculated a value of 1.1% for the same metric using an intravital microscope. It is interesting to note that a similar study by Yada et al. [160] found that cardiac contraction decreased the diameter of both subendocardial arterioles and venules by approximately 20%, revealing the phasic nature of arterial diameter changes.

Thus, one can conclude that arterial radius is likely to be dependent on a host of extra factors, such as transmural location and effect of IMP, LV pressure, local myocardial structure, vessel scale, age, health *etc.* Given these complications and the dearth of transmural experimental data on dynamic vessel radii, for the purposes of this study it was decided that a reasonable first approximation was to assume a quasi-static framework, whereby individual vessel fluid volume was conserved between mesh deformation timesteps. Thus for a vessel with radius r_t and length l_t at timestep t, r_t can be determined via

$$r_t = \sqrt{\frac{(r_0)^2 l_0}{l_t}}. \tag{5.2.6}$$

Using this relation, the change in radius from end-diastole to end-systole was calculated to be $-1.43 \pm 8.4\%$ (mean$\pm$SD) which is of the same order of magnitude as the experimentally measured values reported above.

To the best of our knowledge, this is the first example of a high-resolution anatomical vascular model coupled to a realistic, deforming cardiac geometry.

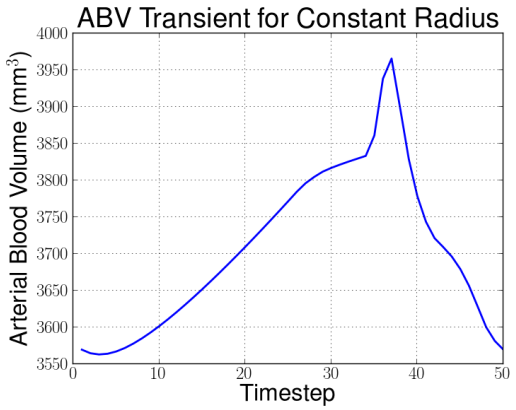


Figure 5.8: Graph of total Arterial Blood Volume (ABV) versus timestep with dynamic vessel strains and constant radii values as determined from the cryomicrotome analysis.

5.3 Dynamic Parameterisation Methods

This section is related to step 2 of the schematic shown in Figure 5.1, *i.e.* the parameterisation and pressure simulation of our continuum perfusion models. Recall that a key aim of this chapter is to determine whether one can dynamically update the porous parameters in a computationally tractable manner. In other words, is it necessary to modify the permeability tensor fields within our multi-compartment perfusion model given a temporal deformation, and if so, what is a suitable method of modifying the parameters? To address this issue, we now consider four methods for parameterising a dynamic perfusion model, taking as inputs: *(i)* the reference configuration Darcy porous domain parameters as calculated in Chapter 3, and *(ii)* the deformation gradient tensor field, $\boldsymbol{F}$. Note that in a hyperporoelastic simulation, $\boldsymbol{F}$ will have to be determined regardless of the permeability parameter updating method chosen as it is required to calculate the pointwise residual stresses for the large deformation mechanics solution.

Importantly, the reference configuration pressure-coupling fields are kept constant throughout for the first three of the four methods described below (for

discussion of this point see Section 5.5).

The $\boldsymbol{K}$ updating methods considered are:

- **"Ref" Method**

  The reference configuration permeability tensor fields are kept constant throughout all timesteps *i.e.*

  $$\boldsymbol{K}_t = \boldsymbol{K}_0. \tag{5.3.1}$$

  Note that there is no additional computational cost to a dynamic perfusion simulation using this method

- **"Mod$_F$" Method**

  This method uses the deformation gradient $\boldsymbol{F}$ to deform the flow directions and simultaneously alter the flow strengths. Specifically, $\boldsymbol{K}$ is first eigendecomposed [2] via

  $$\boldsymbol{K} = VDV^{-1}, \tag{5.3.2}$$

  where V is the square matrix whose i^{th} column is the i^{th} eigenvector v_i of $\boldsymbol{K}$, and D is the diagonal matrix whose diagonal elements are the corresponding eigenvalues, *i.e.* , $D_{ii} = \lambda_i$ and $\boldsymbol{K}\lambda_i = \lambda_i v_i$. Formalised in this manner, one can see that the eigenvalues λ_i correspond to the magnitudes of the principal fluxes along the principal flow directions *i.e.* the eigenvectors v_i. One needs to know the tissue strain along these flow directions in order to sensibly update these fluxes. We can thus apply the *polar decomposition* of $\boldsymbol{F}$ (see Section 4.6 of Bonet and Wood [10]), whereby $\boldsymbol{F}$ is expressed as the product of a rotation tensor $\boldsymbol{R}$ times a stretch tensor

[2] Note that this eigendecomposition exists as $\boldsymbol{K}$ is SPD by design.

$\boldsymbol{U}$, *i.e.*

$$\boldsymbol{F} = \boldsymbol{R}\boldsymbol{U}. \tag{5.3.3}$$

In practice, one generally calculates $\boldsymbol{U}$ from the right Cauchy-Green tensor $\boldsymbol{C}_{CG}$ via

$$\boldsymbol{C}_{CG} = \boldsymbol{F}^T\boldsymbol{F} = \boldsymbol{U}^2, \tag{5.3.4}$$

where $\boldsymbol{F}^T$ denotes the application of the matrix transpose operator to the matrix $\boldsymbol{F}$, thereby determining the stretch that occurs in the principal flow directions. If one imagines a vessel oriented along the i^{th} eigenvector, it is possible to calculate its deformed length, l, as a function of its reference length l_0 and $\boldsymbol{U}$ via

$$l = l_0 \, |\boldsymbol{U} \, v_i|, \tag{5.3.5}$$

where $|\boldsymbol{a}|$ is the length of the vector $\boldsymbol{a}$. Thus, the Poiseuille conductance at the timestep t, denoted C_t, is given by

$$\begin{aligned} C_t &= \frac{\pi}{8\mu}\frac{r^4}{l} && (5.3.6)\\ &= \frac{\pi}{8\mu} r_0^4 \left(\frac{l_0}{l}\right)^2 \frac{1}{l} && (5.3.7)\\ &= \frac{\pi}{8\mu}\frac{r_0^4}{l_0} \left(\frac{l_0}{l}\right)^3 && (5.3.8)\\ &= C_0 \left(\frac{l_0}{l}\right)^3, && (5.3.9) \end{aligned}$$

where l/l_0 is the vessel stretch ratio (Figure 5.9) and the constant fluid mass assumption has been applied (see Eq. (5.2.6)). This ratio of the dynamic Poiseuille conductance to the reference Poiseuille conductance is extrapolated to the related measure of directional conductance in the per-

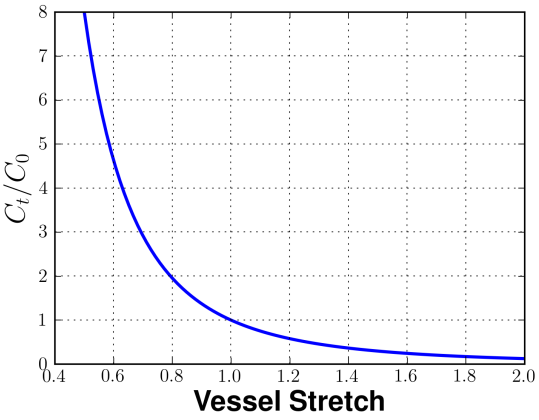


Figure 5.9: The ratio of initial Poiseuille conductance, C_0 to the current timestep Poiseuille conductance C_t is graphed for various values of vessel stretch. This relationship was derived by assuming a constant vessel fluid volume.

fusion model *i.e.* one can update the flux magnitudes as a function of $\boldsymbol{F}$ via

$$\lambda_{i,t} = \lambda_{i,0} \left(\frac{1}{|\boldsymbol{U}\, v_i|} \right)^3. \tag{5.3.10}$$

Of course, a given deformation may not only alter the flux magnitudes but it could also alter the flow directions. For the Mod_F method, this is done by taking the product of the eigenvector matrix with the deformation gradient tensor itself *i.e.*

$$\boldsymbol{K}_t = (\boldsymbol{F}V) D_t (\boldsymbol{F}V)^{-1}, \tag{5.3.11}$$

where $(D_t)_{ii} = \lambda_{i,t}$.

- **"Mod_R" Method**

  This method is similar to the Mod_F method above, except that rather than modifying the principal flow directions by $\boldsymbol{F}$ directly, they are instead operated on by the rotation tensor $\boldsymbol{R}$ *i.e.*

$$\boldsymbol{K}_t = (\boldsymbol{R}V) D_t (\boldsymbol{R}V)^{-1}. \tag{5.3.12}$$

The only extra computational cost required is the calculation of $\boldsymbol{R}$ which involves the application of two linear algebraic operations as can be seen by rearranging Eq. (5.3.3) into

$$\boldsymbol{R} = \boldsymbol{F}\boldsymbol{U}^{-1}. \tag{5.3.13}$$

- **"Opt" Method**

  The deformed tissue and vascular models are treated as a entirely new static perfusion model. The Darcy porous domain parameters are derived and optimised as per Chapter 4 at each timestep. This includes the permeabilities and, unlike the previous three methods, also the pressure-coupling fields. In this case, the HvC $\boldsymbol{K}$ parameterisation method is applied to provide fully anisotropic permeability fields. The use of this method would add a significant extra computational burden upon a dynamic perfusion model, significantly compromising our goal of a clinically-relevant solution time. However for the purposes of this research it effectively acts as the 'gold standard' of Darcy porous domain parameterisation, against which the three previous temporal updating methods can be compared.

5.3.1 Choice of Reference State

The reference configuration, $\boldsymbol{X}$, used for continuum model simulations within the field of large deformation tissue mechanics is a challenging and sometimes controversial issue. The choice of $\boldsymbol{X}$ significantly effects the model simulation via its coupling to the deformation gradient tensor (see Eq. (5.2.2)) which fea-

tures in the stress-strain relation (see Chapter 6 of Bonet and Wood [10]). The crux of the challenge is that one can rarely determine the true reference configuration of a biological tissue. For example, the *in vivo* heart is constantly in a 'loaded' condition *e.g.* via exterior forces applied by breathing motion, anatomical displacement constraints (the heart normally resides within the *pericardium* and is attached physically to the body via the aorta, vena cava and several other pulmonary arteries/veins) and the pressure exerted by the pumped blood on the myocardium. Compounding these factors is the whole issue of *residual stress*, which is thought to arise from tissue growth and remodelling [119].

With respect to our continuum perfusion model however, the choice of $\boldsymbol{X}$ affects the temporal $\boldsymbol{K}$ values only, as seen in the derivation of the updated permeabilities presented above. The temporal $\boldsymbol{K}$ values depend on the vessel strain which in turn depends on the initial vessel length (or equivalently the initial Poiseuille conductance assigned to each vessel). Arguably, a sensible approach is to choose one of the timesteps of the cardiac cycle as the reference timestep, and define the vessel strain from this initial, or reference, length. Even by restricting the choice to this finite set of 50 timesteps, one still cannot know which timestep to take as the reference, denoted $\boldsymbol{t_{ref}}$, or how sensitive the results will be to this choice. For this reason, it was decided to select several timesteps as the reference timestep and to analyse the results of the various dynamic parameterisation methods for each value of $\boldsymbol{t_{ref}}$.

The set of timesteps chosen as $\boldsymbol{t_{ref}}$, and the reasons for their selection, are now presented:

- $\boldsymbol{t_{ref}} = 1$

  This is the timestep of zero mesh displacement, and approximately the be-

ginning of diastole (see Figure 5.5). Thus the tissue geometry, and vascular lengths and radii, are all as extracted from the original cryomicrotome data set.

- $t_{ref} = 10$

  This is the timestep of *least strain deviation* for all vessels over all timesteps. Strain deviation for a vessel was calculated by determining the maximum and minimum vessel length over the course of the cardiac cycle. This information was used to define a mean length for the vessel, and the vessel strain deviation was defined to be the sum of the absolute difference between the vessel's length at time t, and its mean length, over all discrete timesteps t.

- $t_{ref} = 18$

  This is a representative mid-diastolic timestep.

- $t_{ref} = 26$

  This timestep was chosen in a retrospective manner. It is the timestep that resulted in the least porosity-weighted pressure rms discrepancy when comparing the continuum model result using the 'Ref' dynamic parameterisation method against the spatially-averaged Poiseuille pressure field.

- $t_{ref} = 36$

  This is the end-diastole timestep.

- $t_{ref} = 43$

  This is the end-systole timestep.

5.4 Results

Vascular model strain data is first presented in Section 5.4.1. This serves two purposes: *(i)* independent analysis of the simulated yet realistic vascular strains is important in its own right, as there currently exists no method of obtaining a similar data set from either direct or indirect visualisation methods or imaging modalities; and *(ii)* by equation Eq. (5.3.10), one can see that the strain is directly related to the temporal state of the Darcy permeability fields, and thus in general, regions of tissue that experience greater vessel strain should be expected to experience greater alterations to the local permeability.

The rms discrepancy results for the varying updating methods and reference timesteps are presented in Section 5.4.2.

5.4.1 Temporal Strain Measures

It is now possible to simulate the length of any vessel embedded within the LV tissue model throughout the cardiac cycle. As outlined in Section 5.4.2, the definition of a standard strain measure requires a reference timestep from which the vessel compression or expansion can be calculated. For example, in Figure 5.10, the vascular model strain is quantified at both the end-diastolic and end-systolic timesteps, assuming $\boldsymbol{t_{ref}} = 1$, with the corresponding strain histograms shown in Figure 5.11.

Given the myriad of issues surrounding the choice of the reference timestep (see Section 5.3.1), it would be valuable to produce a $\boldsymbol{t_{ref}}$ independent measure of vascular motion. To this end, in Figure 5.12(A), histograms of the maximum vessel lengths (l_{max}), minimum vessel lengths (l_{min}) and the vessel length range

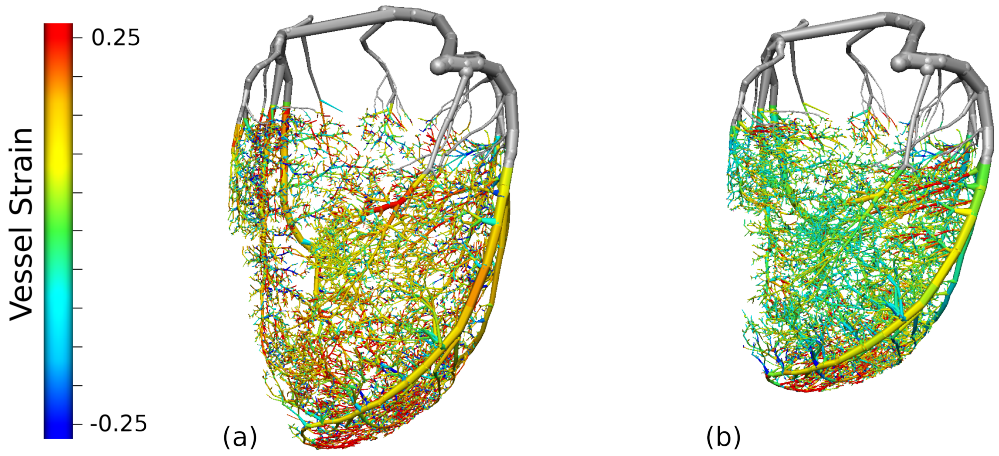


Figure 5.10: The vessel strain throughout the LV tissue model at end-diastole (a) and end-systole (b). These strains were calculated with respect to the reference timestep $t_{ref} = 1$. Vessel extension is clearly seen throughout the end-diastolic stage, whereas the majority of vessels are compressed during systole. An exception to this can be seen at the apex of (b), where the significant tissue rotation is stretching the local vessels. The silver vessels have vascular model nodes above the tissue model base plane, but only accurate displacements can be guaranteed for the vessels within the tissue model. Hence, their strains are not used in any calculations or visualised in this figure.

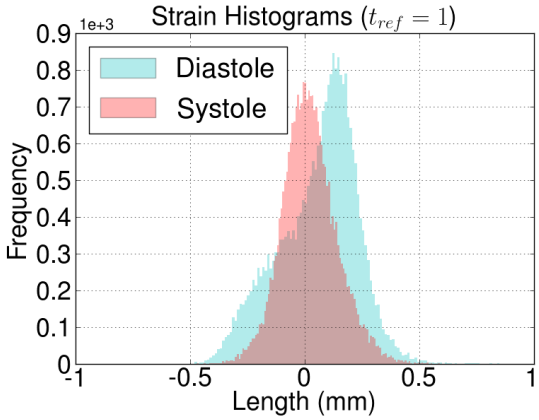


Figure 5.11: Histograms of vessel strain for diastole ($t = 36$) and systole ($t = 43$) using $t_{ref} = 1$. The diastolic and systolic strains correspond to those visualised in Figure 5.10(a) and Figure 5.10(b) respectively.

($\triangle l = l_{max} - l_{min}$) are displayed. This latter histogram is of particular importance as it reveals the expected physiological range of vascular deformation. Specifically, 95% of vessels have a range $<$ 0.45mm (Figure 5.12(B)) with an average range of approximately 0.17mm, which is significant given that it represents 21% (27%) of the average l_{max} (l_{min}) value.

Of course, considering the range of vessel deformation in this manner does not

reveal any possible underlying relation with vessel scale. To investigate this issue further, one can assign to each vessel a normalised strain, l_{norm}, via

$$l_{norm} = \frac{\triangle l}{0.5(l_{max} + l_{min})}. \tag{5.4.1}$$

A scatter plot of the vessel radius versus normalised strain can be seen in Figure 5.13(A), from which it can be observed that the variance of l_{norm} is negatively correlated with vessel radius. This suggests that smaller scale vessels are more likely to experience a greater deformation relative to their larger scale counter-parts. Furthermore, one might reasonably suspect that the spatial distribution of l_{norm} is not homogeneous. An inspection of the normalised strain field displayed on the vascular model geometry in Figure 5.13(B) allows for a global assessment of regional differences. For example, the apical region can be seen to feature a higher concentration of relatively large l_{norm} vessels.

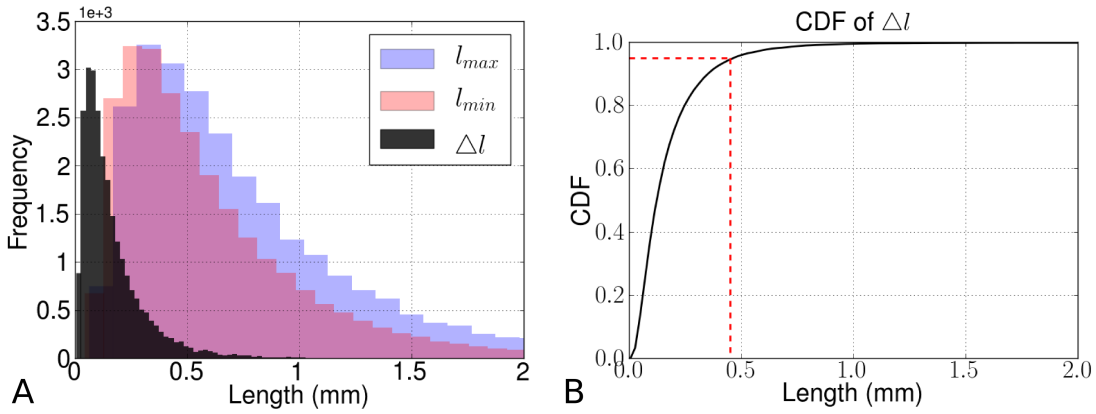


Figure 5.12: (A) Histograms of the maximum lengths (l_{max}), the minimum lengths (l_{min}) and the range ($\triangle l = l_{max} - l_{min}$) attained by tissue embedded vessels. (B) CDF for the $\triangle l$ data, where it can be seen that 95% of vessels have a range < 0.45mm.

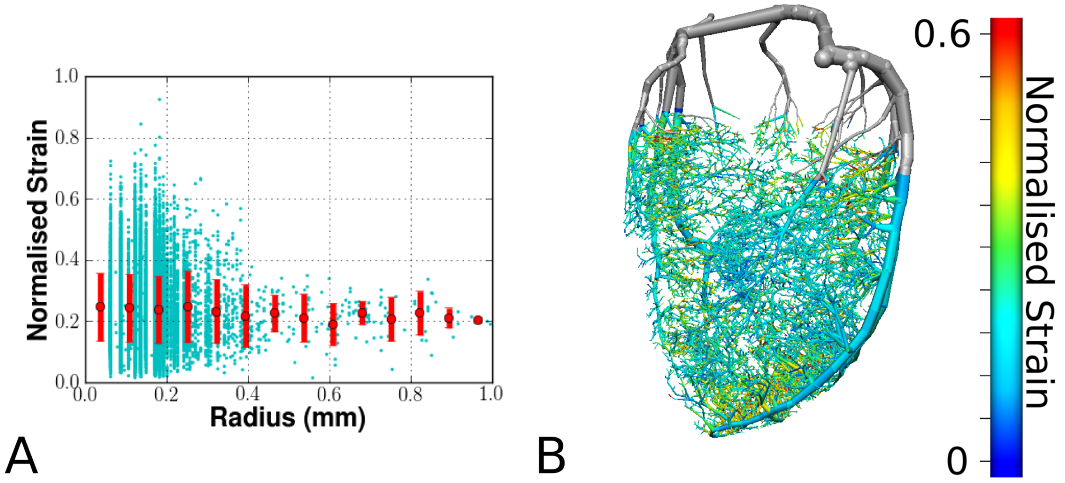


Figure 5.13: (A) Scatter plot revealing the relationship between normalised strain and vessel scale. Vessels were grouped into 14 uniform bins by radius from which the normalised strain mean±S.D. values were calculated and overlaid in red. (B) The role that spatial distribution plays within the deformation of vessels can also be investigated. Here, the normalised strain is shown on the zero displacement geometry.

5.4.2 Temporal *K* Modification

For consistency with our earlier results of Section 4.2, the various methods of dynamic $\boldsymbol{K}$ parameterisation are compared via a porosity-weighted pressure rms discrepancy, denoted $\triangle$, to the spatially-averaged Poiseuille pressure (see Eq. (2.4.1), and step 3 of the schematic shown in Figure 5.1). The discrete model was solved as previously described (Section 4.1.1) with the only difference being that the network topology itself is now a function of time. Although the biophysical situation being modelled is clearly a continuously varying process, it is treated as a discrete set of timesteps and the solutions are independently calculated in a quasi-static manner. For the continuum model, values of $N = 2$ and $\tau = 0.25$mm were applied, along with appropriate BCs as described in Chapter 4.

The rms discrepancy results for the four dynamic $\boldsymbol{K}$ parameterisation methods

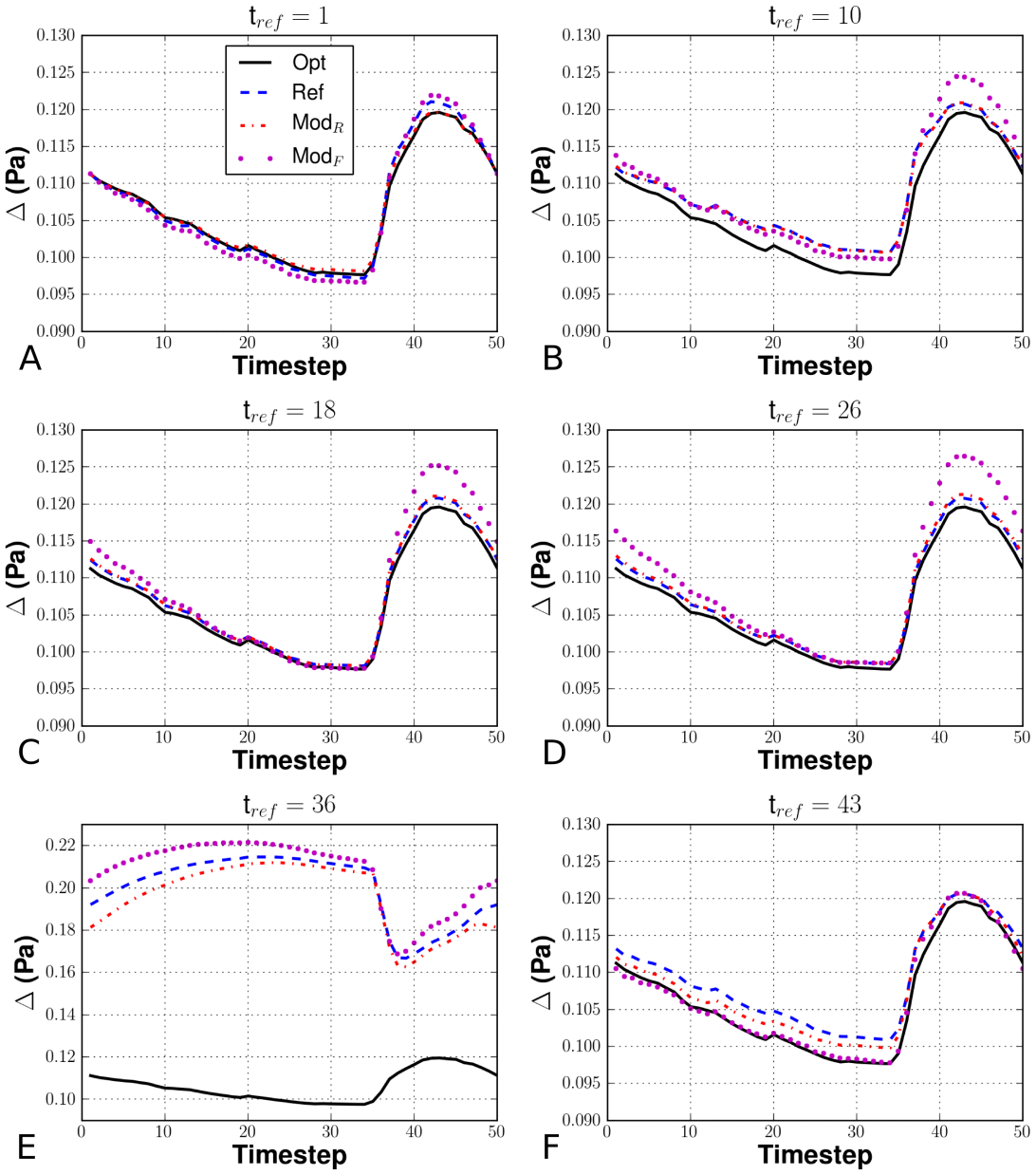


Figure 5.14: The rms error, △, for the four dynamic $\boldsymbol{K}$ parameterisation methods at six different reference timesteps, $\boldsymbol{t_{ref}}$. The legend used in (A) applies to all six sub-figures. Note the increased y-axis dimension for sub-figure (E).

for the six selected $\boldsymbol{t_{ref}}$ times are presented in Figure 5.14 (see also step 4 of Figure 5.1). Firstly, it is observed that all updating strategies coincide at the timestep value $\boldsymbol{t_{ref}}$. This is because at this time, the deformation gradient field is trivial, *i.e.* $\boldsymbol{F} = \boldsymbol{I}$, and thus the methods should produce the same Darcy

permeability field and hence the same continuum pressure field. Secondly, the methods 'Opt', 'Ref' and 'Mod$_R$' produce similar $\triangle$ transients for almost all the $\boldsymbol{t_{ref}}$ tested, with the major exception of $\boldsymbol{t_{ref}} = 36$ whereby the $\triangle$ transients are significantly larger (Figure 5.14(E)).

To discern the more subtle differences amongst the methods, the transients are quantified via subtracting the integral of the re-parameterised method 'Opt' transient from the integral of the updating strategy transient. Specifically, the total *relative* error, $\triangle_T$, is given by

$$\triangle_T(M) = \int_{beat} (\triangle M - \triangle Opt)\, dt, \tag{5.4.2}$$

where M is a temporal parameterisation method, and *beat* is the set of 50 discrete timesteps. These results are collated in Table 5.1. Three findings are evident from these data: *(i)* $\boldsymbol{t_{ref}} = 1$ produces the minimum $\triangle_T$, whether considering the parameterisation methods individually or in total, *(ii)* considering all $\boldsymbol{t_{ref}}$ values, the Mod_R parameterisation method is the optimal of the three, and *(iii)* considering only the diastolic $\boldsymbol{t_{ref}}$ values (*i.e.* $\boldsymbol{t_{ref}} = 1, 10, 18, \&26$), then the Ref method is optimal. Finally, upon visual inspection of the diastolic $\boldsymbol{t_{ref}}$ transients, one can see the larger $\triangle$ values are generated during the main rotational time period (see Figure 5.5). This is particularly evident for the 'Mod_F' method.

Full analysis of these findings are presented in the forthcoming Section 5.5.2.

t_{ref}	$\triangle_T(Ref)$	$\triangle_T(Mod_R)$	$\triangle_T(Mod_F)$	$\sum\triangle_T$
1	0.004745	0.011712	-0.013643	0.002814
10	0.112709	0.111361	0.133049	0.357119
18	0.038849	0.043599	0.099688	0.182136
26	0.046535	0.057456	0.149551	0.253542
36	4.687064	4.454350	5.034851	14.176265
43	0.134142	0.083990	0.012725	0.230857
$\sum t_{ref}$	5.024044	4.762468	5.416221	
$\sum t_{ref_{dia}}$	0.202838	0.224128	0.368645	

Table 5.1: Quantification of dynamic $\boldsymbol{K}$ parameterisation via transient integration. Here, $\triangle_T(M) = \int_{beat}(\triangle M - \triangle Opt)\ dt$, where $\triangle M$ is the rms transient for the temporal parameterisation method M, and *beat* is the set of 50 discrete timesteps. It can be seen that $t_{ref} = 1$ produces the minimum $\triangle_T$, whether considering the parameterisation methods individually or in total. When all six reference timesteps are considered, it can be seen that the Mod_R parameterisation method is optimal. However, if the extreme t_{ref} are excluded, *i.e.* the end-diastolic and end-systolic cardiac stages, then the Ref method is optimal.

5.5 Discussion

We have identified an unmet need within the cardiac modelling community for detailed information on the typical deformations that the coronary network experiences throughout a full heart cycle. While the cryomicrotome-derived vascular models provide the realistic substrate on which to examine the effects of tissue motion, their inherent static nature means that any motion must be applied to them, rather than simply directly observed. In this chapter, we have developed a method to map a realistic left ventricular motion from one geometric model to another. This method was purposely developed in a general manner in principle to allow the mapping of displacements using a variety of source deformation fields *e.g.* cine MRI, *in silico* simulations *etc.*, although at the time of writing only the latter data source was available. The combination of

anatomically realistic vascular/tissue geometry models and the displacement mapping method represents a unique, and thus far unparalleled, data set with which to test scientific hypotheses.

5.5.1 Deformation Effects on Network Topology

Coarse-grain myocardial tissue strain can be determined via various techniques *e.g.* tagged MRI, sonomicrometry [118]. However, knowledge of the tissue deformation alone is not enough to determine the deformation of the embedded vascular network. One clearly also needs to know the vessel orientation as well, which is the key data that the cryomicrotome modality provides us. In this chapter, we have demonstrated how one can model the spatial distribution of vascular strain throughout the LV wall, and we have quantified this strain in a detailed manner (Figure 5.10). In our further analysis, we identified the choice of the reference time point as a key issue with using the standard definition of strain *i.e.* the ratio of deformed length over reference length. The importance of the $\boldsymbol{t_{ref}}$ value is obvious considering that it defines the reference length for all vessels. Perhaps less intuitive is the impact $\boldsymbol{t_{ref}}$ has with respect to dynamic changes in relative Poiseuille conductance. In our analysis, we have derived a simple relationship between a vessel's Poiseuille conductance and its stretch (Eq. (5.3.9)). As can be seen in Figure 5.9, this relationship is not axi-symmetric about the line $y = x$. In fact, a given amount of vessel extension produces a smaller effect on the relative conductance than the equivalent compression amount. This difference in behaviour is exaggerated in a non-linear fashion as the vessel's current length deviates further from its reference length.

In relation to experimental protocol, and to increase the confidence in our cho-

sen reference configuration, it would be beneficial to capture the network in the most physiologically-realistic state possible. For example, if end-diastole is our chosen point of reference, then ensuring correct LV cavity balloon deployment, and reducing fibre contraction to a minimum, would be advantageous for subsequent data collection and analysis.

It is important to note that one could challenge the entire idea of ever obtaining a realistic reference configuration for the vascular network, as it is continually subjected to mechanical forces, even in the heart's excised non-beating state. Thus it is appropriate to also consider measures of vascular deformation that are independent of time. In Figure 5.12, we have quantified the range of vessel length, which we defined to be the maximum length minus the minimum length, that the vessel attains during the heart cycle. We further increased the relevance of this finding by considering a normalised strain field, which was defined to the ratio of the vessel range to mean length. This quantification partially reveals the relationship between vascular deformation and scale, in both a global (Figure 5.13(A)) and a localised sense (Figure 5.13(B)). This strain data could be used as part of future studies, such as: *(i)* investigating a correlation between vascular range and the work done by the tissue in a region, *(ii)* linking greater normalised strain to a more temporally sensitive set of lumped-parameter regional blood flow model resistance parameters, and *(iii)* analysing time-dependent bifurcation angles.

5.5.2 Negligible Benefit of Temporal Parameter Updating

Similar to researchers across many numerical modelling fields, we judge our models in the context of both computational efficiency and biophysical com-

plexity. One seeks the most appropriate balance between these two key factors, and it is a strong motivating factor behind our adoption of continuum perfusion modelling frameworks and indeed the work of this thesis. This was true when we sought to incorporate discrete data with a static perfusion model, and it remains true also for our future dynamic hyperporoelastic perfusion model. The computational expense of this latter model will already be significant, due to the needs of strong-coupling between the solid and fluid domains, but also between the 1D and 3D components. Thus, it is important to examine methods for adapting our initial porous domain parameter fields to the dynamic scenario, and to do so in as efficient a manner as possible. We examined three intuitive approaches to model the effects of tissue deformation on the Darcy permeability fields, and quantitatively compared our continuum pressure results to the solution obtained when the parameter fields (both $\boldsymbol{K}$ and β) were re-evaluated at every timestep (Figure 5.14). Furthermore, due to the aforementioned difficulties surrounding the choice of a reference timestep, this comparison was repeated across a set of $\boldsymbol{t}_{ref}$ values chosen by their unique anatomical features. Several key results follow from this study:

(i) Perhaps the most striking finding is that an end-diastolic $\boldsymbol{t}_{ref}$ produces extremely poor results, as is clearly demonstrated by Figure 5.14(E). This result can be understood in terms of the relative conductance *vs* vessel stretch curve of Figure 5.9. The majority of vessels are in their most extended state at end-diastole, which is what this $\boldsymbol{t}_{ref}$ value has defined to be their reference state. For all other timesteps, these vessels are deemed to be in a compressed state, with the consequence that the relative conductance value is produced by the more non-linear portion of the relative conductance - vessel stretch curve *i.e.* values of stretch less than unity. Thus the longer reference lengths can lead to signifi-

cant alterations to the relative flux magnitudes determined by the permeability tensors, and in this instance, to a poor continuum pressure result.

(ii) $\boldsymbol{t_{ref}} = 1$ produced the best results of the six $\boldsymbol{t_{ref}}$ values tested. We can see from Table 5.1 that this is true both in terms of an analysis of any-$\boldsymbol{t_{ref}}$ any-methods results ($\boldsymbol{t_{ref}} = 1$ and method 'Mod$_F$' produced the best result) and any-$\boldsymbol{t_{ref}}$ all-methods results (the sum of the $\boldsymbol{t_{ref}} = 1$ results is less than the sum for any other $\boldsymbol{t_{ref}}$ value). While this result could not have been ascertained *a priori*, it does at least agree with the efforts made during the experimental process to ensure the heart was frozen in a condition approximating the end-diastolic state.

(iii) The 'Mod$_R$' method produced the lowest total rms discrepancy value. However, based on what we have observed thus far (particularly point *(i)* above), it is reasonable to reconsider this issue while discounting the results of the two extreme $\boldsymbol{t_{ref}}$ values *i.e.* the end-diastolic and the end-systolic reference timesteps. In this case, we found that the 'Ref' method is optimum. Therefore, it is recommended that dynamic perfusion models use the initial state parameter fields as, in our opinion, this does not produce unacceptably worse results while clearly being the most efficient in terms of computational expense. However, there is one caveat with respect this recommendation which is discussed in the following point.

(iv) Close inspection of the diastolic reference timesteps ($\boldsymbol{t_{ref}} = 1, 10, 18, \&26$) reveals that the largest instantaneous errors tend to occur around systole. This implies that the parameter updating methods are not as reliable during this phase of the cardiac cycle as during the less complex diastolic phase. Specifically, the 'Mod$_F$' method is consistently the worse during the systolic phase,

and the remaining two dynamic methods producing similarly improved results. There is the notable exception, however, of the 'Mod$_R$' method for $\boldsymbol{t_{ref}} = 1$. Its transient follows closely that of the 'Opt' or re-parameterised method. Thus, if the particular perfusion model application is expected to produce a pronounced apical rotation, *e.g.* in the case of uncomplicated type 1 diabetes mellitus (T1DM) or concentric hypertrophy, then it may be more appropriate to use the 'Mod$_R$' method.

5.5.3 Limitations of the Model

Throughout this study, we have assumed a simple deformation model for the network. Deformation acted directly on the length of the cylindrical vessels, and the radius altered accordingly to enforce constant fluid mass per vessel (see Eq. (5.2.6)). This would appear to contradict experimental findings in the rat heart that systolically arrested hearts have approximately 40% less intramyocardial blood volume than diastolically arrested hearts [139]. However, this figure includes capillaries and venuole volumes, and has not been shown to be representative of a healthy, intact heart. Furthermore, the assumed conservation of vessel volume ignores the effects of regionally varying IMP, which we have stated previously is likely to play a role in vascular deformation and effective conductance via vascular compression (see Section 5.1). It would require a complex model to adequately account for these effects, far more complex than the current model employed for this thesis. Arguably, a transient flow model incorporating inertial terms and vessel elasticity would be required to investigate myocardial contractile coupling to coronary blood flow. Such a model does not yet exist for the coronary arterial network, primarily due to difficulties in

parameterisation, validation, and tractability. We have also not examined shear effects on the cross-sectional vessel geometry, which could play a important role with long-term pathological/remodelling events which have been linked to non-trivial flow patterns and endothelial shear stresses [34, 76, 133, 154]. The effect of coronary tortuosity [158, 159], which is a feature of the systolic phase, has also not been investigated, due to limited information and the negligible effect it is likely to have on the intramural vessels of the scale considered in this study. Note that if these limitations are ameliorated in the future (in particular the vessel-wise fluid mass conservation assumption), then the findings of this chapter with respect to the wide-spread applicability of the undeformed porous parameters may no longer hold, and porous parameterisation based directly on the deformed network may be required for improved model accuracy.

The research featured in this chapter is largely focused on the permeability parameterisation rather than the pressure-coupling field, β. At first glance, this might appear to be a limitation of the study, however further examination reveals that this is not the case. Recall that the 'Opt' method, which was used throughout as our 'gold-standard' parameterisation method, re-parameterised both the $\boldsymbol{K}$ and β fields for each timestep. In contrast to this, the two 'Mod' methods only modified their permeabilities and kept the β fields constant at their $\boldsymbol{t}_{ref}$ values. The results displayed in Figure 5.14 shows that there is little to be gained from updating β simultaneously as part of these two methods, as it is likely that the resulting solution would lie between the original 'Mod' $\boldsymbol{K}$-only transient and the 'Opt' transient. Furthermore, similar to the reasons behind the definition of the β fields in the static instance (see Section 2.3.3, and in particular Eq. (2.3.10)), the point-wise value of β is a function of the entire displacement mapping, ψ. To see this, note that ψ alters the global vascular

network topology, thereby impacting on local Poiseuille pressures, fluxes and hence β values. Thus, updating β would pose a significant challenge from a numerical implementation point-of-view, for although the local $\boldsymbol{F}$ data is available at the level of the Gaussian integration point within each finite element, the global $\boldsymbol{F}$ information is typically not.

Finally, if one were to use a dynamic perfusion model where the Darcy porous parameters were derived using the $\phi\boldsymbol{I}$ method, as described in Chapter 4, then the assumption has already been implicitly made that network deformation does not affect the principal flow directions or relative flow magnitudes. That is not to say, however, that the porous parameter fields must remain constant. For example, in a hyperporoelastic perfusion model say, one can expect there to be a movement of fluid mass and thus changes in the local fluid volume. As increase-in-fluid-mass (or some equivalent variant) is a state variable in the hyperporoelastic framework, and is thus necessarily solved for, its use in modifying the $\boldsymbol{K}$ fields would come at almost no extra computational cost. Hence, the modification of $\boldsymbol{K}$ could be done in a manner consistent with the $\phi\boldsymbol{I}$ parameterisation method via, for example as has been used previously [58, 120, 149],

$$\boldsymbol{K}_t = \boldsymbol{K}_0 \left(\frac{J\phi_t^f}{\phi_0^f} \right)^2, \tag{5.5.1}$$

where ϕ_t^f is the fraction of fluid per unit tissue volume at time t.

Summary

The development of a parameterisation process for the porous compartments within a static Darcy perfusion model leads inevitably to the question of the dynamic updating of the parameter fields as the tissue undergoes a deformation. To examine this issue, a technique was devised and implemented that allows one to map a tissue displacement from one geometry onto another, cryomicrotome-derived, geometry. Various time-dependent and time-independent metrics were used to probe the effects of a realistic cardiac deformation on the porcine arterial model topology. Furthermore, several strategies were considered for the temporal updating of the Darcy permeabilities, and these strategies were of varying computational cost and physical realism. Our results suggest that for most perfusion modelling applications, the parameter fields derived from the original undeformed vasculature are adequate for dynamic perfusion modelling needs.

6 Conclusions

To conclude this dissertation, a discussion of the principal criticisms of the methods applied and the perfusion models used are presented in Section 6.1. This is followed by Section 6.2, which is a description of ongoing and planned research projects that build on the work reported herein. Finally, the contributions and principal scientific findings of this thesis are outlined in Section 6.3.

6.1 Limitations

A number of simplifying assumptions have been made during the course of this work that in some cases were to allow for a less complex perfusion model, and in other cases were enforced by factors beyond our control. Several key criticisms of the current dissertation are outlined below.

Vascular Model Assumptions

We assumed that all the coronary vessels were well-represented by cylindrical vessels. While we believe this is the correct model to apply for the intramural vessels in a study that does not look at wall shear stresses, it is more questionable for the larger, epicardial vessels. Such vessels do demonstrate some distal

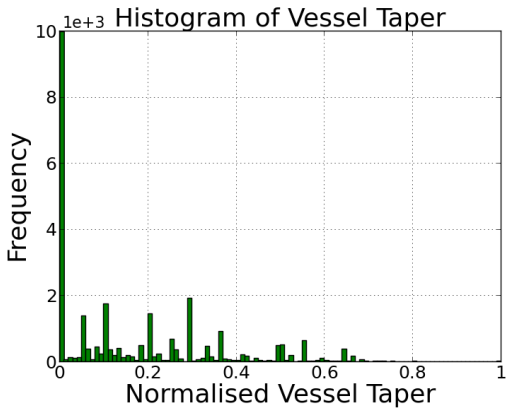


Figure 6.1: Distribution of the porcine arterial model normalised vessel taper. For a vessel with inflow and outflow radii, denoted r_a and r_b, the normalised vessel taper is defined to be $|r_a - r_b|/argmax\{r_a, r_b\}$. This data supports the cylindrical vessel modelling assumption.

tapering ([134] and references therein). This issue could be rectified by a variety of means, *e.g.* finer length discretisation, switching to a vascular nodal based radius field and adjusting the Poiseuille conductance equation, or even using higher order basis functions for the vessel interpretation and a more complex discrete flow model. However, given the small number of vessels that are significantly affected by tapering, we were satisfied to use the cylindrical approach taken (see Figure 6.1).

For the anatomical perfusion models, we applied a weak coupling between the 1D and 3D model components. Here, the mass flux exiting the 1D component was attributed to its spatially coincident finite element via the definition of the Darcy source fields s_i. In this situation, the global resistance experienced by the flow that produced these source fields was that of the discrete network, and not that of the 3D porous domain. Importantly, this approach does allow for the enforcement of equal fluid volume influx regardless of the continuum model parameters.

With respect to 1D/3D component coupling, it is clear that the applied approach conserves mass flux but does not conserve momentum. Balance of momentum is arguably a secondary effect as flow direction is largely determined

by the Darcy parameter fields, particularly so for a static domain perfusion model. Regardless, it is still one of the fundamental laws of classical physics, and one we are keen to preserve in our future, more application-focused perfusion models.

Derived Parameter Uncertainty Quantification

Of notable absence from this thesis is a detailed study and quantification of the uncertainly of our derived parameters. Inter- and intra-species variability of same organ and same phenotype vascular networks has yet to be studied on any scale, let alone one that is statistically significant. The primary reason for this would be the large expense of such a survey, in terms of both experimental costs and manual processing. The vascular extraction process is still at only a semi-automated state, and it unlikely to be fully automated within the foreseeable future due to inconsistencies amongst cryomicrotome data sets. Not only would an inter- and intra-species variability study be worthwhile from a basic physiological point-of-view, but it would also be an important future step if we wish to use averaged permeability fields within a generic perfusion model of the given organ. The importance of a statistical atlas is most easily observed in the desired patient-specific modelling scenario as, due to the aforementioned limitations of clinical imaging modalities, the myocardial vascular structure will not be available for continuum perfusion model parameterisation purposes. Thereby likely rendering the use of a statistical atlas of the Darcy parameterised fields as a requirement for perfusion modelling when the underlying network is not known.

Opportunities for Validation

While numerical models should be tested and validated as much as is deemed

necessary to demonstrate full efficacy of the model and the techniques used to obtain its solution, it is self-evident that this is an absolute necessity within the field of bio-engineering. Not only must the scientist be assured of the model's accuracy at representing the real-life problem, but the clinician (and regulatory bodies) must also trust in its output if it is ever to successfully make the translation from a research to a clinical environment.

For practical purposes, in this study, we have relied on *in silico* validation. However, the discrete model pressure was used to optimise the porous parameter fields scale. Therefore a portion of the same input data was used to validate the model as was used in the model construction itself. This is a necessary limitation given the small number of anatomical arterial models currently available. Once a full understanding of the vascular model variability and typical scales has been acquired, this limitation could be overcome.

It was originally our intention to complete a systematic comparison of our perfusion model results to the experimentally-obtained microsphere density data [115]. A microsphere deposition study would be one of the very few perfusion data types that are suitable for comparison to static perfusion model results (radioisotopes and thermoelectrical flow probes have also been used as surrogates for perfusion [91]). However, there are several serious issues with regards to using microsphere deposition results to validate flow models, some inherent to the flow of microspheres within the blood stream [115], and more related to the effects that deposited microspheres might have on the subsequent distribution of the vascular casting agent, as previously mentioned in Section 3.4. Therefore, one needs to validate the entire perfusion model against perfusion MRI data without the potentially deleterious presence of microspheres. This

requires a dedicated animal model study, but as this thesis shows, both the required experimental and engineering knowledge and capability to successfully conduct this study now exists. Furthermore, such a study would be the natural stepping-stone to our ultimate goal, which is clinical testing via the comparison of dynamic anatomically-parameterised perfusion model results to patient perfusion data.

6.2 Future Directions

The long-term aim to incorporate the anatomically-derived parameters within an existing hyperporoelastic model of perfusion [24] has been stated several times during this thesis, thereby providing the necessary context for our parameterisation efforts. We believe that embedding the anatomically-derived Darcy parameters within the poroelastic perfusion modelling framework would represent a significant step forward towards a clinically-useful dynamic porous perfusion model. That being said, there are some critical perfusion-related modelling opportunities that are wholly-amenable to being investigated via a less complex perfusion model. Two current projects are now described, that rely on, and build upon, the research conducted for this thesis.

6.2.1 Coronary Occlusion Simulations

The presence of a high-grade coronary *stenosis* or occlusion can lead to myocardial infarction, and a subsequent deterioration of cardiac function. Patient outcome is linked not only to the location and severity of the stenosis, but also to the degree of *collateralisation* present in the heart. Of relevance to the lat-

ter point, previous coronary vasculature studies strongly suggest that the myocardium is partitioned into regional perfusion zones, and that these regions are perfused by distinct arterial subnetworks [132]. This finding of isolated perfusion regions has been observed more recently via multi-coloured microsphere deposition studies [144, 145]. The implication of regional perfusion boundaries is that in a pathological event, such as coronary occlusion, the extent of the downstream hypoperfusion is dependent on the amount of blood flow entering the region from neighbouring zones of perfusion. Thus, it is important that our tissue property fields respect such known physiological features, and a perfusion model with varying levels of inter-region permeability is most suitable for investigating the effects of collateralisation on perfusion defects.

To this end, a method has been developed for arterial subtree extraction and a regional volume-growing algorithm to define each arterial perfusion region. More specifically, proximal vessels for each main arterial tree are selected. The challenge is to determine the volume of tissue perfused via the particular arterial tree. Using the same method as was used to define the hierarchic parameter field in Section 4.1.1, every myocardial vessel is attributed to a single one of the selected proximal arterial vessels by virtue of the dominant flux source calculated from a Poiseuille flow model (the single artery subtree that features in Cookson et al. [24] and Section 4.2.2 was extracted in this manner). A binary mask of the tissue geometry is created and the myocardial vessel centrelines are discretised and associated to their corresponding set of binary voxels. These voxels are tagged with an identifying integer unique to the selected proximal arterial vessel. In this manner, the tissue binary mask has been seeded according to the arterial subtree vessels perfusing that local region. A region-growing algorithm is then used to iteratively assign non-tagged voxels neighbouring a

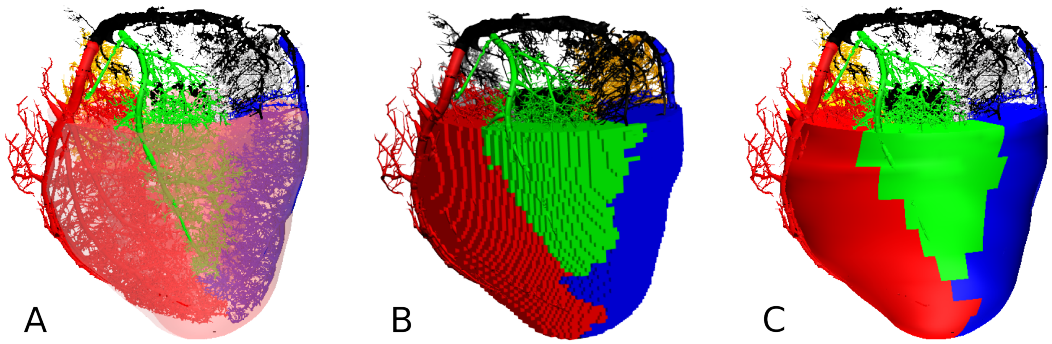


Figure 6.2: The main arterial networks of the porcine heart are used to define their perfusion volume *i.e.* the tissue they are deemed to supply with blood. (A) Arterial subtrees are coloured individually according to their distal relationship to five main coronary artery vascular model nodes. The subtree centrelines are used to seed a discrete region-growing algorithm until all the myocardium has been assigned to one of the subtrees. (B) The result of the regional seeding and growing algorithms. (C) The distinct regional perfusion zones for a course hexahedral finite element mesh as calculated from the binary tagged volume.

tagged voxel to the value of the tagged voxel. This algorithm continues until all tissue binary mask voxels have been assigned a tag, and is thus associated with the perfusing arterial subtree. Finally it remains to assign the perfusion model finite element mesh elements to their perfusing arterial subtrees via the dominant voxel tag resident in the element's volume. As can be seen in Figure 6.2, this method for defining regional perfusion zones has been applied to the porcine vascular model with five selected arterial subtrees, and a coarse cubic Hermite hexahedral mesh to determine five separate regional perfusion zones. Armed with the knowledge of the regional perfusion zone boundaries, we can strongly-couple the 1D and 3D flow domains, thereby allowing us to simulate a stenosis or occlusion anywhere in the proximal epicardial vessels while simultaneously altering the permeability of the regional perfusion zone to represent varying levels of collateralisation.

6.2.2 Contrast Agent Transport

As mentioned in the Section 1.1, clinical use of Contrast Agent (CA) enhanced MRI of myocardial perfusion provides a non-ionising, non-invasive, early indication of defects in the coronary circulation. Importantly, it also provides a direct representation of the underlying global perfusion state of the heart. However, there are several issues that confound the interpretation of CA perfusion results, chief amongst them are: the diffusive nature of current contrast agents; contrast agent properties (*e.g.* blood-bound or not); possible disease type (large-vessel or microvascular); saturation of the signal response curve; and partial volume effects. A mathematical model of CA transport within the myocardium is particularly amenable to improving our understanding of these issues and to quantify their interdependence. In the long-term, such a model could be used to guide CA design and selection for a given patient scenario. We have already completed one study that explores the key variables within a simplified 2D geometry [25]. A second study is underway that uses physiologically-realistic 3D geometries, anatomically-derived porous domain parameters, and two-way coupling between the 1D and 3D model components. A preliminary result from this study is presented in Figure 6.3.

6.3 Dissertation Contributions

The research presented in this thesis extends our knowledge of coronary perfusion modelling and physiology. This has been successfully achieved by the fusion of several powerful techniques: *(i)* novel experimental data, *(ii)* 3D vascular network reconstruction using a variety of image processing algorithms,

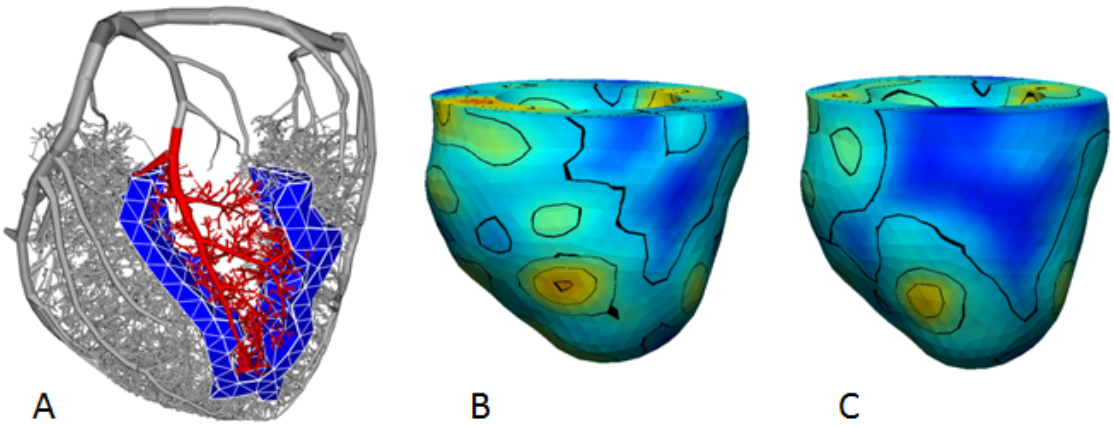


Figure 6.3: (A) A stenosis was modelled within a major arterial subtree (red) by decreasing its root vessel radius by a factor of 0.7. A regional perfusion boundary was imposed by applying zero permeability in the border finite elements (blue tetrahedra). The total concentration of contrast agent in the tissue 20 seconds after the simulated administration of a bolus injection for the healthy case (B) and the stenosis case (C).

(iii) an appropriate perfusion modelling framework, and *(iv)* rigorous and systematic model parameterisation.

Throughout this thesis, the focus has been on coronary perfusion modelling due to its significant medical importance and the considerable interest of the scientific community. However, the tissue and accompanying vascular network have, for the most part, been treated in a general manner (the exception to this is Chapter 5, which examined the issue of myocardial deformation effects on the vascular topology). Thus, the parameterisation methods, and the findings with respect to sampling domain size and vessel density sensitivities, are applicable to perfusion models of various tissue types *e.g.* lung [11, 107], kidney [4, 153], brain [2] *etc.*

This work has produced many novel outcomes, which are now summarised:

- The coronary perfusion modelling pipeline developed during the course of this thesis is unique. To the best of our knowledge, no other research group has previously combined *(i)* myocardial perfusion modelling ex-

pertise (1D Poiseuille/Navier-Stoke flow, 3D multi-compartment static and dynamic Darcy flow, hyperporoelastic flow), *(ii)* access to several high-resolution arterial network models from various species and organs (plus the imaging of venous networks is scheduled for the near future), and *(iii)* expert clinical advice and imaging data such as anatomical and Late Gadolinium Enhancement (LGE) perfusion MRI (Prof. Eike Nagel and Prof. Reza Razavi, King's College London, UK)

- The porcine and canine perfusion models presented in Chapter 3 are the first whole-organ perfusion models to be parameterised using the underlying anatomical network. This a significant step forward in the biophysical parameterisation of perfusion models. Furthermore, it may also encourage a move away from the generation of CCO networks for biophysical modelling purposes, which may be accurate in terms of global vessel statistics but fail to capture the local variations in structure.

- This is the first comprehensive and systematic comparison of parameterisation methods for a continuum perfusion model using the underlying vascular network.

- The high-resolution dynamic anatomical vascular network featured in Chapter 5 represents another unique contribution to biomedical engineering. Until now, the closest such network is the CCO network featured in Smith *et al.* [127], which has only six vessel generations. One could now probe the link between vascular topology and mechanical strain throughout the cardiac cycle.

With regards to the contributions that this research has made to the field of

biomedical engineering, the principal scientific findings are:

- Our original hypothesis that discrete vessel data can be successfully incorporated within continuum models of perfusion was found to be true. This hypothesis was conjectured based on the seminal yet limited study of the 2D synthetic network assimilation study of Vankan *et al.* [148]. We successfully applied spatial-averaging techniques to parameterise perfusion models based upon 3D synthetic, rat capillary, canine LV arterial and porcine LV arterial discrete vascular models.

- One should be wary with respect to RVE size and vessel density when applying spatial-averaging techniques. The rigorous quantitative analysis carried out in Chapter 2 has revealed the key role that these two variables play in terms of overall discrete *vs* continuum pressure results.

- The robustness of the parameterised fields to the pressure BCs has been demonstrated. This finding is of crucial importance in terms of the long-term application of the parameterisation methods considered in this work to dynamic perfusion models. Not only does the pressure entering the coronary vascular system periodically fluctuate due to the beating heart, the pressure could also undergo large local changes during cardiomyopathy.

- The parameterisation of the porous permeability tensor fields is of secondary importance relative to the pressure-coupling method applied. Not only have we demonstrated a clear improvement when allowing for a more general connectivity amongst porous compartments as opposed to strictly-hierarchical compartmental communication (Section 4.2.2, [24]),

but also for the use of anatomically-derived β fields in contrast to homogeneous scaling fields (Section 4.2.3).

- The parameterisation method of HvC cannot be used "as is" for anatomical networks. We can attribute this failing to the occurrence of 'small length - large radius' vessels which skew the permeability tensor field values.

- There is strong evidence to suggest that the temporal updating of the Darcy parameters during a dynamic perfusion simulation is not necessary. Although shown using the static multi-compartment Darcy perfusion model, this finding is most relevant within the framework of the hyperporoelastic perfusion model. A similar study as that undertaken in Chapter 5 is planned for the hyperporoelastic model in the near future. Overall, this study increases the tractability of myocardial perfusion modelling using data-driven Darcy parameters that improve the biophysical realism of our models.

As a concluding remark to this section, this thesis is also an example of both data- and application-driven science, based upon large-scale collaboration and interdisciplinary research. Experimental physiologists, image processing specialists, mathematical modellers, numerical analysts, cardiologists – all have either contributed or will use the results of this thesis. Indeed, as illustrated by our perfusion modelling pipeline of Figure 1.4, this research has been fundamentally constructed upon the three pillars of bioengineering: instrumentation development, experimental measurement, and mathematical modelling.

A

FEM Solutions for Darcy Flow

The Darcy model for fluid flow in porous media has been solved numerically via the Finite Element (FE) method to provide key results throughout this thesis (*e.g.* Chapter 2, Chapter 4 and Chapter 5). In light of the prevalence of numerical solutions within this dissertation, it may benefit the reader to briefly discuss the use of numerical solution techniques within mathematical modelling, with a particular focus on the FE method.

Mathematical modelling is used to study and predict behaviour in a huge range of physical and biological processes. The goal of modelling is to develop systems of equations that describe the behaviour of the desired process. These systems of equations often take the form of coupled ordinary differential equations or Partial Differential Equations (PDEs). Analytical solutions may exist for simple processes, but mathematical models often become intractable as they become more complex *e.g.* the inclusion of nonlinear effects, high spatial dimensions, or dynamic domains of interest. Thus, models of complex systems often necessitate the use of a numerical scheme to compute approximate solutions to the equations.

Various methods have been developed for the numerical solution of equations,

such as finite difference methods [44], finite volume methods [150], FE methods [10, 23, 164], and spectral methods [140]. Of these, the finite difference method is arguably the most elementary, being founded upon Taylor's Theorem, and involving the approximation of derivatives of a variable with linear combinations of values of the given variable at nearby points. The finite volume method is used extensively in Computational Fluid Dynamics (CFD) applications. Whereas in the finite difference method the PDE is approximated only at a grid-point (*a.k.a* a 'node'), in the finite volume method the PDE is approximated at 'control regions', which are volumes that enclose a single node. The PDE is integrated over the control region, allowing boundary conditions to be applied through use of the divergence theorem. The FE method also involves integrating the PDE over small volumes, here called 'elements', but is more complex than the finite volume method as quantities of interest are allowed to take various possible functional forms, depending on the types of 'basis functions' (defined shortly) used. In the FE method, the basis functions are generally piece-wise polynomials and are non-zero only in small regions (*i.e.* they have local compact support). Spectral methods can be considered as an analogous method in which globally smooth basis functions are used, either trigonometric polynomials or orthogonal polynomials, together with specific quadrature rules. This approach works effectively on problems involving highly smooth functions and simple domains [140].

Of the numerical methods available, the FE method is probably the most common. The FE method was first proposed in 1943 by Richard Courant, although most of the essential mathematical analysis behind the method was not carried out until the 1960s [164]. In the FE method, differential equations (known as the strong formulation) are reformulated as equations in terms of integrals over the

domain (known as the weak formulation), involving functions from infinite-dimensional function spaces. By approximating these functions by functions from finite-dimensional function spaces, we obtain the FE problem *i.e.* an integral problem over a finite-dimensional space that can be rewritten as a linear matrix problem (or a finite set of nonlinear equations) and solved using numerical techniques from linear algebra.

In relation to this dissertation, the FE method was chosen given its wide applicability to biomedical engineering problems *e.g.* passive and active mechanics [103], fluid mechanics [129], Fluid Solid Interaction (FSI) [127], tissue activation [103], solute transport [125] *etc.*

In Section A.1, the various components and stages involved in the FE method are introduced within a general setting. The application of the FE method to the specific problem of Darcy flow modelling over 2D domains is then discussed in Section A.2, and some sample results are presented in Section A.3.

A.1 Introduction to the Finite Element Method

A.1.1 Nodes, Elements and Basis Functions

The first stage in using the FE method to solve a problem numerically is to create a mesh which encompasses the domain of the problem. A mesh is a collection of:

- nodes – which are points in the domain, and
- elements – which are regular-shaped subsets of the domain, generally tetrahedra or hexahedra (or their lower dimensional equivalents in 1D

or 2D), and having nodes for vertices.

More formally, let $\Omega \subset \mathbb{R}^n$ be the domain over which the problem has been posed. Define the nodes as a set of points $\{\boldsymbol{X}_i \in \Omega, i = 1, ..., \mathcal{N}\}$, and the elements as a set of regular-shaped open subsets $\{K_i \subset \Omega, i = 1, ..., \mathcal{M}\}$, satisfying $K_i \cap K_j = \emptyset$ if $i \neq j$, and containing only nodes at vertices. Note that a node may not necessarily be a vertex of an element. Define the computational domain, Ω^h, to be the union of the closures of the elements, *i.e.*

$$\Omega^h = \bigcup_{i=1}^{\mathcal{M}} \overline{K}_i. \tag{A.1.1}$$

For the purposes of this work, we demand that if a node is a vertex for any element, it is also a vertex of any neighbouring element. A node which does not satisfy this property is known as a *hanging node*, the treatment of which is not discussed herein but can be found in the relevant textbooks [164]. An example mesh of a two-dimensional computational domain is shown in Figure A.1(B). The computational domain is the domain over which integrands that appear in the weak formulation will be integrated, and elements are regions over which integration will be considered separately.

In the FE method, unlike the finite difference method, values of the numerical solution can be calculated at any point in the mesh. This is because the numerical solution is assumed to take a known functional form, and not to consist of a set of nodal values only. For the nodal Lagrange FE method, the numerical solution is computed at the nodes however, like in finite difference methods, as this value is used in the approximation scheme. To interpolate values of the numerical solution at non-nodal points from their nodal values, one needs to

define basis functions. These functions can take the form of polynomials (in 1, 2, or 3 spatial variables) over any particular element, and (apart from the case of piecewise constant basis functions) are continuous throughout the computational domain. Furthermore, basis functions satisfy the important property that

$$\varphi_i(\boldsymbol{X}_j) = \delta_{ij}, \tag{A.1.2}$$

where φ is the basis function associated with the node $\boldsymbol{X}_i$, and δ is the Kronecker delta function (*i.e.* φ_i takes the value 1 at node i and 0 at all other nodes). Basis functions are used to interpolate any quantity of interest across the computational domain. Different orders of basis functions can be used to interpolate different quantities, such as fluid velocities, pressure *etc.* For example, suppose there exists a quantity u whose nodal values are u_i at $\boldsymbol{X}_i$. Given a set of basis functions $\{\varphi_j\}$ associated with each node, the functional form of u when interpolated by these basis functions is given by

$$u(\boldsymbol{x}) = \sum_{i=1}^{\mathcal{N}} u_i \varphi_i(\boldsymbol{x}), \tag{A.1.3}$$

where $\boldsymbol{x} \in \Omega^h$. Note that by Eq. (A.1.2), $u(\boldsymbol{X}_j) = u_j$.

A.1.1.1 Piecewise Bilinear Basis Functions

As mentioned above, the basis functions can take the form of polynomials. Generally, the order of the polynomial is chosen based on the following considerations:

- The requirements of the equations system *e.g.* function spaces, and field discontinuities and differentiability,

- The desired accuracy of the solution, and
- Computational efficiency.

We next describe in detail the implementation of one particular order of basis function commonly used in 2D FE simulations – the bilinear Lagrange basis functions. For reasons of conciseness, the piecewise constant or the higher order basis functions are not explicitly presented as their implementation can be intuitively derived from the bilinear case, and they are extensively documented elsewhere [164].

To specify the basis functions, it is easiest to consider them on one single element, called the *canonical* or *master* element. The linear basis functions on this element are the linear functions which take the value one on one node and zero on the others. The master quadrilateral is taken to be the unit square $[0,1] \times [0,1]$, with nodes labeled as shown in Figure A.1(A). Assuming a local coordinate system of the master element given by (ξ, η), then the bilinear basis functions are

$$\begin{aligned} \varphi_1 &= (1-\xi)(1-\eta), \\ \varphi_2 &= \xi(1-\eta), \\ \varphi_3 &= \xi\eta, \\ \varphi_4 &= (1-\xi)\eta. \end{aligned} \tag{A.1.4}$$

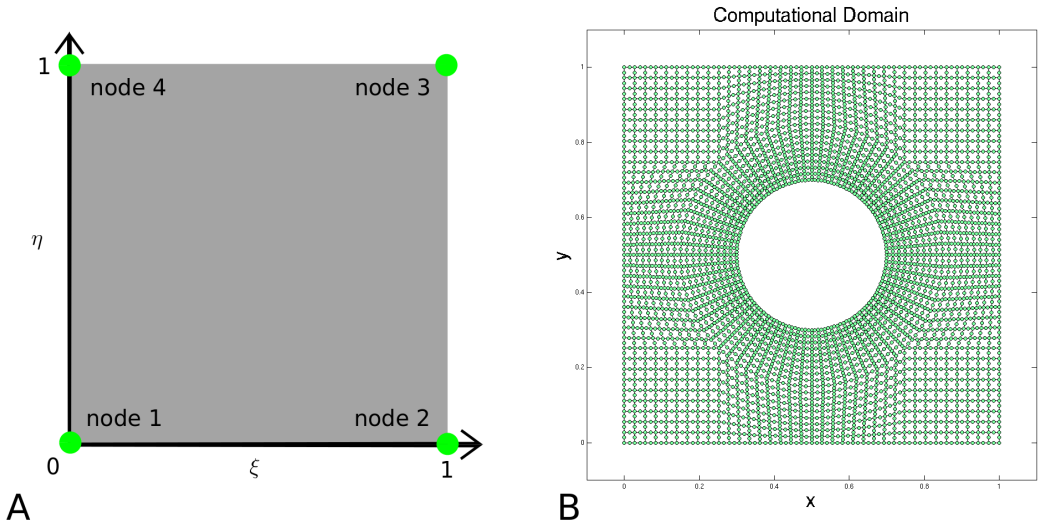


Figure A.1: (A) Master 2D bilinear element. (B) The computational domain on which the Darcy system of equations is solved. This 2D mesh consists of 5,076 nodes and 1,620 quadratic elements.

A.1.2 Weak Formulation and the Finite Element Formulation

Let $\Omega \subset \mathbb{R}^n$ be compact (*i.e.* closed and bounded, see [23]). The function f is said to be square-integrable over the volume V, or $f \in L^2(V)$, if $\int_V f^2 dV < \infty$. The first Sobolev space H^1 on Ω is defined as the set of functions on Ω which are square-integrable and whose first (weak) derivatives are also square-integrable. Note that a weak derivative is a generalisation of the classical derivative, and is useful for functions which do not have a strict classical derivative but have a classical derivative almost everywhere. For precise definitions of weak derivatives and Sobolev spaces, see [164]. Let $\partial\Omega$ be the boundary of Ω, and $\Gamma \subset \partial\Omega$ be the portion of $\partial\Omega$ with imposed Dirichlet BCs (*i.e.* the portion of the boundary where the value of the solution variable is specified), and define $H^1_0 = \{v \in H^1 : v = 0 \text{ on } \partial\Omega\}$, and $H^1_{0,\Gamma} = \{v \in H^1 : v = 0 \text{ on } \Gamma\}$. For the treatment of Neumann BCs, see [23]. Then the general weak problem for one unknown u

subject to zero-Dirichlet BCs on Γ is: find $u \in H^1_{0,\Gamma}$ such that

$$\int_\Omega f_1(u, v, \boldsymbol{\nabla} u, \boldsymbol{\nabla} v) dV_0 + \int_{\partial\Omega} f_2(\boldsymbol{\nabla} u \cdot \hat{\mathbf{n}}, v) dS_0 = \int_\Omega g(v) dV_0 \qquad \forall v \in H^1_0, \tag{A.1.5}$$

where f_1, f_2 and g are known functionals, and $\hat{\mathbf{n}}$ is the unit outward normal vector on $\partial\Omega$. In this context the functions $v \in H^1_0$ are known as *test functions*. Existence and uniqueness of solutions of weak problems in the linear elliptic case can be established if the weak form satisfies the conditions of the Lax-Milgram lemma [23].

Defining

$$\begin{aligned} a(u, v) &= \int_\Omega f_1(u, v, \boldsymbol{\nabla} u, \boldsymbol{\nabla} v) dV_0, \\ b(v) &= \int_\Omega g(v) dV_0 - \int_{\partial\Omega} f_2(\boldsymbol{\nabla} u \cdot \hat{\mathbf{n}}, v) dS_0, \end{aligned} \tag{A.1.6}$$

the general weak form can be written more succinctly as: find $u \in H^1_{0,\Gamma}$ such that

$$a(u, v) = b(v) \qquad \forall v \in H^1_0. \tag{A.1.7}$$

The FE problem is obtained by replacing the domain with the computational domain, and by solving the weak formulation over finite-dimensional function spaces. Given basis functions on Ω^h with which to interpolate u (and which are zero on Γ), we define V^h to be the set spanned by these basis functions, and $V^h_0 = \{v^h \in V^h : v^h = 0 \text{ on } \partial\Gamma\}$. The ciarlet1978finite problem is then: find $u^h \in V^h$ such that

$$a^h(u^h, v^h) = b^h(v^h) \qquad \forall v^h \in V^h_0, \tag{A.1.8}$$

where

$$a^h(u^h, v^h) = \int_{\Omega^h} f_1(u^h, v^h, \boldsymbol{\nabla} u^h, \boldsymbol{\nabla} v^h) dV_0, \tag{A.1.9}$$
$$b^h(v^h) = \int_{\Omega^h} g(v^h) dV_0 - \int_{\partial\Omega^h} f_2(\boldsymbol{\nabla} u^h \cdot \hat{\mathbf{n}}, v^h) dS_0.$$

The question of under which conditions the FE solution approximates the solution to the full problem is fundamental to FE analysis. The existence and uniqueness of a solution to the FE problem can be determined for some problems using the Lax-Milgram lemma, similarly to the initial weak problem above (Eq. (A.1.5)). Associated issues and the conditions for convergence of the FE solution to the true solution as the FE mesh is refined is discussed in detail in the literature [136].

Suppose we wish to solve the FE problem for values of the unknown u at the nodes, excluding those nodes which are on the Dirichlet boundary, where the value of u is known. The number of nodes is $\mathcal{N}$, so supposing the number of nodes on the Dirichlet boundary is $\mathcal{N}_d$, then the number of unknowns is $\mathcal{N} - \mathcal{N}_d$. The dimension of the space V_0^h is also $\mathcal{N} - \mathcal{N}_d$, and we obtain the $\mathcal{N} - \mathcal{N}_d$ equations for the $\mathcal{N} - \mathcal{N}_d$ unknowns by considering Eq. (A.1.8) and setting v^h to be the basis functions corresponding to non-Dirichlet nodes (*i.e.* the basis functions which span V_0^h). Thus the $\mathcal{N} - \mathcal{N}_d$ equations determining the unknown nodal values of u^h are

$$\mathcal{F}_i(\{u_j\}) := a^h(u^h, \varphi_i) - b^h(\varphi_i) = 0. \tag{A.1.10}$$

The vector whose components are $\mathcal{F}_i$ is known as the *residual vector*. For linear systems, $\mathcal{F}_i$ is a linear vector function of the unknowns u_j, and can be written in matrix equation form as

$$\mathcal{F} = \mathcal{A}\mathcal{U} - \mathcal{B}, \tag{A.1.11}$$

where $\mathcal{U} \in \mathbb{M}_{(\mathcal{N}-\mathcal{N}_d,1)}$ is the vector of unknowns u_j. It is straightforward to show that the matrix $\mathcal{A}$ (known as the global stiffness matrix) is given by

$$\mathcal{A}_{ij} = a^h(\varphi_i, \varphi_j), \tag{A.1.12}$$

and the vector $\mathcal{B}$ (known as the global load vector) is given by

$$\mathcal{B}_i = b^h(\varphi_i). \tag{A.1.13}$$

As we shall see shortly, our target system of equations (*i.e.* Darcy flow) is linear. For nonlinear problems $\mathcal{F}$ is a nonlinear function of the unknowns, in which case a numerical scheme for solving finite-dimensional nonlinear systems must be used *e.g.* the Newton-Raphson method [10]. Further details on the solution of nonlinear systems can be found in the literature [10, 136, 164].

A.1.3 System Assembly for Linear FE Problems

Setting up the matrix equation (Eq. (A.1.11)) involves the computation of integrals over the computational domain. To do this, the total integral is split into a sum of integrals over elements. The idea is to loop over the various elements, calculating the contributions to the global stiffness matrix and global load vector from that element, and adding these contributions to the global matrix and

vector. These contributions take the form of Element Stiffness Matrices (ESM) and Element Load Vectors (ELV). The ESM for the element k is the matrix $\mathcal{A}^{(k)}$ which satisfies

$$\int_k f_1(u^h, \varphi_j^{(k)}, \boldsymbol{\nabla} u^h, \boldsymbol{\nabla} \varphi_j^{(k)}) dV_0 = \left((\mathcal{U}^{(k)})^T \mathcal{A}^{(k)} \right)_j, \tag{A.1.14}$$

where $(\cdot)^T$ is the transpose operator, $\mathcal{U}^{(k)}$ is a small vector containing the nodal values of u for only the nodes contained in the element k, and φ_j is the j^{th} local basis function for the element k. In other words, the ESM comes from restricting all integrals to just the element in consideration. The ELV is defined similarly as the vector $\mathcal{B}^{(k)}$ satisfying

$$\int_k g(\varphi_j^{(k)}) dV_0 - \int_{k \cap \partial\Omega^h} f_2(\boldsymbol{\nabla} u^h \cdot \hat{\mathbf{n}}, \varphi_j^{(k)}) dS_0 = \left(\mathcal{B}^{(k)} \right)_j, \tag{A.1.15}$$

which is independent of u^h as either $u = 0$ or $\boldsymbol{\nabla} u \cdot \hat{\mathbf{n}}$ is given on the boundary.

Hence, for 2D quadrilateral bilinear elements, the ESM is a 4×4 matrix, since there are four nodes associated to the element, and the ELV is a 4×1 vector. Once computed, the components of the ESM and the ELV are added to the appropriate entries of the global stiffness matrix and load vector.

A.1.4 Numerical Integration and Gaussian Quadrature

By the above assembly process, the entries of the residual have been reduced to a sum of integrals of known quantities over elements. These quantities, being interpolated over the element by polynomial basis functions, are continuous. In general however, the integrals cannot be computed analytically, and a numerical integration scheme is necessary. To numerically approximate an integral, we

transform the integral to the master element, $\overline{K}$, and use Gaussian quadrature, where the integral of a function is approximated by a weighted sum of function evaluations. Gaussian quadrature involves the use of a fixed number of known quadrature points, $\tilde{x}_i$, and known weights w_i, $i = 1, ..., \mathcal{G}$ in the master element. The integral of a quantity over $\overline{K}$ is approximated by

$$\int_{\overline{K}} F(x)dV \approx \sum_{i=1}^{\mathcal{G}} w_i F(\tilde{x}_i). \tag{A.1.16}$$

Quadrature points and weights can be chosen so that Gaussian quadrature is exact on all polynomials on the element of degree $<= 2\mathcal{G}$ [10].

Once the global stiffness matrix and global load vector have been defined, it remains to solve the linear system

$$\mathcal{F} = 0 \Leftrightarrow \mathcal{A}\mathcal{U} = \mathcal{B}. \tag{A.1.17}$$

This matrix equation can be solved by a variety of techniques, such as Gaussian elimination with back substitution, LU decomposition, or the Gauss-Seidel method (see [141] for further details on these solution techniques and a discussion of direct *vs* iterative solution schemes).

A.2 Darcy Flow Solutions via FEM

We have described the FE method in a general sense above. In this section, the focus shifts to the particular system of equations that describe Darcy flow. The multi-compartment formulation has been presented in Eq. (2.1.1), and its FE treatment can be found in Michler et al. [97]. We deem the more common

single-compartment formulation as sufficient for the purposes of elucidating its solution via the FE method. Recall that the classical Darcy system is given by

$$\boldsymbol{w} = -\boldsymbol{K} \cdot \boldsymbol{\nabla} p \text{ in } \Omega, \tag{A.2.1}$$

$$\boldsymbol{\nabla} \cdot \boldsymbol{w} = s \text{ in } \Omega, \tag{A.2.2}$$

where $\boldsymbol{w}$ and p denote the Darcy velocity and pore pressure respectively, $\boldsymbol{K}$ is the permeability tensor of the porous medium, and s is a volumetric source field.

This system is augmented by the following Dirichlet and Neumann boundary conditions respectively,

$$\boldsymbol{w} \cdot \hat{\mathbf{n}} = \zeta \text{ on } \Gamma_D, \tag{A.2.3}$$

$$p\hat{\mathbf{n}} = \varsigma\hat{\mathbf{n}} \text{ on } \Gamma_N, \tag{A.2.4}$$

where ζ is the designated normal component of the velocity field on the boundary and ς are given boundary tractions. We further assume that $\Gamma_D \cup \Gamma_N = \partial\Omega$ and $\Gamma_D \cap \Gamma_N = \emptyset$.

The variational formulation of the Darcy system can be expressed as follows: given $\boldsymbol{K}$ and $s \in L^\infty(\Omega)$, find $\boldsymbol{w} \in V_w$ and $p \in V_p$ such that for all $\boldsymbol{v} \in V_w$ and $q \in V_p$,

$$a(\boldsymbol{w}, p, \boldsymbol{v}, q) = b(\boldsymbol{v}, q), \tag{A.2.5}$$

where

$$a(\boldsymbol{w}, p, \boldsymbol{v}, q) = \int_\Omega \Big[(\boldsymbol{v} \cdot \boldsymbol{K}^{-1}\boldsymbol{w}) - (p\boldsymbol{\nabla} \cdot \boldsymbol{v}) + (q\boldsymbol{\nabla} \cdot \boldsymbol{w})\Big]\, dV_0, \tag{A.2.6}$$

and

$$b(\boldsymbol{v}, q) = \int_{\Omega} qs \, dV_0 - \int_{\Gamma_N} \boldsymbol{v} \cdot \varsigma \hat{\mathbf{n}} \, dS_0. \tag{A.2.7}$$

The infinite dimensional function spaces are given by

$$V_w = H(div, \Omega) = \{\boldsymbol{v} | \boldsymbol{v} \in L^2(\Omega), div(\boldsymbol{v}) \in L^2(\Omega), \boldsymbol{v} \cdot \hat{\mathbf{n}} \in H^1_{0,\Gamma}\}, \tag{A.2.8}$$

$$V_p = L^2(\Omega) = \{p | p \in L^2(\Omega)\}, \tag{A.2.9}$$

where $div(\cdot)$ is the divergence operator.

Discretisation of the variational problem (Eq. (A.2.5) – Eq. (A.2.9)) is obtained by replacing the infinite-dimensional function spaces by finite-dimensional subspaces. For the discrete setting, we use nodal Lagrange elements with basis functions that are in H^1_0 rather than $H(div, \Omega)$ to approximate the velocity solution with the assumption that the given data for the problem results in a solution that is also in H^1_0.

To obtain a stable and convergent numerical discretisation of the classic Darcy system, the discrete velocity and pressure spaces must satisfy the Babuska-Brezzi condition, also referred to as the inf-sup condition, which is a condition on the compatibility of the interpolation spaces used for velocity and pressure [36]. To this end, mixed formulations are typically employed, *i.e.* different interpolations are used for velocity and pressure where the latter must not be of too high an order, otherwise the inf-sup condition is violated. For the results shown in the next section, we used a bilinear pressure approximation and a biquadratic velocity approximation. Alternatively, stabilisation techniques can be employed to circumvent the inf-sup condition and ensuing restrictions on the choice of interpolation spaces [36, 90].

Finally, we have presented the strong and weak formulations of what is known as the *full* Darcy system, whereby the Darcy velocity and pressures are simultaneously solved for. We could also have substituted Eq. (A.2.1) into Eq. (A.2.2) to derive the *reduced* Darcy formulation [97]. The reduced Darcy system is associated with two main advantages: *(i)* there is typically a dramatic reduction in the size of the algebraic system obtained, and *(ii)* the imposition of impermeable BCs on arbitrarily curved boundaries is naturally inherent by the weak formulation process. The disadvantage of the reduced Darcy system is that the imposition of a non-trivial velocity BC is enforced only in the weak sense rather than strongly as a Dirichlet condition in the full Darcy model.

A.3 Sample Results and Software Verification

As mentioned in the dissertation 'Foreword', an in-house closed-source software package, called 'CHeart', was used to solve the continuum perfusion models in this dissertation. To provide an independent verification of this software, the FE method described in the previous sections was implemented in a commercial software package (MATLAB R2012b, The MathWorks Inc., Natick, MA, 2000). A computational domain was constructed which consisted of a unit square with a central disk of radius 0.2 units removed (Figure A.1(B)). The permeability tensor was assumed to be equal to the identity tensor for two dimensions. The Darcy flow model was solved on this domain subject to imposed BCs of

$$w_1 = 1 \text{ on } x = \{0,1\}, \text{ and } w_2 = 0 \text{ on } y = \{0,1\}, \tag{A.3.1}$$

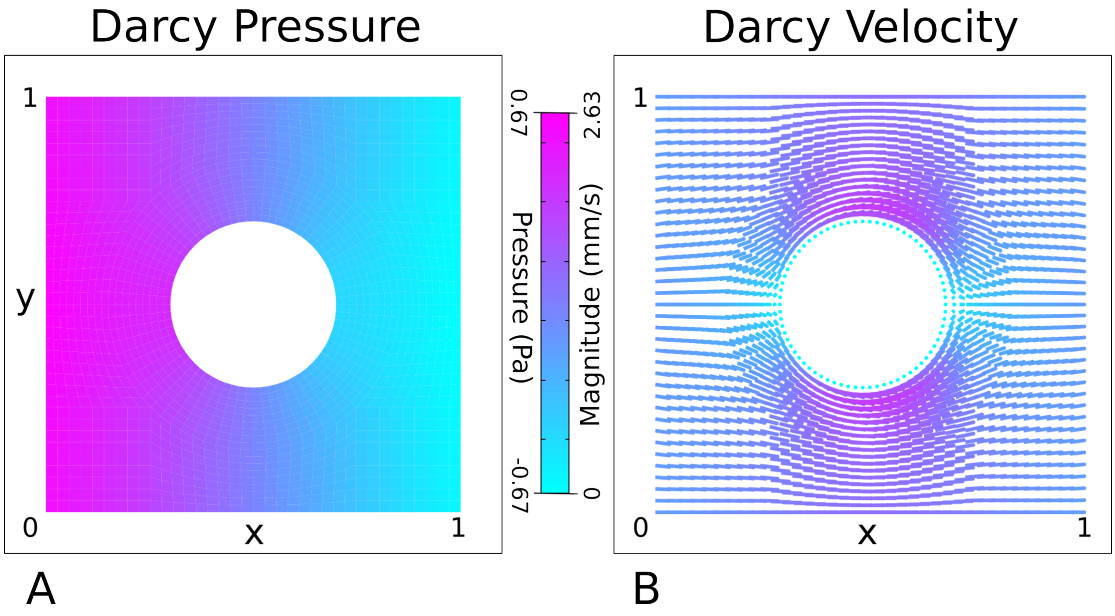


Figure A.2: Results from the finite element simulation on the unit mm square for flow moving generally from left-to-right with a no-slip BC on the central disk boundary. (A) Darcy pressure field with a mean pressure of zero. (B) Darcy velocity field coloured by velocity magnitude.

with a no-slip BC on the disk surface. Note that without specifying a Dirichlet pressure BC, the pressure field is only determined up to a constant. Thus, the pressure solution was uniformly shifted to yield an average pressure value of zero. The Darcy pore pressure is shown in Figure A.2(A), and the Darcy velocity vectors at the biquadratic nodes (scaled by a factor of 0.1) are shown in Figure A.2(B). The rms difference in both pressure and velocity results between this FE implementation and 'CHeart' were found to be less than machine precision.



A Brief Introduction to Poroelasticity

Our intention to apply the continuum multi-compartment Darcy parameters within a (hyper)poroelastic perfusion model has been mentioned at several stages in this dissertation (*e.g.* Section 3.2, Section 3.4, Section 5.1, and Section 6.2). While poroelastic perfusion simulation results do not feature in this work, we believe that it may aid the reader to provide a brief description of this modelling framework. In addition to this chapter, further details can be found in the relevant literature, in particular the seminal books by Biot ([9]), Bowen ([13]) and Coussy ([26, 27]) as well as key research papers by Vankan et al. [147], Ng et al. [101], Chapelle et al. [19], Tully and Ventikos [142] (application to cerebrospinal fluid hydrodynamics) and our own Cookson et al. [24]. The formulation of the poroelastic perfusion model presented in the next section is based on our work presented in the latter paper.

B.1 Poroelastic Perfusion Model Equations

In this section, we describe our previous work to develop a multi-compartment coupled porous-mechanical model of the cardiac left ventricle, providing a mod-

elling framework for the future integration of both detailed structural and clinical imaging data [24].

B.1.1 Flow

We consider first a single-compartment fully-saturated porous medium consisting of a fluid and solid phase. The total mass of the volume Ω is given by

$$m_{tot} = \int_{\Omega} (\rho_f \phi_f + \rho_s \phi_s) dV, \tag{B.1.1}$$

where $(\cdot)_{f(s)}$ refers to a fluid(solid) phase property, ϕ is the volume fraction, and ρ is the phase density. Our assumption of a fully-saturated medium implies that

$$\phi_f + \phi_s = 1. \tag{B.1.2}$$

It is important to note however, that if the solid matrix (*a.k.a* skeleton) is deformable, then the bulk porous medium will be compressible as the pore space can undergo volume changes due to net fluid flux. For the same reasons presented in Section 2.1.1, we generalise this system to a multi-compartment scenario, thus Eq. (B.1.2) becomes

$$\sum_{i=1}^{N} \phi_{f,i} + \phi_s = 1. \tag{B.1.3}$$

We next present the evolution equations for the phases in their Lagrangian form. We denote the reference and deformed coordinates as $\boldsymbol{x}$ and $\boldsymbol{X}$ respectively, and $\boldsymbol{y} := \boldsymbol{x} - \boldsymbol{X}$ is the skeleton displacement. Assuming Darcy flow, the

equations for the fluid transport in compartment i are given by

$$\frac{\boldsymbol{F}\cdot\boldsymbol{M}_i}{\rho_f} = -J\boldsymbol{K}_i\boldsymbol{F}^{-T}\nabla_X p_i, \tag{B.1.4}$$

$$\frac{d^s m_i}{dt} + \nabla_X \cdot M_i = \rho_f q_i + \sum_{k=1}^{N} -J\beta_{i,k}(p_i - p_k), \tag{B.1.5}$$

where $\boldsymbol{M}$ is the Lagrangian Darcy flow vector, which is related to the Eulerian relative flow vector by

$$\boldsymbol{M}_i = J\boldsymbol{F}^{-1}\boldsymbol{w}_i, \tag{B.1.6}$$

with

$$\boldsymbol{w}_i = \rho_f\phi_{f,i}(\boldsymbol{V}_i^f - \boldsymbol{V}^s), \tag{B.1.7}$$

where $\boldsymbol{V}^f$ and $\boldsymbol{V}^s$ denotes the velocity of the fluid and of the skeleton respectively. Recall that $\boldsymbol{F}$ is the deformation gradient tensor, J is the Jacobian, $\boldsymbol{K}$ is the permeability of the medium, β is the pressure-coupling array, and q is a volumetric source term. In the equation of mass conservation, Eq. (B.1.5), the time derivative is with respect to the skeleton, *i.e.*

$$\frac{d^s m_i}{dt} = \frac{\partial m_i}{\partial t} + \nabla_x m_i \cdot \boldsymbol{V}^s, \tag{B.1.8}$$

where m is the fluid mass increase, defined per unit volume of the reference configuration.

B.1.2 Deformation

Large strain deformation of the bulk medium is modelled via finite-deformation elasticity. The skeleton kinematics are governed by the linear momentum bal-

ance

$$\nabla_X \cdot (\boldsymbol{F}\boldsymbol{S}) = \boldsymbol{0}, \tag{B.1.9}$$

where $\boldsymbol{S}$ is the second Piola-Kirchoff stress tensor. Eq. (B.1.9) is solved subject to the constraint

$$J = 1 + \frac{\sum_{i=1}^{N} m_i}{\rho_f}, \tag{B.1.10}$$

which implies incompressibility of the solid matrix, and is enforced numerically using a Lagrange multiplier, denoted λ.

An isotropic exponential-form material law can be used to define the strain energy, Ψ^s, which is dependent on both skeletal displacement and fluid volume changes. Specifically,

$$\begin{aligned}\Psi^s = a\Big[exp\Big(D_1\left(\bar{I}_1\left(1+\sum_{i=1}^{N} Q_1^i \frac{m_i}{\rho_f}\right)-3\right)\\ +D_2\left(\bar{I}_2\left(1+\sum_{i=1}^{N} Q_2^i \frac{m_i}{\rho_f}\right)-3\right)\\ +D_3\left((J-1)^2+\sum_{i=1}^{N} Q_3^i\left(\frac{m_i}{\rho_f}\right)^2\right)\Big)-1\Big],\end{aligned} \tag{B.1.11}$$

where the material parameter set is $\{a, D_j, Q_j^i\}$ for $j = 1,2,3$, and $\bar{I}_1$ and $\bar{I}_2$ are the modified invariants of the right Cauchy–Green deformation tensor, $\boldsymbol{C}_G = \boldsymbol{F}^T\boldsymbol{F}$. Note that the scales Q_j^i can capture varying vessel compliances within the porous media.

The constitutive law is coupled to the aforementioned skeletal volume constraint to give the constrained constitutive law

$$\Psi^s_{cons} = \Psi^s + \lambda\left(J - 1 - \sum_{i=1}^{N}\frac{m_i}{\rho_f}\right), \tag{B.1.12}$$

from which $\boldsymbol{S}$ can be evaluated as (see Bonet and Wood [10], 2008, Section 6.5.1)

$$\boldsymbol{S} = \frac{\partial \Psi^s}{\partial \boldsymbol{E}} + \lambda J \boldsymbol{C}_G^{-1}, \tag{B.1.13}$$

where $\boldsymbol{E} = (\boldsymbol{C}_G - \boldsymbol{I})/2$ is the Lagrangian strain tensor. The relationship between the constitutive law and the compartmental pressure is given by [27]

$$p_i = \frac{\partial \Psi^s}{\partial (J\phi_{f,i})} - \lambda. \tag{B.1.14}$$

Bibliography

[1] 2020 Science. 2020 Science: Mathmatical and computational modelling of complex natural systems. `www.2020science.net`, 2011. [Online; accessed 19-Nov-2011].

[2] Aguirre G. K. and Detre J. A. The development and future of Perfusion fMRI for dynamic imaging of human brain activity. *NeuroImage*, 62(2): 1279–1285, Apr. 2012.

[3] Anderson T. and Jackson R. A fluid mechanical description of fluidized beds. *I&EC Fundamentals*, 6(4):527–539, 1967.

[4] Annan K. Mathematical modeling of the dynamic exchange of solutes during bicarbonate dialysis. *Mathematical and Computer Modelling*, 55(5-6):1691–1704, Mar. 2012.

[5] Araoz P., Glockner J., Mcgee K., Potter D. D., Valeti V. U., Stanley D., and Christian T. 3 Tesla MR imaging provides improved contrast in first-pass myocardial perfusion imaging over a range of gadolinium doses. *Journal of Cardiovascular Magnetic Resonance*, 7(3):559–564, May 2005.

[6] Arts M. *A mathematical model of the dynamics of the left ventricle and the coronary circulation*. PhD thesis, Rijksuniversiteit Limburg, 1978.

[7] Bassingthwaighte J. B., Yipintsoi T., and Harvey R. B. Microvasculature of the dog left ventricular myocardium. *Microvascular Research*, 7(2):229–249, Mar. 1974.

[8] Bear J. *Dynamics of fluids in porous media*. Dover Publications, 1988.

[9] Biot M. A. Theory of finite deformations of porous solids. *Indiana University Mathematics Journal*, 21(7):597–620, 1972.

[10] Bonet J. and Wood R. *Nonlinear Continuum Mechanics for Finite Element Analysis*. Cambridge University Press, 2008.

[11] Borges J. B., Suarez-Sipmann F., Bohm S. H., Tusman G., Melo A., Maripuu E., Sandström M., Park M., Costa E. L. V., Hedenstierna G., and Amato M. Regional lung perfusion estimated by electrical impedance tomography in a piglet model of lung collapse. *Journal of Applied Physiology*, 112(1):225–36, Jan. 2012.

[12] Botnar R. M. and Nagel E. Structural and functional imaging by MRI. *Basic Research in Cardiology*, 103(2):152–60, Mar. 2008.

[13] Bowen R. M. Incompressible porous media by useof the theory of mixtures. *International Journal of Engineering Science*, 18:1129–1148, 1980.

[14] Braakman R., Sipkema P., and Westerhof N. A dynamic nonlinear lumped parameter model for skeletal muscle circulation. *Annals of Biomedical Engineering*, 17(6):593–616, Jan. 1989.

[15] Carabello B. A. Understanding coronary blood flow: the wave of the future. *Circulation*, 113(14):1721–2, Apr. 2006.

[16] Chabiniok R., Moireau P., Lesault P.-F., Rahmouni A., Deux J.-F., and Chapelle D. Estimation of tissue contractility from cardiac cine-MRI using a biomechanical heart model. *Biomechanics and Modeling in Mechanobiology*, 11(5):609–30, May 2012.

[17] Chabiniok R., Wong J., Giese D., Nordsletten D. A., Shi W., Greil G., Rueckert D., Razavi R., Schaeffter T., and Smith N. P. Flow analysis in cardiac chambers combining phase contrast, 3d tagged and cine mri. In *Functional Imaging and Modeling of the Heart*, pages 360–369. Springer, 2013.

[18] Chan R., Karl W., and Lees R. A new model-based technique for enhanced small-vessel measurements in x-ray cine-angiograms. *IEEE Transactions on Medical Imaging*, 19(3):243–255, 2000.

[19] Chapelle D., Gerbeau J.-F., Sainte-Marie J., and Vignon-Clementel I. E. A poroelastic model valid in large strains with applications to perfusion in cardiac modeling. *Computational Mechanics*, 46(1):91–101, Dec. 2009.

[20] Chapman S., Shipley R. J., and Jawad R. Multiscale modeling of fluid transport in tumors. *Bulletin of Mathematical Biology*, 70(8):2334–57, Nov. 2008.

[21] Chilian W. M., Eastham C. L., and Marcus M. L. Microvascular distribution of coronary vascular resistance in beating left ventricle. *American Journal of Physiology-Heart and Circulatory Physiology*, 251:779–788, 1986.

[22] Chilian W. M., Layne S. M., Klausner E. C., Eastham C. L., Marcus M. L., Klausner C., and Edward C. Redistribution of coronary microvascular resistance produced by dipyridamole. *American Journal of Physiology-Heart and Circulatory Physiology*, 256:383–390, 1989.

[23] Ciarlet P. G. *The finite element method for elliptic problems*. Access Online via Elsevier, 1978.

[24] Cookson A. N., Lee J., Michler C., Chabiniok R., Hyde E. R., Nordsletten D. A., Sinclair M., Siebes M., and Smith N. P. A novel porous mechanical framework for modelling the interaction between coronary perfusion and myocardial mechanics. *Journal of Biomechanics*, 45(5):850–5, Mar. 2012.

[25] Cookson A. N., Lee J., Michler C., Chabiniok R., Hyde E. R., Nordsletten D. A., and Smith N. P. A Finite Element Model of MRI Contrast Agent Transport in the Myocardium. *Medical Image Analysis (Submitted)*, 2013.

[26] Coussy O. *Mechanics of porous continua.* John Wiley and Sons, New York, 1995.

[27] Coussy O. *Poromechanics*. John Wiley & Sons Inc, 2004.

[28] Crick S., Sheppard M., Ho S., Gebstein L., and Anderson R. Anatomy of the pig heart : comparisons with normal human cardiac structure. *Journal of Anatomy*, pages 105–119, 1998.

[29] de Kemp R. A., Epstein F. H., Catana C., Tsui B. M. W., and Ritman E. L. Small-animal molecular imaging methods. *Journal of Nuclear Medicine*, 51 Suppl 1(5):18S–32S, May 2010.

[30] Dellsperger K. C., Janzen D. L., Eastham C. L., and Marcus M. L. Effects of acute coronary artery occlusion on the coronary microcirculation. *American Journal of Physiology-Heart and Circulatory Physiology*, 259:909–916, 1990.

[31] Dijkstra E. A note on two problems in connexion with graphs. *Numerische mathematik*, 1959.

[32] Ding Z. and Friedman M. H. Dynamics of human coronary arterial motion and its potential role in coronary atherogenesis. *Journal of Biomechanical engineering*, 122(5):488–92, Oct. 2000.

[33] Dousset V., Ballarino L., Delalande C., Coussemacq M., Canioni P., Petry K., and Caille J. Comparison of ultrasmall particles of iron oxide (USPIO)-enhanced T2-weighted, conventional T2-weighted, and gadolinium-enhanced T1-weighted MR images in rats with experimental autoimmune encephalomyelitis. *American Journal of Neuroradiology*, 20 (2):223, 1999.

[34] Duncker D. and Bache R. Regulation of coronary blood flow during exercise. *Physiological Reviews*, pages 1009–1086, 2008.

[35] Efimov I. R., Nikolski V. P., and Salama G. Optical imaging of the heart. *Circulation Research*, 95(1):21–33, July 2004.

[36] Elman H. C., Silvester D. J., and Wathen A. J. *Finite Elements and Fast Iterative Solvers: with Applications in Incompressible Fluid Dynamics: with Applications in Incompressible Fluid Dynamics*. Oxford University Press, 2005.

[37] euHeart. euHeart: integrated cardiac care using patient-specific cardiovascular modelling. `www.euheart.eu/`, 2008. [Online; accessed 22-Dec-2010].

[38] Euler L. Principes généraux de l'état d'équilibre d'un fluide [General principles of the state of equilibrium of a fluid]. *Académie Royale des Sciences et des Belles-Lettres de Berlin, Mémoires*, 11:217–273, 1757.

[39] Euler L. Principia pro motu sanguinis per arterias determinando. *Opera posthuma mathematica et physica anno 1844 detecta*, 2:814–823, 1775.

[40] Fernandes P., Carreira P., and Bahir M. Mass balance simulation and principal components analysis applied to groundwater resources: Essaouira basin. *Environmental Earth Sciences*, 59(7):1475–1484, 2010.

[41] Figueroa C., Vignon-Clementel I., Jansen K., Hughes T., and Taylor C. A coupled momentum method for modeling blood flow in three-dimensional deformable arteries. *Computer Methods in Applied Mechanics and Engineering*, 195(41-43):5685–5706, 2006.

[42] Fokkema D. S., VanTeeffelen J. W. G. E., Dekker S., Vergroesen I., Reitsma J. B., and Spaan J. A. E. Diastolic time fraction as a determinant of subendocardial perfusion. *American Journal of Physiology-Heart and Circulatory Physiology*, 288(5):H2450–6, May 2005.

[43] Formaggia L., Lamponi D., and Quarteroni A. One-dimensional models for blood flow in arteries. *Journal of Engineering Mathematics*, 47(3):251–276, 2003.

[44] Forsythe G. and Wasow W. *Finite-Difference Methods for Partial Differential Equations*. Dover Publications, 2004.

[45] Frangi A. and Niessen W. Multiscale vessel enhancement filtering. *Medical Image Computing and Computer-Assisted Intervention*, 1496:130–137, 1998.

[46] Fulton W. F. The Dynamic Factor in Enlargement of Coronary Arterial Anastomoses, and Paradoxical Changes in the Subendocardial Plexus. *British Heart Journal*, 26:39–50, Jan. 1964.

[47] Gilbert S. H., Benson A. P., Li P., and Holden A. V. Regional localisation of left ventricular sheet structure: integration with current models of cardiac fibre, sheet and band structure. *European Journal of Cardio-thoracic Surgery*, 32(2):231–49, Aug. 2007.

[48] Glagov S., Vito R., Giddens D. P., and Zarins C. K. Micro-architecture and composition of artery walls: relationship to location, diameter and the distribution of mechanical stress. *Journal of Hypertension*, 10(6):101–104, 1992.

[49] Goyal A., Lee J., Lamata P., Grau V., van den Wijngaard J. P. H. M., van Horssen P., Spaan J. A. E., Siebes M., and Smith N. P. Model-based Vasculature Extraction from Optical Fluorescence Cryomicrotome Images. *IEEE Transactions on Medical Imaging*, 32(1):56–72, 2013.

[50] Harvey W. Exercitatio anatomica de motu cordis et sanguinis in animalibus. *Frankfurt am Main*, 1628, 1928.

[51] Hoffman J. Transmural myocardial perfusion. *Progress in Cardiovascular Diseases*, pages 429–464, 1987.

[52] Holzapfel G. *Nonlinear solid mechanics: a continuum approach for engineering*. John Wiley & Sons Ltd., 2000.

[53] Hornung U. *Homogenization and Porous Media*, volume 6. Springer Verlag, 1997.

[54] Horssen P. V., van den Wijngaard J. P. H. M., Nolte F., Hoefer I., Haverslag R., Spaan J. A. E., and Siebes M. Extraction of Coronary Vascular Tree and Myocardial Perfusion Data from Stacks of Cryomicrotome Images. *Functional Imaging and Modeling of the Heart*, pages 486–494, 2009.

[55] Huyghe J. M. and Van Campen D. H. Finite deformation theory of hierarchically arranged porous solids. I: Balance of mass and momentum. *International Journal of Engineering Science*, 33(13):1861–1871, 1995.

[56] Huyghe J. M. and van Campen D. H. Finite deformation theory of hierarchically arranged porous solids. II: Constitutive behaviour. *International Journal of Engineering Science*, 33(13):1873–1886, 1995.

[57] Huyghe J. M., Van Campen D. H., Arts T., and Heethaar R. M. A two-phase finite element model of the diastolic left ventricle. *Journal of Biomechanics*, 24(7), 1991.

[58] Huyghe J. M., Arts T., van Campen D. H., and Reneman R. S. Porous medium finite element model of the beating left ventricle. *American Journal of Physiology-Heart and Circulatory Physiology*, 262(4):H1256–1267, Apr. 1992.

[59] Hyde E. R., Michler C., Lee J., Cookson A. N., Chabiniok R., Nordsletten D. A., and Smith N. P. Parameterisation of multi-scale continuum perfusion models from discrete vascular networks. *Medical & Biological Engineering & Computing*, 51(5):557–570, 2013.

[60] Ibrahim T., Hackl T., Nekolla S., Breuer M., Feldmair M., Schömig A., and Schwaiger M. Acute myocardial infarction: Serial cardiac mr imaging shows a decrease in delayed enhancement of the myocardium during the 1st week after reperfusion1. *Radiology*, 254(1):88, 2010.

[61] Johnson R. and Wichern D. *Applied multivariate statistical analysis*, volume 4. Prentice hall Upper Saddle River, NJ, 2002.

[62] Kaimovitz B., Lanir Y., and Kassab G. S. A full 3-D reconstruction of the entire porcine coronary vasculature. *American journal of physiology. Heart and circulatory physiology*, 299(4):H1064–76, Oct. 2010.

[63] Kalukin A., Van Geet M., and Swennen R. Principal components analysis of multienergy x-ray computed tomography of mineral samples. *IEEE Transactions on Nuclear Science*, 47(5):1729–1736, 2000.

[64] Kanatsuka H., Lamping K. G., Eastham C. L., Dellsperger K. C., and Marcus M. L. Comparison of the effects of increased myocardial oxygen consumption and adenosine on the coronary microvascular resistance. *Circulation Research*, 65(5):1296–1305, Nov. 1989.

[65] Kanatsuka H., Lamping K. G., Eastham C. L., and Marcus M. L. Heterogeneous changes in epimyocardial microvascular size during graded coronary stenosis. Evidence of the microvascular site for autoregulation. *Circulation Research*, 66(2):389–396, Feb. 1990.

[66] Kaneko N., Matsuda R., Toda M., and Shimamoto K. Three-dimensional reconstruction of the human capillary network and the intramyocardial

micronecrosis. *American Journal of Physiology-Heart and Circulatory Physiology*, 300(3):H754–61, Mar. 2011.

[67] Kassab G. S. Functional hierarchy of coronary circulation: direct evidence of a structure-function relation. *American journal of physiology. Heart and circulatory physiology*, 289(6):H2559–65, Dec. 2005.

[68] Kassab G. S. and Fung Y. C. Topology and dimensions of pig coronary capillary network. *American Journal of Physiology-Heart and Circulatory Physiology*, 267(6):H319–25, July 1994.

[69] Kassab G. S., Rider C. A., Tang N. J., and Fung Y. C. Morphometry of pig coronary arterial trees. *American Journal of Physiology-Heart and Circulatory Physiology*, 265(1):H350–365, July 1993.

[70] Kassab G. S., Lin D. H., and Fung Y. C. Morphometry of pig coronary venous system. *American Journal of Physiology-Heart and Circulatory Physiology*, 267(6):H2100–13, Dec. 1994.

[71] Kassab G. S., Algranati D., and Lanir Y. Myocardial-vessel interaction: role of LV pressure and myocardial contractility. *Medical & Biological Engineering & Computing*, 51(7):729–739, Apr. 2013.

[72] Katz A. *Physiology of the Heart*. Lippincott Williams & Wilkins, 2005.

[73] Kazakidi A., Sherwin S., and Weinberg P. D. Effect of Reynolds number and flow division on patterns of haemodynamic wall shear stress near branch points in the descending thoracic aorta. *Journal of the Royal Society Interface*, 6(35):539–48, June 2009.

[74] Kelle S., Hays A. G., Hirsch G. A., Gerstenblith G., Miller J. M., Steinberg A. M., Schär M., Texter J. H., Wellnhofer E., Weiss R. G., and Stuber M. Coronary artery distensibility assessed by 3.0 Tesla coronary magnetic resonance imaging in subjects with and without coronary artery disease. *American Journal of Cardiology*, 108(4):491–7, Aug. 2011.

[75] Kolyva C., Spaan J. A. E., Piek J. J., and Siebes M. Windkesselness of coronary arteries hampers assessment of human coronary wave speed by single-point technique. *American journal of physiology. Heart and circulatory physiology*, 295(2):H482–90, Aug. 2008.

[76] Ku D. N. Blood Flow in Arteries. *Annual Review of Fluid Mechanics*, 29(1): 399–434, Jan. 1997.

[77] Lamata P., Niederer S., Nordsletten D., Barber D., Roy I., Hose D. R., and Smith N. P. An accurate, fast and robust method to generate patient-specific cubic Hermite meshes. *Medical Image Analysis*, 15(6):801–13, Dec. 2011.

[78] Lamberts R., van Rijen M., Sipkema P., Fransen P., Sys S., and Westerhof N. Coronary perfusion and muscle lengthening increase cardiac contraction: different stretch-triggered mechanisms. *American Journal of Physiology-Heart and Circulatory Physiology*, 283(4):H1515, 2002.

[79] Lee J. *Computational Modelling of Coronary Structure and Flow Mechanics*. PhD thesis, University of Oxford, 2009.

[80] Lee J. and Smith N. P. Development and application of a one-dimensional blood flow model for microvascular networks. *Proceedings of the Institution of Mechanical Engineers, Part H: Journal of Engineering in Medicine*, 222 (4):487–512, May 2008.

[81] Lee J. and Smith N. P. The Multi-Scale Modelling of Coronary Blood Flow. *Annals of Biomedical Engineering*, 40(11):2399–2413, May 2012.

[82] Lee J., Beighley P. E., Ritman E. L., and Smith N. P. Automatic segmentation of 3D micro-CT coronary vascular images. *Medical Image Analysis*, 11 (6):630–47, Dec. 2007.

[83] Lee J., Niederer S., Nordsletten D. A., Legrice I. J., Smaill B. H., Kay D., and Smith N. P. Coupling contraction, excitation, ventricular and coronary blood flow across scale and physics in the heart. *Philosophical transactions. Series A, Mathematical, physical, and engineering sciences*, 367(1896): 2311–31, June 2009.

[84] Legrice I. J., Smaill B. H., Chai L. Z., Edgar S. G., Gavin J. B., and Hunter P. J. Laminar structure of the heart : ventricular myocyte arrangement and connective tissue architecture in the dog. *American journal of physiology. Heart and circulatory physiology*, 269(H):571—-582, Aug. 1995.

[85] Lipowsky H. H., Kovalcheck S., and Zweifach B. W. The distribution of blood rheological parameters in the microvasculature of cat mesentery. *Circulation Research*, 43(5):738–49, Nov. 1978.

[86] Lydzba D., Pietruszczak S., and Shao J. On anisotropy of stratified rocks: homogenization and fabric tensor approach. *Computers and Geotechnics*, 30(4):289–302, 2003.

[87] Malvern L. *Introduction to the Mechanics of a Continuous Medium*. Prentice-Hall., 1969.

[88] Maret E., Todt T., Brudin L., Nylander E., Swahn E., Ohlsson J. L., and Engvall J. E. Functional measurements based on feature tracking of cine magnetic resonance images identify left ventricular segments with myocardial scar. *Cardiovascular Ultrasound*, 7:53, Jan. 2009.

[89] Marxen M., Sled J. G., Yu L. X., Paget C., and Henkelman R. M. Comparing microsphere deposition and flow modeling in 3D vascular trees. *AJP: Heart and Circulatory Physiology*, 291(5):H2136–H2141, July 2006.

[90] Masud A. and Hughes T. J. R. A stabilized mixed finite element method for Darcy flow. *Computer Methods in Applied Mechanics and Engineering*, 191(39-40):4341–4370, Aug. 2002.

[91] Maxwell M. P., Hearse D. J., and Yellon D. M. Species variation in the coronary collateral circulation during regional myocardial ischaemia: a critical determinant of the rate of evolution and extent of myocardial infarction. *Cardiovascular Research*, 21(10):737–46, Oct. 1987.

[92] May-Newman K. and McCulloch A. D. Homogenization modeling for the mechanics of perfused myocardium. *Progress in Biophysics and Molecular Biology*, 69(2-3):463–81, Jan. 1998.

[93] May-Newman K., Omens J. H., Pavelec R. S., and McCulloch A. D. Three-dimensional transmural mechanical interaction between the coronary vasculature and passive myocardium in the dog. *Circulation Research*, 74 (6):1166–78, June 1994.

[94] May-Newman K., Mathieu-Costello O., Omens J. H., Klumb K., and McCulloch A. D. Transmural Distribution of Capillary Morphology as a Function of Coronary Perfusion Pressure in the Resting Canine Heart. *Microvascular Research*, 50(3):381–396, 1995.

[95] McCabe J. M., Armstrong E. J., Hoffmayer K. S., Bhave P. D., Macgregor J. S., Hsue P., Stein J. C., Kinlay S., and Ganz P. Impact of Door-to-Activation Time on Door-to-Balloon Time in Primary Percutaneous Coronary Intervention for ST-Segment Elevation Myocardial Infarctions: A Report From the Activate-SF Registry. *Circulation. Cardiovascular quality and outcomes*, 5(5):672–9, Sept. 2012.

[96] McCulloch A. D., Hunter P. J., and Smaill B. H. Mechanical effects of coronary perfusion in the passive canine left ventricle. *American Journal of Physiology-Heart and Circulatory Physiology*, 262:523–530, 1992.

[97] Michler C., Cookson A. N., Chabiniok R., Hyde E. R., Lee J., Sinclair M., Sochi T., Goyal A., Vigueras G., Nordsletten D. A., and Smith N. P. A

computationally efficient framework for the simulation of cardiac perfusion using a multi-compartment Darcy porous-media flow model. *International Journal for Numerical Methods in Biomedical Engineering*, 29(2): 217–232, 2013.

[98] Muehling O., Jerosch-Herold M., Panse P., Zenovich A., Wilson B., Wilson R., and Wilke N. Regional Heterogeneity of Myocardial Perfusion in Healthy Human Myocardium: Assessment with Magnetic Resonance Perfusion Imaging. *Journal of Cardiovascular Magnetic Resonance*, 6(2):499–507, Apr. 2004.

[99] Murray C. The physiological principle of minimum work: I. The vascular system and the cost of blood volume. *PNAS*, 12(3):207–214, 1926.

[100] Nesto R. W. and Kowalchuk G. J. The ischemic cascade: temporal sequence of hemodynamic, electrocardiographic and symptomatic expressions of ischemia. *American Journal of Cardiology*, 59(7):23C–30C, Mar. 1987.

[101] Ng E. Y. K., Ghista D. N., and Jegathese R. C. Perfusion studies of steady flow in poroelastic myocardium tissue. *Computer Methods in Biomechanics and Biomedical Engineering*, 8(6):349–57, Dec. 2005.

[102] Nichols M., Townsend N., Luengo-Fernandez R., Leal J., Gray A., Scarborough P., and M R. European Cardiovascular Disease Statistics 2012. Technical report, European Society of Cardiology, European Heart Network, Brussels, 2012.

[103] Niederer S., Plank G., Chinchapatnam P., Ginks M., Lamata P., Rhode K. S., Rinaldi C. A., Razavi R., and Smith N. P. Length-dependent tension in the failing heart and the efficacy of cardiac resynchronization therapy. *Cardiovascular Research*, 89(2):336–43, Feb. 2011.

[104] Nielsen P. M., Legrice I. J., Smaill B. H., and Hunter P. J. Mathematical model of geometry and fibrous structure of the heart. *American Journal of Physiology*, 260(4 Pt 2):H1365–78, Apr. 1991.

[105] Ofjord E., Clausen G., and Aukland K. Skimming of microspheres in vitro : implications for measurement of intrarenal blood flow. *American Physiological Society*, 1981.

[106] Otsu N. A threshold selection method from gray-level histograms. *Automatica*, 20(1):62–66, 1975.

[107] Parker J. C., Cave C. B., Ardell J. L., Hamm C. R., Williams S. G., Susan G., and James C. Vascular tree structure affects lung blood flow heterogeneity

simulated in three dimensions. *Journal of Applied Physiology*, 83(4):1370–1382, Oct. 1997.

[108] Perktold K. and Rappitsch G. Computer simulation of local blood flow and vessel mechanics in a compliant carotid artery bifurcation model. *Journal of Biomechanics*, 28(7):845–856, 1995.

[109] Pindera M. Z., Ding H., Athavale M. M., and Chen Z. Accuracy of 1D microvascular flow models in the limit of low Reynolds numbers. *Microvascular Research*, 77(3):273–80, May 2009.

[110] Plein S., Ryf S., Schwitter J., Radjenovic A., Boesiger P., and Kozerke S. Dynamic contrast-enhanced myocardial perfusion MRI accelerated with kt sense. *Magnetic Resonance in Medicine*, 58(4):777–785, 2007.

[111] preDiCT. preDiCT: computational prediction of drug cardiac toxicity. `http://www.vph-noe.eu/vph-projects/74-eu-fp7-vph-projects/47-predict-strep`, 2008. [Online; accessed 03-Sept-2012].

[112] Pries A. R., Secomb T. W., and Gross J. Blood Flow in Microvascular Networks. *Cardiovascular Medicine*, 1990.

[113] Pries A. R., Secomb T. W., Gessner T., Sperandio M. B., Gross J. F., and Gaehtgens P. Resistance to blood flow in microvessels in vivo. *Circulation Research*, 75(5):904–915, Nov. 1994.

[114] Pries A. R., Secomb T. W., and Gaehtgens P. Biophysical aspects of blood flow in the microvasculature. *Cardiovascular Research*, 32(4):654–67, Oct. 1996.

[115] Prinzen F. W. and Bassingthwaighte J. B. Blood flow distributions by microsphere deposition methods. *Cardiovascular Research*, 45:13–21, 2000.

[116] Pudney C. Distance-Ordered Homotopic Thinning: A Skeletonization Algorithm for 3D Digital Images. *Computer Vision and Image Understanding*, 72(3):404–413, Dec. 1998.

[117] Rakusan K., Flanagan M. F., Geva T., Southern J., and Van Praagh R. Morphometry of human coronary capillaries during normal growth and the effect of age in left ventricular pressure-overload hypertrophy. *Circulation*, 86(1):38–46, July 1992.

[118] Rankin J. S., McHale P. A., Arentzen C. E., Ling D., Greenfield J. C., and Anderson R. W. The three-dimensional dynamic geometry of the left ventricle in the conscious dog. *Circulation Research*, 39(3):304–313, Sept. 1976.

[119] Rodriguez E., Hoger A., and McCulloch A. Stress-dependent finite growth in soft elastic tissues. *Journal of Biomechanics*, pages 455–467, 1994.

[120] Rossi G. E. *Numerical simulation of perfusion in the beating heart*. PhD thesis, Politechnico Di Milano, 2007.

[121] Sauvola J. and Pietikäinen M. Adaptive document image binarization. *Pattern Recognition*, 33:225–236, 2000.

[122] Schreiner W., Karch R., Neumann F., and Neumann M. *Constrained constructive optimization of arterial tree models*. New York. Oxford University Press, 2000.

[123] Sellke F. W., Myers P. R., Bates J. N., and Harrison G. Influence of vessel size on the sensitivity of porcine coronary microvessels to nitroglycerin. *American Journal of Physiology-Heart and Circulatory Physiology*, 258 (H):515–520, 1990.

[124] Sherwin S., Formaggia L., Peiró J., and Franke V. Computational modelling of 1D blood flow with variable mechanical properties and its application to the simulation of wave propagation in the human arterial system. *International Journal for Numerical Methods in Fluids*, 43(6-7):673–700, 2003.

[125] Shipley R. J. and Chapman S. Multiscale modelling of fluid and drug transport in vascular tumours. *Bulletin of Mathematical Biology*, 72(6): 1464–91, Aug. 2010.

[126] Slattery J. Flow of Viscoelastic Fluids Through Porous Media. *AIChE Journal*, 13(6):1066–1071, 1967.

[127] Smith N. P. and Kassab G. S. Analysis of coronary blood flow interaction with myocardial mechanics based on anatomical models. *Philosophical transactions. Series A, Mathematical, physical, and engineering sciences*, 359 (1783), 2001.

[128] Smith N. P., Pullan A., and Hunter P. J. Generation of an anatomically based geometric coronary model. *Annals of Biomedical Engineering*, 28(1): 14–25, Jan. 2000.

[129] Smith N. P., Pullan A., and Hunter P. J. An Anatomically Based Model of Transient Coronary Blood Flow in the Heart. *SIAM Journal of Applied Mathematics*, 62(3):990– 1018, Jan. 2001.

[130] Smith N. P., Mulquiney P., Nash M. P., Bradley C., Nickerson D., and Hunter P. J. Mathematical modelling of the heart: cell to organ. *Chaos, Solitons & Fractals*, 13(8):1613–1621, June 2002.

[131] Spaan J. A. E., Breuls N. P., and Laird J. D. Diastolic-systolic coronary flow differences are caused by intramyocardial pump action in the anesthetized dog. *Circulation Research*, 49(3):584—-593, May 1982.

[132] Spaan J. A. E., Siebes M., Wee R., Kolyva C., Vink H., Fokkema D. S., Streekstra G., and Vanbavel E. Visualisation of intramural coronary vasculature by an imaging cryomicrotome suggests compartmentalisation of myocardial perfusion areas. *Medical & Biological Engineering & Computing*, 43:431–435, 2005.

[133] Spaan J. A. E., Kolyva C., van den Wijngaard J. P. H. M., ter Wee R., van Horssen P., Piek J. J., and Siebes M. Coronary structure and perfusion in health and disease. *Philosophical transactions. Series A, Mathematical, physical, and engineering sciences*, 366(1878):3137–53, Sept. 2008.

[134] Stergiopulos N., Young D. F., and Rogge T. R. Computer simulation of arterial flow with applications to arterial and aortic stenoses. *Journal of Biomechanics*, 25(12):1477–88, Dec. 1992.

[135] Strahler A. N. Hypsometric (area-altitude) analysis of erosional topology. *Geological Society of America Bulletin*, 11:1117–1142, 1952.

[136] Süli E. *Finite element methods for partial differential equations*. Oxford University Computing Laboratory, 2002.

[137] Taylor C. A. and Figueroa C. A. Patient-specific modeling of cardiovascular mechanics. *Annual Review of Biomedical Engineering*, 11:109–34, Jan. 2009.

[138] TGCA. The Cancer Genome Atlas: Understanding genomics to improve cancer care. `http://cancergenome.nih.gov/`, 2006. [Online; accessed 02-Jan-2013].

[139] Toyota E., Fujimoto K., Ogasawara Y., Kajita T., Shigeto F., Matsumoto T., Goto M., and Kajiya F. Dynamic Changes in Three-Dimensional Architecture and Vascular Volume of Transmural Coronary Microvasculature Between Diastolic- and Systolic-Arrested Rat Hearts. *Circulation*, 105(5): 621–626, Feb. 2002.

[140] Trefethen L. *Spectral methods in MATLAB*, volume 10. SIAM, 2000.

[141] Trefethen L. and Bau III D. *Numerical linear algebra*. SIAM, 1997.

[142] Tully B. and Ventikos Y. Coupling poroelasticity and CFD for cerebrospinal fluid hydrodynamics. *IEEE Transactions on Bio-medical Engineering*, 56(6):1644–51, June 2009.

[143] van den Wijngaard J. P. H. M., Schulten H., van Horssen P., ter Wee R., Siebes M., Post M. J., and Spaan J. A. E. Porcine coronary collateral formation in the absence of a pressure gradient remote of the ischemic border zone. *American Journal of Physiology-Heart and Circulatory Physiology*, 300 (5):H1930–7, May 2011.

[144] van den Wijngaard J. P. H. M., Schwarz J. C. V., van Horssen P., van Lier M. G. J. T. B., Dobbe J. G. G., Spaan J. A. E., and Siebes M. 3D Imaging of vascular networks for biophysical modeling of perfusion distribution within the heart. *Journal of Biomechanics*, 46(2):229–39, Jan. 2013.

[145] van Horssen P., Siebes M., Hoefer I., Spaan J. A. E., and van den Wijngaard J. P. H. M. Improved detection of fluorescently labeled microspheres and vessel architecture with an imaging cryomicrotome. *Medical & Biological Engineering & Computing*, 48(8):735–44, Aug. 2010.

[146] VanBavel E. and Spaan J. A. E. Branching patterns in the porcine coronary arterial tree. Estimation of flow heterogeneity. *Circulation Research*, 71(5): 1200–1212, Nov. 1992.

[147] Vankan W. J., Huyghe J. M., and Janssen J. D. Poroelasticity of saturated solids with an application to blood perfusion. *International Journal of Engineering Science*, 34(9):1019–1031, 1996.

[148] Vankan W. J., Huyghe J. M., Janssen J. D., Huson A., and Schreiner W. Finite element blood flow through biological tissue. *International Journal of Engineering Science*, 35(4):375–385, 1997.

[149] Vankan W. J., Huyghe J. M., Slaaf D. W., van Donkelaar C. C., Drost M. R., Janssen J. D., and Huson A. Finite-element simulation of blood perfusion in muscle tissue during compression and sustained contraction. *American Journal of Physiology-Heart and Circulatory Physiology*, 273(3):H1587–1594, Sept. 1997.

[150] Versteeg H. and Malalasekra W. *An Introduction to Computational Fluid Dynamics: The Finite Volume Method Approach*. Prentice Hall, 1996.

[151] Wang C. Y., Bassingthwaighte J. B., and Weissman L. J. Bifurcating distributive system using Monte Carlo method. *Mathematical and Computer Modelling*, 16(3):91–98, 1992.

[152] Weninger W. J., Meng S., Streicher J., and Müller G. B. A new episcopic method for rapid 3-D reconstruction: applications in anatomy and embryology. *Anatomy and Embryology*, 197(5):341–8, May 1998.

[153] Wentland A. L., Artz N. S., Fain S. B., Grist T. M., Djamali A., and Sadowski E. A. MR measures of renal perfusion, oxygen bioavailability and total renal blood flow in a porcine model: noninvasive regional assessment of renal function. *Nephrology Dialysis Transplantation*, 27(1):128–35, Jan. 2012.

[154] Wentzel J. J., Chatzizisis Y. S., Gijsen F. J. H., Giannoglou G. D., Feldman C. L., and Stone P. H. Endothelial shear stress in the evolution of coronary atherosclerotic plaque and vascular remodelling: current understanding and remaining questions. *Cardiovascular Research*, 96(2):234–43, Nov. 2012.

[155] Westerhof N., Boer C., Lamberts R. R., and Sipkema P. Cross-Talk Between Cardiac Muscle and Coronary Vasculature. *Physiological Reviews*, 86(4):1263–1308, 2006.

[156] Whitaker S. Diffusion and Dispersion in Porous Media. *AIChE Journal*, 13(3):420–427, 1967.

[157] Wüsten B., Buss D. D., Deist H., and Schaper W. Dilatory capacity of the coronary circulation and its correlation to the arterial vasculature in the canine left ventricle. *Basic Research in Cardiology*, 72(6):636–50, 1977.

[158] Xie X., Wang Y., and Zhou H. Impact of coronary tortuosity on the coronary blood flow: A 3D computational study. *Journal of Biomechanics*, 46 (11):1833–41, July 2013.

[159] Xie X., Wang Y., Zhu H., Zhou H., and Zhou J. Impact of coronary tortuosity on coronary blood supply: a patient-specific study. *PLOS One*, 8(5): e64564, Jan. 2013.

[160] Yada T., Hiramatsu O., Kimura A., Goto M., Ogasawara Y., Tsujioka K., Yamamori S., Ohno K., Hosaka H., and Kajiya F. In vivo observation of subendocardial microvessels of the beating porcine heart using a needle-probe videomicroscope with a CCD camera. *Circulation Research*, 72(5): 939–946, May 1993.

[161] Yada T., Hiramatsu O., Kimura A., Tachibana H., Chiba Y., Lu S., Goto M., Ogasawara Y., Tsujioka K., and Kajiya F. Direct In Vivo Observation of Subendocardial Arteriolar Response During Reactive Hyperemia. *Circulation Research*, 77(3):622–631, Sept. 1995.

[162] Young A. A. and Prince J. Cardiovascular Magnetic Resonance: Deeper Insights Through Bioengineering. *Annual Review of Biomedical Engineering*, 15(1):130510152341006, Sept. 2012.

[163] Young T. Hydraulic investigations, subservient to an intended Croonian lecture on the motion of the blood. *Phil. Trans. Roy. Soc., London*, 98:164–186, 1808.

[164] Zienkiewicz O. and R.L. T. *The finite element method*, volume 3. McGraw-hill London, 1977.

Glossary

angina pectoris	Angina pectoris, commonly known as angina, is chest pain due to ischemia of the heart muscle, generally due to obstruction or spasm of the coronary arteries.
angiogenesis	The physiological process through which new blood vessels form from pre-existing vessels.
atherosclerosis	Atherosclerosis is the thickening of the artery wall as a result of the accumulation of calcium and fatty materials such as cholesterol and triglyceride.
collateralisation	The growth of a blood vessel or several blood vessels that serve the same end organ or vascular bed as another blood vessel that cannot adequately supply that end organ or vascular bed sufficiently.
myocyte	A type of cell found in muscle tissue. Cardiac myocytes are responsible for generating the electrical impulses that control the heart rate and contraction.
pericardium	A double-walled sac containing the heart and the roots of the great vessels.
residual stress	The stress remaining in a body in the absence of any external tractions or pressures.
stenosis	An abnormal narrowing in a blood vessel or other tubular organ or structure.
thrombosis	Thrombosis is the formation of a blood clot inside a blood vessel, obstructing the flow of blood through the circulatory system. .